'TOXICOLOGY: BIOLOGICAL INTERACTIONS OF 2D Zn-Al LAYERED DOUBLE HYDROXIDES (LDHs) IN *IN-VITRO* AND *IN-VIVO* SYSTEMS'

A THESIS SUBMITTED BY

ASHTAMI JAYAKUMAR

TO

SREE CHITRA TIRUNAL INSTITUTE FOR MEDICAL SCIENCES AND TECHNOLOGY, TRIVANDRUM

IN PARTIAL FULFILLMENT OF THE REQUIREMENTS

FOR THE AWARD OF

DOCTOR OF PHILOSOPHY

2023

DECLARATION BY THE STUDENT

I, **Ashtami Jayakumar**, hereby certify that I had personally carried out the work depicted in the thesis entitled **'Toxicology: Biological interactions of 2D Zn-Al layered double hydroxides (LDHs) in *in-vitro* and *in-vivo* systems'**. No part of the thesis has been submitted for the award of any other degree or diploma prior to this date.

Place: Trivandrum

Date: 05.12.23

Signature

Name: Ashtami Jayakumar

Reg No: 2018/PhD/02

श्री चित्रा तिरुनाल आयुर्विज्ञान एवं प्रौद्योगिकी संस्थान, त्रिवेंद्रम, जैवचिकित्सकीय प्रौद्योगिकी स्कंध
पूजप्पुरा, तिरुवनन्तपुरम - 695 012, केरल, भारत
SREE CHITRA TIRUNAL INSTITUTE FOR MEDICAL SCIENCES AND TECHNOLOGY, TRIVANDRUM
BIO MEDICAL TECHNOLOGY WING
POOJAPPURA, THIRUVANANTHAPURAM - 695 012, KERALA, INDIA
(एक राष्ट्रीय महत्व का संस्थान, विज्ञान एवं प्रौद्योगिकी विभाग, भारत सरकार)
An Institution of National Importance, Department of Science & Technology, Government of India)
टेलीफॉन नं./Telephone No: 0471-2340801/2520450, फैक्स/Fax: 0471-2341814
ई-मेल/E-mail:sct@sctimst.ac.in वेबसाइट/Website : www.sctimst.ac.in

Dr. P V Mohanan

Toxicology Division

CERTIFICATE OF GUIDE

This is to certify that ***Ms. Ashtami Jayakumar,*** Toxicology Division of this institute has fulfilled the requirements prescribed for the Ph.D. degree of the Sree Chitra Tirunal Institute for Medical Sciences and Technology, Trivandrum. The thesis entitled '**Toxicology: Biological interactions of 2D Zn-Al layered double hydroxides (LDHs) in *in-vitro* and *in-vivo* systems'** was carried out under my direct supervision. No part of the thesis was submitted for the award of any degree or diploma prior to this date.

*Clearance was obtained from the Institute Animal Ethics Committee (IAEC) for carrying out the study. IAEC approval No: SCT/IAEC-379/NOVEMBER/2020/107.

Date: 05.12.2023

Signature

Dr P V Mohanan

Dr. P.V. Mohanan
Scientist-G & Head, Division of Toxicology,
Head, Dept. of Applied Biology
Sree Chitra Tirunal Institute for Medical Sciences and Technology (Govt. of India),
Trivandrum-12, Kerala,India.

The thesis entitled

'TOXICOLOGY: BIOLOGICAL INTERACTIONS OF 2D Zn-Al LAYERED DOUBLE HYDROXIDES (LDHs) IN *IN-VITRO* AND *IN-VIVO* SYSTEMS'

Submitted by

Ashtami Jayakumar

for the degree of

Doctor of philosophy

of

THE SREE CHITRA TIRUNAL INSTITUTE

FOR

MEDICAL SCIENCES AND TECHNOLOGY, TRIVANDRUM

Thiruvananthapuram

Is evaluated and approved by

Name of the guide

05/12/2023

Dr. P.V. Mohanan
Scientist-G & Head, Division of Toxicology.
Head, Dept. of Applied Biology
Sree Chitra Tirunal Institute for Medical Sciences and Technology (Govt. of India),
Trivandrum-12, Kerala, India.

Name of thesis examiner

डॉ. श्याम सुन्दर शर्मा / Dr. Shyam S. Sharma
प्रोफेसर / Professor
भेषज एवं विष विज्ञान विभाग
Department of Pharmacology & Toxicology
राष्ट्रीय औषधीय शिक्षा एवं अनुसंधान संस्थान
National Institute of Pharmaceutical Education and Research
सैक्टर - 67, एस.ए.एस. नगर - 160062, पंजाब
Sector-67, S.A.S. Nagar-160062, Punjab

ACKNOWLEDGEMENT

I would like my express my gratitude to the people who supported me all through my PhD journey and made this thesis a reality.

I sincerely acknowledge to our Director Dr. Sanjay Behari and Dr. H.K. Varma, Head, Biomedical Technology Wing, Trivandrum, Sree Chitra Tirunal Institute for Medical Sciences and Technology for the essential support and facilities provided for completing my Ph.D. work. I also acknowledge former Director Dr Asha Kishore for the support.

I thank our Dean, Associate Dean, Registrar, Deputy Registrar, other staff of Academic division and members of stores & purchase division for their academic assistance.

I acknowledge my sincere thanks to the Sree Chitra Tirunal Institute for Medical Sciences and Technology, Trivandrum for the Intitute fellowship to complete my PhD work.

I would like to thank my Doctoral Advising Committee members, Dr. Manoj Komath, Dr. Anugya Bhatt and Dr Sabareeswaran A for their timely suggestions and efforts in reviewing and assessing my research work.

I thank Dr Rajeev Kumar Sukumaran, Principal Scientist and head of Microbial process and technology Division and research scholar Meena for extending their research facilities for FT-IR analysis. I also thank Dr Prathish K P and other members of Dioxin research group, NIIST, TVM for providing ICP-MS facility.

I would like to acknowledge all the SICs of the institute, especially Dr. Manoj Komath, Dr. Sabareeswaran A, Dr. Uma Shankar P, Dr Rekha M.R, for providing their support and extending their lab facilities. I thank Mr. Willi Paul, Dr. Suresh Babu SMrs. Susan Mani, Mr. Prem Mohan M, Ms Jesna, Ms Devika and Ms Ammu, members of central analytical facilities, members of Division of bioceramics, members of Division of Biosurface Technology, members of DIMT, members of Histopathology laboratory and SCTIMST for the technical help.

I express my earnest thanks to all the staff and students of Toxicology Division for the memories and experiences during the journey. I am grateful for the helps offered by Dr. Remya N.S, Mrs Vandana Unnikrishnan, Dr. Sangeetha Vijayan, Ms Varsha, Mr. Shaji S., Mr. Harikumar, Mr. Sudeesan and Mrs. Dhanya. I also thank my seniors and former lab members Dr. Syama S, Dr. Biby T Edwin, Dr.Reshma VG, Dr Prajitha, Dr Anju and Akhil Venugopal for their support. I am also grateful to my collegues Dr

Megha KB, Ms Athira SS, Mr Joseph Xavier and Ms Arathy Ashok for the friendly work atmosphere and encouragement. I also thank my fellow PhD students of the institute for their friendships and helps at times.

I am grateful for my close group of people who been there for me and kept me moving. I am forever indebted to my parents Mr R Jayakumar and Mrs Beenu for the selfless sacrifices they made for me and my education. Their love, care and prayers have been my light and their presence helped me ease this journey beyond explanation. I thank them for believing in me at times of self-doubt. I thank my sister Anamika for her love and encouragement.

I am grateful for my close relatives, cousins and friends who were understanding and genuinely there for me.

I am extremely grateful to the Fulbright commission, India, United States-India educational foundation (USIEF) and the Institute of International Education **(**IIE) for the prestigious Fulbright Nehru Doctoral fellowship.

I sincerely thank my PhD guide Dr Mohanan PV for the opportunity, support and guidance throughout the journey.

I thank God for helping me out with the uncontrollable factors and am grateful for the opportunities and blessings I received.

Lastly, gratitude to everyone, everything and every moment, big or small that have led me knowingly or unknowingly and made this possible.

Ashtami Jayakumar

CONTENTS

LIST OF FIGURES

LIST OF TABLES

ABBREVIATIONS

0D	Zero-dimensional
1D	One-dimensional
2D	Two-dimensional
3D	Three-dimensional
μg	microgram
μl	Microliter
μM	Micromolar
AB/AM	Antibiotic/ Antimycotic
AFM	Atomic Force Microscopy
Al	Aluminium
ALD	Atomic layer deposition technique
ALP	Alkaline phosphatase
ALT	Alanine transaminase
AST	aspartate aminotransferase
AO	Acridine orange
AST	Aspartate transaminase
BBB	Blood Brain Barrier
BP	Black phosphorous
BSA	Bovine serum albumin
CNTs	carbon nanotubes
^oC	Celsius
Cd	Cadmium
C_3N_4	Graphitic carbon nitride
Co	Cobalt
cm	Centimetre
CVD	chemical vapour deposition
DAPI	4',6-diamidino-2-phenylindole
DCFH-DA	Dichloro-dihydro-fluorescein diacetate
D.I	Deionised water
DLS	Dynamic light scattering
DMEM	Dulbecco's Modified Eagle Medium
DMSO	Dimethyl sulphoxide
DNA	Deoxyribonucleic acid
Dox	Doxorubicin
EDTA	Ethylene diamine tetra acetic acid
et al	and others
EtBr	Ethidium bromide
FACS	Fluorescence Activated Cell Sorting
Fe	Iron
FET	Field-effect transistor
FBS	Foetal Bovine Serum
FSC	Forward scatter
FRET	Fluorescence resonance energy transfer
g	Gram

GO	Graphene oxide
GSH	Reduced glutathione
h	Hour
hBN	Hexagonal boron nitride
H & E	Haematoxylin and Eosin
HCT	Haematocrit
HGB	Haemoglobin
hMSCs (hMSCs)	human mesenchymal stem cells
HOS	Human Osteoblast cells
HR-TEM	High Resolution TEM
i.p.	Intraperitoneal
i.v.	Intravenous
IAEC	Institutional Animal Ethics Committee
ICP-OES	Inductively Coupled Plasma Optical Emission Spectroscopy
ISO	International Organization for Standardization
JC1	5,5′,6,6′-tetrachloro-1,1′,3,3′-tetra Ethylbenzimidazolylcarbocyanineiodide
kg	Kilogram
LDHs	Layered double hydroxides
LPO	Lipid peroxidation
LPS	Lipopolysaccharides
M	Molar
MnO_2	Manganese oxide
MDA	Malonedialdehyde
MEM	Modified Eagle Medium
mg	Milligram
Mg	Magnesium
Mn	Manganese
min	Minutes
ml	Millilitre
mm	Millimetre
MMT	Montmorillonite
mM	Millimolar
MMP	Mitochondrial membrane potential
MoS_2	Molybdenum disulfide
MRI	Magnetic Resonance imaging
MTT	3-(4, 5-Dimethylthiazol-2-yl)-2, 5-DiphenyltetrazoliumBromide
$NaCO_3$	Sodium hydroxides
NAD	Nicotinamide adenine dinucleotide
NaDH	Nicotinamide adenine dinucleotide reduced
NaOH	Sodium hydroxides
nm	Nanometre

NIR	Near infra-red
NRU	Neutral red uptake
PEG	Polyethylene glycol
PBS	Phosphate Buffered Saline
PDI	Polydispersity index
PDT	Photodynamic therapy
PTT	Photothermal therapy
PI	Propidium Iodide
PS	Phosphatidylserine
RBC	Red blood cell
rGO	Reduced graphene oxide
RNA	Ribonucleic acid
RNS	Reactive nitrogen species
ROS	Reactive Oxygen Species
RPM	Revolutions per minutes
s	Second
SDS	Sodium Dodecyl Sulphate
SSC	Sideward scatter
TEM	Transmission electron microscopy
TiO_2	Titanium oxide
TiS_2	Titanium disulfide
TMDs	Transition metal dichalcogenides
TMOs	Transition metal oxides
TGA	Thermogravimetric analysis
WBC	White blood cells
WS_2	Tungsten disulfide
XPS	X-ray photoelectron spectroscopy
XRD	X-Ray powder Diffraction
Zn	Zinc

'TOXICOLOGY: BIOLOGICAL INTERACTIONS OF 2D Zn-Al LAYERED DOUBLE HYDROXIDES (LDHs) IN *IN-VITRO* AND *IN-VIVO* SYSTEMS'

SYNOPSIS

By

Ashtami Jayakumar

for the degree of

Doctor of philosophy

of

THE SREE CHITRA TIRUNAL INSTITUTE

FOR

MEDICAL SCIENCES AND TECHNOLOGY, TRIVANDRUM

The two-dimensional (2D) class of materials are been extensively discussed over the past few years and particularly after the mesmerizing accomplishments of graphene. Dimensionality is the prime factor responsible for the appealing characteristics of graphene and therefore its feasibility for diverse applications activated screening of other 2D materials. 2D materials own large surface area, high surface-to-volume ratio, and manipulable electrical, physical, chemical properties which expand the applicability for diverse requisites. Among the broad-ranging class of 2D materials, layered double hydroxides (LDHs) are a relatively recent entry to stretch forth its impact as a versatile functional material. LDHs are 2D clay materials with brucite-like positively charged layers, counterbalanced by water molecules and negative ions. LDHs are attested to suit as adsorbents, polymer additives, catalysts, delivery vectors, flame retardants, and tissue engineering scaffold materials. The distinctive positive aspects like high surface area, charge, ion-exchange capacity, intercalation ability, and high loading range furnish LDHs for proficient performance. All these key features of LDHs facilitate its pursuit for even biomedical applications such as drug delivery, vaccines and tissue engineering. Literature summary over the last decade also validates solid uphold of LDHs in medicinal applications. Even though there is a substantial increase in research exploring the use of LDHs for health-care-related scenarios, there is not much clear portrait of its toxicity available to form an out-and-out conclusion. Applicability of any material for medical usage essentially requires cross-checking its toxicity profile.

In this regard, we designed a work to address the toxicity concerns related to LDHs. To have a broader understanding of the compatibility of LDHs, both *in-vitro* and *in-*

vivo systems were chosen for the planned proposal. The hypothesis was that LDHs does not generate a harmful interaction at the cellular and *in-vivo* level leading to a toxic response. Inorder to prove the hypothesis, the aim was to evaluate the biological interactions of 2D Zn-Al layered double hydroxides (LDHs) in *in-vitro* and *in-vivo* systems. For the study, three objectives framed were as follows

Objective I: Synthesis and physico-chemical characterization of 2D Zn-Al LDHs using different techniques.

Objective II: Evaluation of cellular interactions of 2D Zn-Al layered double hydroxides in *in-vitro* systems.

Phase I: Cellular interaction of 2D Zn-Al LDHs with L929 fibroblast cells.

Phase II: Cellular interaction of 2D Zn-Al LDHs with human osteoblast cell line (HOS cells).

Objective III: Toxicity evaluation of 2D Zn-Al layered double hydroxides in rat model.

The thesis was condensed into six chapters. Chapter 1 noted the introduction, background of the study and rational behind the choice of material. The introductory part discusses in detail about the 2D class of materials, their fundamental properties, types and relevance. The chapter also gives a brief introductory on 2D clay materials. The first chapter also highlights the applications of 2D materials.

Chapter 2 portrays the literature review on 2D clays and their importance. The chapter enlists the different types of 2D clay materials, their synthesis methods, structural

features and characterization techniques required for proper elucidation of structure as well as physico-chemical properties. The application and toxicity of 2D clays are also profiled in this chapter.

The materials and methods used for the work were written down in the 3rd chapter. The hypothesis, aim, work plan and methodologies adopted were described in detail. The motivation behind the study, justification for the selection of the materials as well as *in-vitro* cell lines were also specified. The methodology section involves three parts. The first part includes the synthesis protocol and characterization techniques used for the fabrication of Zn-Al LDHs. The synthesis of Zn-Al LDHs using the co-precipitation method and then characterized using transition electron microscope (TEM), dynamic light scattering (DLS), X-ray diffraction (XRD), Raman spectroscopy, Fourier transform-infra red (FT-IR) spectroscopy, thermogravimetric analysis (TGA), differential thermal analysis (DTA) and Zeta-potential were enlisted attentively.

The second part involves two phases, Phase I; methodologies chosen for marking the cellular interactions of 2D Zn-Al LDHs with L929 cells and Phase 2; methodologies opted for sketching the cellular interactions of 2D Zn-Al LDHs with HOS cells. Zn-Al LDHs of concentrations 10, 20, 40, 80 and 160µg/mL were exposed to L929 and HOS cells in respective study phases. For the phase 1 of second phase, cellular uptake of Zn-Al LDHs when exposed to L929 cells was confirmed byflow cytometry . The cell viability, mitochondrial activity and lysosomal function of L929 on treatment with Zn-Al LDHs were confirmed with MTT and neutral red uptake (NRU) assays. The chances for oxidative stress on exposure to Zn-Al LDHs were marked using the

DCFH-DA assay. The integrity of actin-filaments post-exposure to Zn-Al LDHs was confirmed by rhodamine-phalloidin staining. DNA laddering and 4′,6-diamidino-2-phenylindole (DAPI) staining were used as methods to perceive any chances of nuclear damage. Since the synthesized LDHs contain Zn^{2+} and Al^{3+} ions, chances of leach out toxicity were analysed using MTT, neutral red and DCFH-DA assays. To further confirm the impact of LDHs treatment on cellular interactions, calcein-AM staining of treated L929 cells was done. The chances of apoptosis in L929 cells when in association with LDHs were examined with Annexin-PI staining and analyzed with flow cytometry analysis.

For phase II of objective II, effect on cell viability of HOS cells on exposure to Zn-Al LDHs was inspected with the help of MTT assay and live dead assay using acridine orange-ethidium bromide (EtBr) staining. The outcome on the mitochondrial function when subjected to LDHs exposure was inferred from MTT as well as JC1 staining. The consequence of LDHs treatment on HOS cell morphology was checked using Coomassie brilliant blue staining and Giemsa staining. Reactive oxygen species (ROS) generation in HOS cells which fit-out to be an important marker for oxidative stress was quantified by DCFH-DA assay. The potential risk of Zn-Al LDHs on the cell membrane was analyzed using lactate dehydrogenase assay. The organelle integrity (specifically actin filaments, nucleus and lysosomes) post-exposure to Zn-Al LDHs was examined with the help of fluorescent dyes like rhodamine-phalloidin, DAPI and acridine orange.

For the third part, Wistar rats were chosen for understanding the effect of Zn-Al LDHs exposure at *in-vivo* level. Twelve rats were categorized into 4 groups for the study.

The first group with three Wistar rats was classified as the control group and was injected with saline intra-peritoneally. The next three groups with three rats each were given a dose of 10 mg/Kg of Zn-Al LDHs via intra-peritoneal (i.p) injection and were sacrificed on 3rd, 7th and 14th day respectively. The parameters overlooked for analysis were clinical and behavioral changes, gross pathology, hematology, blood biochemistry, urine, anti-oxidant levels, immunotoxicity, biodistribution and histopathology. Throughout the study period, the rats were checked for any clinical signs, specifically general appearance (like posture, piloerection, stimuli response to the surroundings, dehydration, weight loss, swelling, movements, *etc.*), eyes, skin, fur, nose, mouth, ear, respiration and excretion as well as for behavioral patterns like eating, drinking, grooming and movement. Body weights of rats on the 0th day and final day of sacrifice were documented. Blood and urine samples were collected from rats on the day of sacrifice. Collected blood were subjected to hematology, biochemistry and Inductively Coupled Plasma-Mass spectrometry (ICP-MS)-analysis. Urine analysis was done and a comparison for the different parameters between the test group rats and the control groups were logged. Gross pathology of the sacrificed rats was done and brain, kidney, liver and spleen were collected for further analysis. The chances for induced oxidative stress in liver and brain on exposure to Zn-Al LDHs were inspected using anti-oxidant assays. The biodistribution of Zn-Al LDHs on i.p administration was examined using ICP analysis. The chances for immunotoxicity were scrutinized with the help of splenocyte proliferation assay. Histopathology analysis of liver, kidney, spleen and brain was done using Hematoxylin & Eosin (H&E) staining to examine the possibility of tissue damage on the administration of Zn-Al LDHs.

The 4th and 5th chapter includes the results and discussion of the study respectively. Both the chapters consist of three main parts. The first part of 4th chapter comprises the outcome of synthesis and characterization techniques carried out for authenticating the proper formation of Zn-Al LDHs. The results of the adopted co-precipitation method and inferences obtained from the different physico-chemical characterization of the synthesized material; along with the previous literature support is discussed in the initial part of chapter 5. Zn-Al LDHs was synthesized using the co-precipitation method with nucleation in ice-cold condition and growth at hydrothermal condition. According to TEM analysis, the synthesized Zn-Al LDHs showed an average size of 102 nm and characteristic hexagonal morphology. The XRD analysis confirmed Zn-Al LDHs hexagonal lattice with 3R symmetry with d spacing, a and c values as 0.75 nm, 0.307 nm and 2.25 nm respectively. All the fundamental functional groups were evident in FT-IR and Raman spectra confirming the formation of Zn-Al LDHs. FT-IR examination showed the characteristic peaks for OH group, H_2O bending vibration of interlayer water, and intercalated carboxylate anion, Metal-oxygen (M-O) bonds at 3361.92, 1621.77, 1340.5, 734.87, 677 and 541.9 cm^{-1}conforming LDH structure. Similarly, in Raman spectra the corresponding peaks for CO_3–H_2O bridging at 3471 cm^{-1}, absorbed Carbonate at interlayers at 2921 cm^{-1}, vibrational modes of carbonate at 1388cm^{-1} and 1052 cm^{-1}, interlayer water at 1435 cm^{-1} as well as metal-oxygen peaks at 555, 495 and 152 cm^{-1} further validated the formation of Zn-Al LDHs with carbonate as the anion. Thermal stability of synthesized Zn-Al LDHs was done using TGA analysis. A total weight loss of 38.16% was observed when synthesized Zn-Al LDHs was subjected to a temperature range from room temperature to 850^0 C. The weight loss corresponds to the elimination of adsorbed water molecules, dehydration

of the layers, elimination of carbonate ions and formation of mixed metal oxide. Added to it, DTA analysis showed continued dehydration and dehydroxylation of layers in two-step reactions at 165^0C (removal of physisorbed and interlayer H_2O) and 250^0C. Interlayer anion decomposition was observed between 250^0 C and 350^0C. Peak beyond 312 denotes collapse of the layered structure. The hydrodynamic size of Zn-Al LDHs in ethanol and culture media was found to be 136.2 nm and 102 nm respectively. Zeta potential analysis revealed the charge of Zn-Al LDHs to be +24.3 approving the formation of brucite layers.

The second part of 4^{th} and 5^{th} chapters comprises the results and discussion of *in-vitro* analysis. In phase 1, the consequences of LDHs exposure on L929 cells were evaluated. Dose-dependent increment in cellular uptake was observed in L929 cells when treated with Zn-Al LDHs for 24h. The cell viability and mitochondrial function of L929 cells showed a non-toxic response when subjected to Zn-Al LDHs for different time intervals of exposure (3 h, 6 h, 24 h and 48 h). The lysosomal activity of L929 cells was not interrupted with Zn-Al LDHs uptake as per the results of cross-examination using neutral red uptake (NRU) assay and acridine-orange staining. As per the DCFH-DA assay, no significant deviation in ROS production was observed for L929 cells treated with 10, 20, 40, 80 and 160 µg/mL in comparison to the control group (without any treatment). Actin filaments were found to be healthy even after contact with Zn-Al LDHs as per the conclusion from rhodamine-phalloidin staining. No nuclear condensation was observed in DAPI staining when L929 cells were introduced to Zn-Al LDHs. In addition to that, no DNA fragmentation was observed in DNA isolated from L929 cells when in contact with different concentrations of Zn-

Al LDHs, suggesting an absence of genotoxic potential. The live-dead assay using calcein-AM PI staining showed non-toxic interactions in L929 with Zn-Al LDHs. The chances for apoptosis-mediated cell death mechanism were analyzed by FACS using Annexin/PI staining. The data showed that cells treated with 10, 20, 40 µg/mL of Zn-Al LDHs showed a population similar to that of the control untreated group but for treatment groups with 80 and 160 µg/mL of Zn-Al LDHs there was an observed increase in the population of cells in the early apoptotic stage. The overall viability of cells in even the highest concentration (160 µg/mL) treatment group was above 80%. Besides the direct toxicity check, the leach-out toxicity study using MTT, NRU and DCFH-DA assays also showed no evidence of adverse effect on L929 cells.

For the second phase, a follow-up of the study carried out to examine the interactions of HOS with Zn-Al LDHs was noted and discussed. The cell viability of HOS cells post-exposure to the highest concentration of 160 µg/mL of Zn-Al LDHs were 98.5%, 87.1% and 82.5 % for an exposure time of 2 h, 24 h and 48 h respectively. The mitochondrial activity of HOS cells after coming in contact with Zn-Al LDHs was not deteriorated as evident from both MTT and JC1 staining results. The morphology of HOS cells showed no visible changes in both Giemsa and Coomassie's brilliant blue staining. The ROS production in the treatment groups did not show any evident deviation in comparison to control for 3h and 24 h exposure. For 48h treatment, a small increase in ROS production was observed in treatment groups though not significant. An increase in lactate dehydrogenase release was observed in HOS cells treated with higher concentrations of Zn-Al LDHs relative to the control HOS cells. The actin filaments were found to be maintaining the integrity even after LDHs treatment for

24h as per the rhodamine-phalloidin fluorescent staining. The nuclear integrity of HOS cells was seen to be unharmed despite being exposed to Zn-Al LDHs. The lysosomal function was also not disturbed in HOS cells upto the highest selected dose concentration of 160 µg/mL. Live dead assay showed a dose-dependent increase in dead cells but no drastic shift from green to red was observed which suggests no apparent toxic response.

Third last part of 4th and 5th chapters appends the results and discussion from the *in-vivo* toxicity studies. There were no clinical symptoms observed after administration of 10 mg/Kg of Zn-Al LDHs in rats. Gross abnormality or observable lesions were not found during the examination. Hematological parameters showed variations compared to the control group but were in the normal range. Albumin, protein, and creatinine, levels in serum were found to be comparable to control. Whereas alternations were observed in cholesterol, glucose, aspartate aminotransferase (AST), alanine aminotransferase (ALT) and alkaline phosphatase (ALP) levels when compared to control animals' values. Urine analysis showed normal range when exposed to LDHs. Anti-oxidant levels showed fluctuations as an adaptive response to LDHs exposure. The biodistribution study indicated the presence of Zn and Al in the brain, kidney, liver and blood. The histopathological evaluation indicated periportal infiltration and reactive hepatocytes in the liver on 3rd and 14thdays. The histopathology of brain, kidney and spleen of all the three treatment groups was normal in comparison to control organs. Further long-term toxicity studies will be required to confirm this observation.

The sixth chapter comprehends the summary of the conducted work. Zn-Al LDHs was successfully synthesized by the co-precipitation method. The physico-chemical characterization confirmed Zn-Al LDHs formation. The synthesized LDHs of average size of 102 nm showed a harmless interaction at the cellular level in HOS and L929 cells. Histopathological analysis showed a slight number of reactive hepatocytes on exposure to Zn-Al LDHs while no adverse effect was evident in the kidney, spleen, and brain. Additional long-term and chronic toxicity studies will be needed to claim the Zn-Al LDHs to be a safe nanomaterial for biomedical applications.

INTRODUCTION

1 INTRODUCTION

1.1 Two-dimensional materials

Two-dimensional (2D) materials are trending in research disciplines on strength of their impressive physicochemical properties attributed to their dimensionality. 2D materials as per definition comprise materials having one dimension restricted to the nano-range [Zamora *et al*., 2010]. Dimensionality beholds a controlling role in material characteristics as apparent from the difference in properties of carbon in its different dimensions i.e, fullerene (Zero-dimensional-0D), carbon nanotubes (one-dimensional-1D), graphene (2D) and graphite (three-dimensional-3D). The 2D materials offer layered structures with high surface area making them potent for various applications with high functionalities [Jayakumar *et al*., 2018].

Graphene remains the most celebrated 2D material for its long list of positive attributes like its mechanical/ electrical properties, thermal conductivity, high surface area, and other tuneable functionalities. The abovementioned characteristics ease its applicability on multiple grounds. For instance, graphene is probed functional for electronics, material science, and medicinal applications. The fame of graphene in recent times has indeed stimulated the expedition for other 2D materials. Transition metal dichalcogenides, black phosphorous, 2D clay materials, transition metal dioxides, hexagonal boron nitride *etc*., are other important members of the 2D materials classification. Most of the listed 2D nanomaterials have proved successful in achieving the required functionality in material science and medical applications [Kurapati R *et al*., 2014]. 2D materials possess interesting chemical, mechanical, and optical properties. Furthermore, they hold appreciable biocompatibility so that they can be potentially translated for various biomedical applications. Infact, 2D materials are found helpful for regenerative medicine, drug delivery, tissue engineering, biosensor, photothermal therapy (PTT), anti-microbial activity, and magnetic resonance imaging (MRI) *etc*., The thin layered structure of 2D material provides a

high surface area that can be utilized effectively for loading drugs or other molecules of interest, providing the possibility of highly efficient loading for therapeutics. The thin layered structure also improves effective response against external light stimuli which can be used for PTT or photodynamic therapy (PDT) [Chimene, D *et al*., 2015].

2D materials exist as either single layers or as sheets of a few-layer thickness. Synthesis of 2D materials is through two main approaches: (1) Top-down and (2) Bottom-up (Figure 1.1). Top-down techniques involve the exfoliation of 2D materials as layers from bulk counterparts through the application of either thermal energy, mechanical force, use of large/ charged counter ions, or with the help of surfactants.

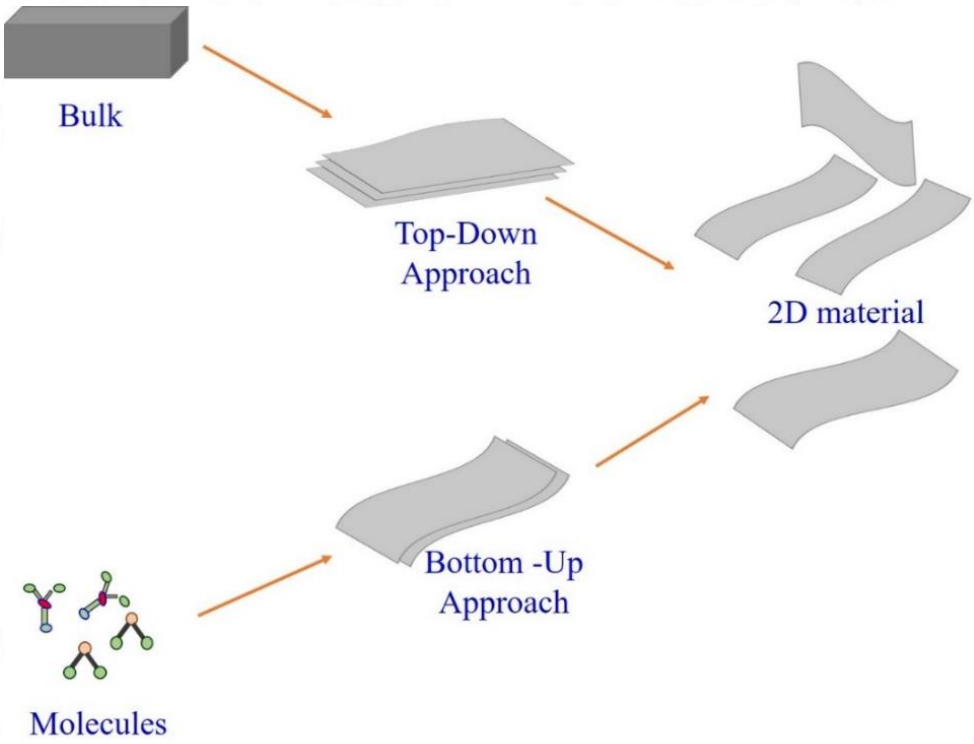

Figure 1.1: Different approaches for the fabrication of 2D structures

The other way around, bottom-up techniques involve wet synthesis that is based upon building up the layered structure from molecular scale. Important bottom-up methods used for obtaining required 2D structures are chemical vapour deposition (CVD),

atomic layer deposition technique (ALD) as well as wet synthesis like co-precipitation [Jayakumar *et al*., 2018].

1.2 2D nanomaterials and their importance in the present era

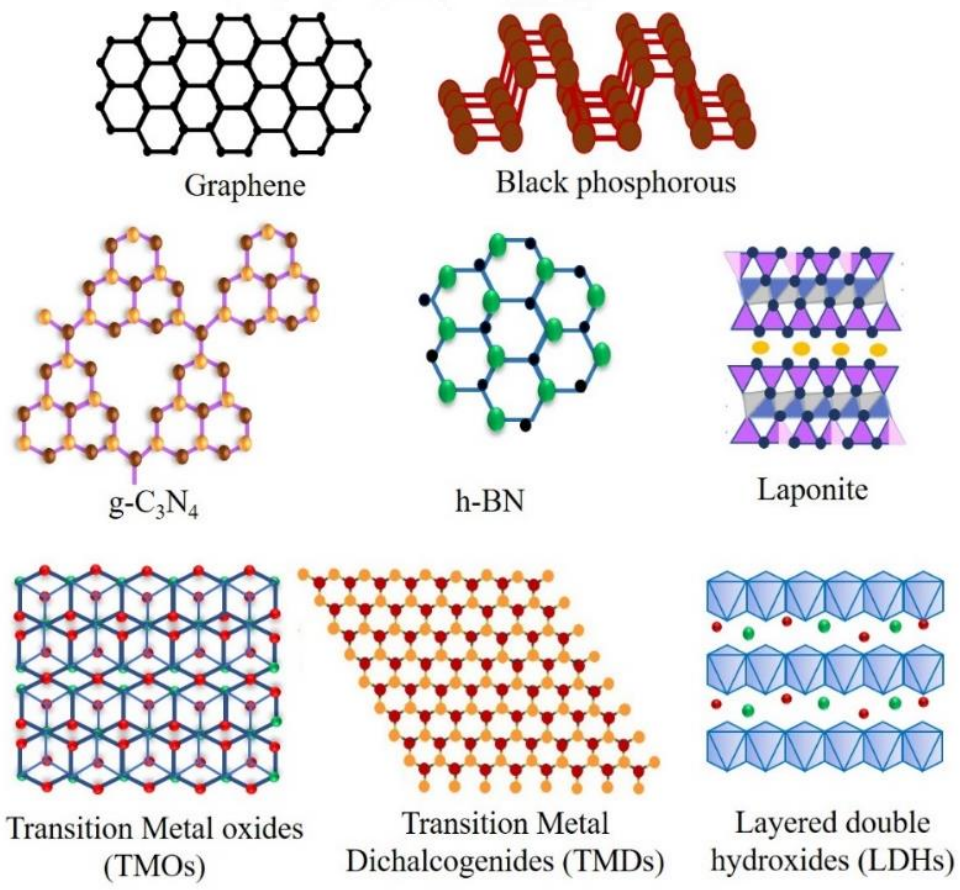

Figure 1.2: Different 2D materials

The 2D materials have one dimension reduced to atomic layer thickness, while the other two dimensions have a larger size. The 2D planar structure displays far-fetched properties compared to bulk counterparts. The large surface area, surface chemistry, charge, optical advantages and most importantly quantum effects of 2D structures smoothen the executions of chemical as well as physical treatments which further enhance its multimode functionalities. Graphene is a classic example of 2D materials

that possesses assorted application possibilities [Banerjee *et al*., 2018]. Following the current sensation stirred up by the fascinating properties of graphene, researchers are now checking out other 2D materials. The expedition into the family of 2D materials has outshone a bunch of interesting materials endowed with engrossing properties (Figure 1.2).

The high surface area, drug loading possibility on either side of the 2D plane, π electron delocalization facilitating drug-bonding and better biocompatibility boost graphene as an ideal drug delivery agent [Zhang H et al., 2020]. Additionally, 2D materials with their appreciably high mechanical strength and better biological interactions without compromising cellular integrity pave the way for tissue engineering as an excellent scaffold material that could promote osteogenic differentiation [Zhang *et al*., 2019]. Furthermore, the photoluminescence property, near infra-red ray absorption capacity together with high mechanical strength and rigidity makes 2D materials, especially TMDs favourable for bioimaging. These central properties forge TMDs as a typical option for bioimaging as well as PTT or PDT treatments which demands a quick and effective response to external stimuli [Agarwal *et al*., 2013]. To add on, the anti-microbial properties exhibited by 2D materials like 2D clays can be utilized for wound repair applications [Munhoz *et al*., 2019]. The electrical conductivity, tuneable band gap, optical properties, vast surface area, and high sensitivity to changes in environmental conditions of 2D materials are highly recommendable for biosensing applications. TMDs and TMOs show outstanding light absorption ability, fluorescence quenching and electron transfer rates that can be rendered for chemical and biosensing applications based on the fluorescence resonance energy transfer (FRET) mechanism [Deng *et al*., 2011].

2D materials are being explored for multimode applications that combine diagnosis and therapeutics. As discussed earlier, 2D materials are ideal for targeted drug delivery, at the same time, the optical properties can be tuned for *in-vivo* imaging and photothermal therapy. 2D materials especially TMDs (MoS_2, WS_2 *etc*) can cause deep

tissue penetration of ultrasound, create sensitive near infra-red (NIR) response, superparamagnetic property and radioactivity. This combination is meritious for stimuli-responsive targeted delivery of drugs with simultaneous *in-vivo* imaging and PTT/PDT activity opening the leeway for effective cancer theranostics.

Encouragingly, 2D materials can adapt to even the latest advancements in biomedical and material research. 2D materials also exhibit promising scope in fulfilling the rising demands [Marian *et al*., 2022]. In situ implantation is one of the very recent breakthroughs in healthcare applications that centralize real-time analysis and allow personalized diagnosis. Graphene-based materials have now been explored for in-situ sensor implant applications owing to their inert nature, flexibility, mechanical properties and biocompatibility. Anti-microbial peptide-loaded graphene was used to develop an in-situ sensors for continuous and sensitive detection of Helicobacter *pylori* bacteria [Cheng *et al*., 2017]. The approach of using CVD graphene helped in achieving a non-invasive detection of bacterial infection. As per reports, graphene derivatives are capable of recording electro-cardio signals of soft tissues like neuronal and cardiac tissues with high performance and stability. Modification of graphene derivatives into hydrophilic ones further enhanced its application scope due to improved compatibility. The optical properties and electrical conductivity of graphene helped in attaining its functionality as a neural implant with an additional feature of *in-vivo* imaging. *In-vivo* imaging at the neural site was made possible with the ability of graphene to respond to light stimuli [Kang *et al*., 2017].

1.3 Types of 2D materials

1.3.1 Graphene, graphene oxide (GO) and reduced graphene oxide (rGO)

Graphene remains the most checked-out 2D material so far. This carbon allotrope in sp^2 hybridization with a hexagonal planar structure has a typical honeycomb structure and is hydrophobic in nature. The oxidized structure of graphene, GO is also widely

discussed and explored as a graphene derivative. GO also exhibit a honeycomb structure but contain sp^3 hybridized carbon in contrast to graphene [Geim*et al*., 2007]. Therefore, GO is hydrophilic in nature. GO is reduced using various reducing agents to obtain another form of graphene, namely reduced graphene oxide (rGO). The reduction of GO results in the elimination of functional groups present and therefore rGO exhibits partial sp^2 characteristics but holds more structural defects than graphene [Gutiérrez *et al.,* 2022]. The chemical structures, mechanical features, electrical and optical properties of graphene, empower graphene to rule multiple research frontiers and application scenarios. Apart from the electrical, optical and mechanical applications, graphene is also enrooting its influence in providing more advanced and improved medical proficiency. Graphene increases mechanical strength when used as additives in hydrogels thereby improving its potential in tissue engineering applications without causing any integrity damage to the cellular environment and organelles. Graphene-based hydrogels also showed better cellular adhesion, proliferation, and differentiation of human mesenchymal stem cells (hMSCs), thereby facilitating osteogenic differentiation [Lee *et al*., 2014].

The strength and conductivity of GO are low compared to graphene, but the improvement in hydrophilicity makes them optimal for biomedical applications that demand good water dispersion. The hydroxyl (OH) group present in graphene improves hydrophilicity, cytocompatibility, and interaction with proteins, cellular matrix and blood [Singh *et al*., 2018]. GO nanosheets show repulsion with individual sheets depending upon the pH and this characteristic of GO is used for the fabrication of pH-responsive composite. The presence of a large amount of carboxyl (COOH) groups at GO surface facilitates the conjugation of biomolecules to these reactive sites and thereby improves the chances of neuronal interactions. Graphene and its derivatives are recently much spotted for neuronal regeneration applications and research outcomes show some highly promising scope [Goenka *et al*., 2014].

rGO has been explored for biosensor, PDT and PTT applications because of its electrical properties. There are also newer graphene derivatives like fluorinated graphene, graphyne, graphdiyne that are under study. The high surface area and charge carrier mobility facilitate rGO to load high amounts of biomolecules on its surface, making rGO well-suited for high sensitive biosensor applications. rGO-based FET biosensor has been fabricated and reported to be efficient in sensing prostate-specific antigens with high sensitivity [Cheng *et al*., 2017]. As per literature updates, rGO absorbs about 20% of irradiated NIR light with the help of a large number of π- π bonds present and is, therefore a more efficient, cheaper substitute for PTT/PDT therapy compared to GO, gold nanoparticles and carbon nanotubes. Surface modification of rGO further accelerates the efficiency profile of rGO by easing drug loading and targeted release [Akhavan *et al*., 2012].

1.3.2 Transition metal dichalcogenides (TMDs)

TMDs are layered structures consisting of chalcogen layers sandwiching transition metal monolayers. The discrete layers are held together by van der Waal forces. The most explored TMDs are molybdenum disulfide (MoS_2), tungsten disulfide (WS_2) and titanium disulfide (TiS_2). The tuneable bandgap, NIR responsive nature, catalytic properties, photoluminescence, optical and electrical characteristics, of TMDs makes them attractive for various biomedical applications. TMDs in bulk form have indirect bandgap but interestingly when confined to 2D, bandgap changes to direct band gap. This property gives an added advantage over graphene which has zero band gap. The zero band gap of graphene is the limiting factor in its feasibility for semiconductor applications. The bandgap increases with decreasing the layer thickness. This possibility for fine-tuning the band gap by adjusting the layer thickness of TMDs further highlights its significance in nanoelectronics. Direct band gap and appreciable semiconducting properties spur further exploration of TMDs. The sensitive response of TMDs to external NIR stimuli showcases their potential in PDT and PTT therapy.

TMDs are highly recommended for biosensor applications demanding high sensitivity and resolution [Wang *et al*., 2017].

One of the most celebrated biomedical applications of TMDs is its significance in overcoming the long-time hurdle of sequencing single DNA molecule. TMDs are engineered into atomically thin nanopores for effective DNA translocation with high sensitivity. The use of TMDs for nanopore sequencing has surprisingly increased the resolution capacity from 20 nm to less than 1nm. The intrinsic direct bandgaps of TMDs are responsible for achieving such remarkable outcomes in nanopore sequencing. The wider span of voltage that can be applied to TMDs and the added advantage of having no need for any surface modification to prevent strong affinity with DNA also makes TMDs preferable for sequencing [Liu *et al*., 2014].

1.3.3 Black phosphorous (BP)

Black phosphorous is nicknamed as the phosphorous analog of graphene [Wu *et al*., 2018]. BP turns out to be the most stable allotrope of phosphorous and holds many distinctive properties that drag BP to the limelight. Interestingly, BP has a honeycomb structure similar to that of graphene. Each of the phosphorous atoms in the BP structure is connected to three other phosphorous atoms. BP exhibits good carrier mobility, layer-dependent band gap, and absorption at the NIR range that cause progressive results in drug delivery, biosensors, bio-imaging, and PDT/PTT therapy [Luo *et al*., 2019]. Fascinatingly, BP is explored for multimode functionality in theranostic applications since BP provides simultaneous drug cargo, targeted delivery, *in-vivo* imaging as well as NIR-dependent PDT and PTT treatment. Furthermore, biocompatibility and biodegradability at a faster rate optimize BP for biomedical applications. The presence of lone pairs at phosphorous atoms in BP structure makes them highly prone to oxidation in the presence of air, making them vulnerable to degradation. Though the instability of BP is a hindering factor, surface functionalization/ doping can overcome this limitation and help in achieving the

requisite demand [Choi *et al.,* 2018]. Ligand coordination/ encapsulation with stable materials are techniques adapted to enhance the stability of BP. TiL_4 coordination to BP is stated not only to augment its stability but also to reduce the other negative attributes of BP like inflammation, ROS production and oxidative stress [Qu *et al*., 2017].

1.3.4 2D clay

2D clay materials are recently gaining notice for their attractive characteristic properties that hold potential worth in medicine, especially but not limited to drug delivery and tissue engineering. 2D clay materials consist of two broad classifications- silicate clays and Layered Double Hydroxide (LDHs). Silicate clays are 2D clays of diameter 10-100 nm with phyllosilicate minerals of varying chemical composition. Important silicate clays are montmorillonite (MMT), Laponite, saponite and hectorite. Silicate clays are negatively charged at the faces and positively charged at the edges [Dawson *et al.,* 2013]. On the other hand, LDHs are hydrotalcite-like materials with general formulae $M^{2+}_{1-x}\, M_x^{3+}(OH)_2\, [A^{p-}_{x/p}]^{x+}.m\, H_2O$. LDHs are anionic clays of metal ions surrounded by hydroxyl groups forming 2D sheets held together by anions present at the inter-layer space. LDHs' metallic layers consist of positively charged divalent cations and trivalent cations forming a brucite-like structure [Nalawade *et al.,* 2009]. The charged surface of 2D clays along with a high surface area facilitates heavy drug loading for targeted delivery. 2D clays also show remarkable efficiency as absorbent. 2D clays are reported to improve the mechanical strength of scaffolds and therefore find good functionality in tissue engineering, especially for bone tissue regeneration.

1.3.5 Transition metal oxides (TMOs)

TMOs exhibit wide bandgap properties that make them an appreciable candidate for nano-electronics. TMOs are most intensely explored for drug delivery and MRI. TMOs have unique electrical and photochemical properties, ferromagnetism, thermal

resistance, and redox potential properties. Titanium dioxide (TiO_2) and manganese dioxide (MnO_2) are the two TMOs that are most exploited. MnO_2 nanosheets find potent scope in biosensing, imaging, and drug delivery applications. PEG-functionalized MnO_2 nanosheets not only enhance the stability of the material but also exhibit potent drug delivery applications. PEG functionalized MnO_2 loaded with doxorubicin effectively executed targeted delivery at tumour site with high efficacy. The fabricated nanosheets also increased MRI signal intensity at the tumor site. The mechanism of action was by breaking down of sheet into consequent metal ions. MnO_2 exhibit multi-functionality in treating cancer by simultaneously performing maximum drug loading, targeted drug delivery and MRI imaging of tumour site [Omomo *et al.,* 2003].

1.3.6 Graphitic carbon nitride

Graphitic carbon nitride (C_3N_4) is a less explored member in the 2D family of nanomaterials. C_3N_4 is known to be graphene analog and is also an organic semiconductor. C_3N_4 is made of layers containing carbon and nitrogen atoms substituted in a consecutive manner. The type of interaction involved in C_3N_4 is covalent bonding between carbon-nitrogen atoms and van der Waal interactions between layers. The resulting structure is highly stable. Graphitic carbon nitride exhibits suitable band gap and thermal stability suitable for electronic and semiconductor applications. g-C_3N_4 shows high stability towards acids, bases and organic solvents. Dispersion of g-C_3N_4 is comparatively effortless due to charge repulsion between layers. Strong photo-adsorption, quick response to light stimuli, and enhanced cellular compatibility C_3N_4 make them an ideal choice as biosensors [Liao *et al.,* 2020].

1.3.7 Hexagonal boron nitride (hBN)

Hexagonal boron nitride is nick-named as white graphene. hBN holds structural similarities with graphene for the reason both have got honeycomb structures with

hexagonal lattice. hBN in contrast to carbon in graphene, has alternatively arranged boron and nitrogen atoms [Weng *et al*., 2016]. The boron-nitrogen bonds in hBN sheets impart higher polarity than C-C bonds in graphene sheets and therefore properties of hBN are different from those of graphene. Interestingly, hBN sheets also exhibit UV-dependent luminescence and have a wider bandgap that is remarkably convivial for electronic applications. hBN is thermally and electrically stable which promotes its usage in various fields. The non-toxic profile of hBN favours biomedical applications such as bioimaging, sensor, and drug delivery. The low dispersity of hBN in water depreciates its usage as a drug delivery vector. But this obstacle is being resolved by functionalization. Hydroxylation of hBN enhances its solubility. Water soluble hBN obtained by hydroxylation using boric acid substituted C_3N_4 showed enhanced drug loading capacity and biocompatibility. The hBN sheets after hydroxylation showed doxorubicin (Dox) loading capacity of 300% of its weight. Additionally, the hydroxylated hBN could achieve targeted release of the loaded drug depending on pH change. The loaded Dox was released at acidic pH, notably at lysosomes having pH in the acidic range. From a cancer therapy point of view, hydroxylated hBN is recommendable as per the obtained results which demonstrate a reduction of tumour cell population to 20%. hBN undergoes cellular uptake by endocytosis, making cell penetration and cellular availability much easier without any compromise on cellular integrity. Therefore, hBN is a good biocompatible choice for live cell imaging, drug delivery *etc.,* [Weng, Q *et al.,* 2014].

1.3.**8 Silicene and germanene**

The mono sheets of silicone and germanium, namely silicene and germanium are the newer additions to the lined-up 2D class of materials. They have honeycomb-like structures similar to graphene and also comparable electrical conductivity. They are grown epitaxially on a substrate in contrast to graphene, which can be exfoliated to form independent sheets. Both silicene and germanene show remarkable flexibility as

well as compressibility. The option of regulating electrical and thermal conductivity by adjusting the stain is a highlighting characteristic of both. Germanene and silicene are structurally very stable and have high conductivity making them epitome for nanoelectronic applications [Ni *et al*., 2012]. Antimony and bismuth analogs of this class have been reported very recently and are named antimomene and bismuthine respectively [Pandey *et al.,* 2021].

1.4 Surface/ chemical functionalization, doping and composite formation.

Functionalization is one vital step towards augmenting the outreach of 2D materials for various fields. Functionalizing the 2D material has indeed aided in increasing its dispersity in various physiological mediums, preventing aggregation, enhancing stability, improving biocompatibility, providing improvisation by adding specific functionality and specificity as per demands, and. The two main types of chemical functionalization are (1) covalent functionalization and (2) non-covalent functionalization. Covalent functionalization involves the direct bonding of 2D materials with specific organic molecules forming stable products. Non-covalent functionalization implicates weaker interactions like physisorption. The mode of functionalization is chosen as per the requirement of a specific function [Martin *et al.,* 2010].

2D material composites are fabricated to achieve either improved or synergic functionality. In a composite, two or more materials are being combined to get a specific applicational decisive factor. Some of the 2D materials have got complementary properties just as in the case of LDHs and graphene, LDHs are chemically reactive but have very low conductivity while graphene is highly conductive but possesses inert chemical behavior. Both suffer from the common demerit of aggregation of individual layers. Interestingly, combining LDHs and

graphene helps in beating the aggregation issues. Also, composite of graphene and LDHs are reported to show better performance as catalyst, adsorbent, electrode and fillers [Cao *et al*., 2016].

Doping is another way to fine-tune the chemical and electrical properties of 2D materials. Doping help to modify the atomic structure and thereby alter the optoelectrical, chemical and mechanical characteristics of the materials as per demands. The doping helps improve and add functionalities so that the material finds applications in sensors and FET transistors with high sensitivity. Doping of TMDs with heteroatoms is reported to attain ferromagnetic properties for the material and thereby enhancing its application scope in magneto-optical devices. Also, doping graphene sheets with nitrogen atoms improves the efficiency of graphene as a biosensor by attaining more selectivity and sensitivity [Feng *et al*., 2017].

2D materials are widely used as fillers in polymer matrices in order to improve polymer performance. The high surface area and a large number of surface atoms in the case of 2D materials indeed make them suitable matrix fillers, since the matrix interaction is facilitated. Even the introduction of a very low amount of 2D materials as fillers in polymers is reported to improve its mechanical strength to 200% in assessment to polymer alone cases. Graphene, TMDs, hBN and many other 2D materials are already reported to be tried as a polymer additive typically in lithium batteries and energy storage. For the preparation of composite, 2D materials are initially exfoliated in order to reduce layer-to-layer interaction and later dispersed evenly in a polymer solution [M *et al*., 2019].

1.5 Applications of 2D materials

Confinement of bulk materials to two-dimension imparts interesting properties that expand their feasibility as multifunctional materials. 2D materials show tuneable electrical, mechanical, and chemical properties that make them advantageous for

various demands. The tuneable band gap property and appreciable thermal and electrical conductivity of 2D materials idealize them for optoelectronic applications. The large surface area, surface charge, active sites and possibility for intercalation into inter-layer space promote their identity as absorbent and catalyst. 2D materials also find potential scope as sensors and FET transistors. The previously mentioned characteristics of 2D materials also smoothen their use in energy storage devices. The space between individual layers facilitates accumulation as well as the release of lithium ions/charge/ molecules as demanded in the case of lithium-ion batteries [Cai *et al*., 2018].

The biomedical scope of 2D materials is far-reaching. 2D materials have marked their contribution in drug delivery, biosensors, bioimaging, tissue engineering as well as multimode applications like cancer theranostics [Kuang *et al*., 2010]. The high surface area and electron mobility favour selective detection of target biomolecules with high precision. The high surface-to-volume ratio of 2D materials helps them to quickly detect the stimuli with even slight variations in environmental conditions. The wide bandgap, high electron mobility, fluorescence property *etc.,* imparts high selectivity to sensors with minimum current leakage and paves the way for next-generation sensing applications [Rohaizad *et al*., 2021].

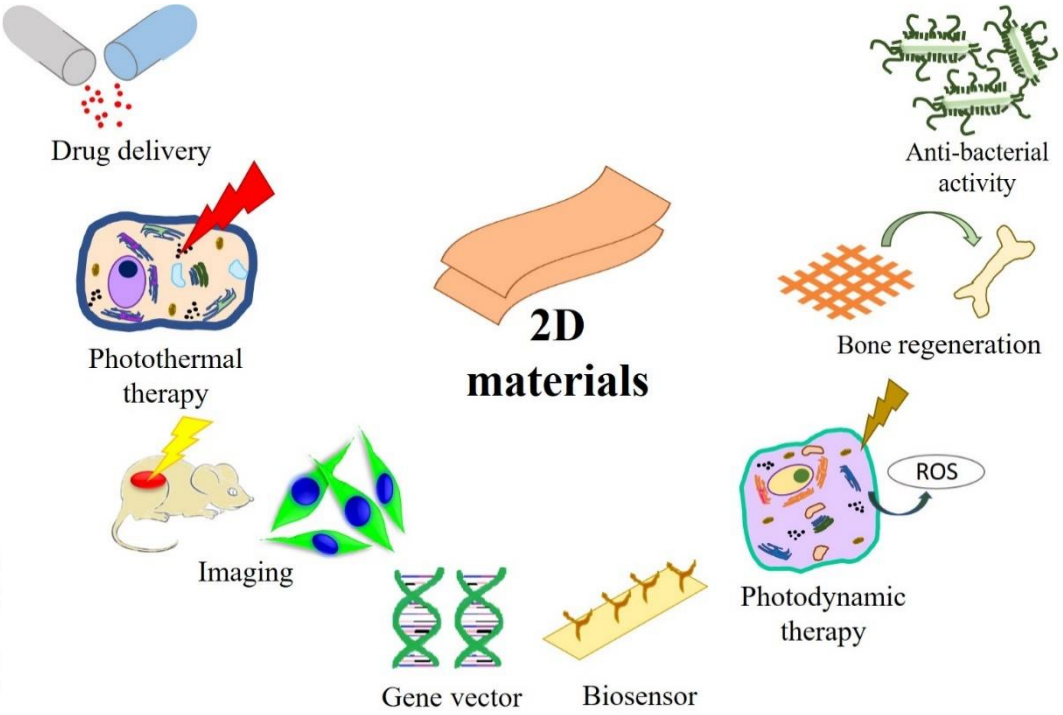

Figure 1.3: An overview on biomedical applications of 2D materials

2D materials also find a major hold as delivery vectors. 2D materials especially 2D clay materials are potentially excellent drug/gene vectors since the surface charge eases high drug loading and also cell internalization without any harmful effects on the cells. Multifunctional applications are also accomplished by 2D materials since they could exhibit collective properties of drug loading, fluorescence and responsiveness to NIR radiation. This competence of 2D materials is explored for cancer treatment where drug-loaded 2D materials could deliver loaded drugs at the target site in response to NIR stimuli. Apart from this, the NIR responsiveness of 2D materials and its ability to act as an efficient photosensitizer, for example in the case of TMDs are utilized for PTT and PDT therapy and shows successful reduction in tumour growth. The fluorescence property, high quantum yield and tuneable optical properties of 2D materials make them ideal for bioimaging [Chimene *et al*., 2020].

Initially, 2D research was dominated by graphene but recently other 2D materials like TMDs, black phosphorous and 2D clay materials were also opted and explored for more enhanced functionalities. 2D clay materials like layered double hydroxides (LDHs), laponite *e* have been explored for various healthcare applications, especially for drug/gene delivery and tissue engineering. The high surface-to-volume ratio, charged surfaces, biocompatibility and possibility for conjugation enhance its scope as a vector in drug delivery applications. 2D clay materials also possess potential reach in tissue engineering and anti-microbial coating as per reports [Wang C *et al*., 2014].

An important field that 2D materials are establishing is tissue engineering [Zheng *et al*.,2021]. 2D materials are reported to provide appreciable mechanical strength. 2D clays such as LDHs and silicate clays exhibit vital performance as biocompatible bone scaffolds promoting cell proliferation, osteoblast differentiation and bone regeneration. For example, Silicate clays like laponite show properties analogous to bioactive glass in bone and are notably osteoinductive, highly biocompatibility and have biodegradation profiles with non-toxic end products [Gonçalves *et al.,* 2014]. In addition, the anti-microbial property of 2D materials like LDHs actually promotes wound healing activity which is an add-on advantage for tissue engineering applications [Fernandes *et al.,* 2019].

1.6 General concepts in 2D clay

Clay materials have been known to possess multiple applications for ages. Traditional applications of clay material such as antacids, antiseptics, cosmetics *etc.,* are reported and known [Gorchakov *et al*., 2001]. The chemical composition of clay also makes possible its usage as a stabilizer and reinforcing material. Clays consisted of layered fine particles mostly from natural origin. Now, synthetic clays are also available and enclose biomedical application scop with enhanced homogeneous composition compared to natural clays. Clay usually consists of crystals of mixed metal ions mostly phyllosilicate minerals of different compositions [Gaharwar *et al.,* 2019]. Octahedral

and tetrahedral sheets are involved as building units for clay structures. The octahedral: tetrahedral sheets ratio, charge on the surfaces, inter-layer space, ion-exchange capacity and morphology of the clay particles are factors that classify the clay materials. Clay materials are subdivided into different families namely Serpentine-kaolin, smectite (or bentonite), and palygorskite-sepiolite [Mousa *et al.,* 2018].

Nanoclays, as per nanotechnological classifications, come under the classifications of 2D materials without a doubt. Nanoclays are layered structures divided by interlayer space of a few nanometer thicknesses. Nanoclays exists in different mineral composition and morphologies [Ke *et al.,* 2005]. MMT, bentonite, sepiolite, laponite, and LDHs are major 2D clays that are explored from an applicational point of view [Murugesan *et al.,* 2020]. 2D clays are broadly classified into silicate clays and LDHs. Silicate clays are 2D nanoparticles of a layered structure having a diameter range of 10-100 nm and a thickness of about 1 nm. The 2D layered silicate bears a net negative charge at the faces while the edges are positively charged. The surface charges associated with silicate clays procure them high drug loading efficiency as the drugs of opposite charge can be loaded onto the silicate layers with ease. Stability in the aqueous medium, shear thinning and biocompatibility are other characteristics of silicate clays that widen their application potential [Kurapati *et al.,* 2016]. 2D clays coming under the category of silicate clays are kaolinite, sepiolite, palygorskite and smectites. Important members of the smectite type of 2D clays are laponite, MMT, saponite and hectorite [Dawson *et al.,* 2013]. The lower charge densities makes the exfoliation of silicate clays much easier in comparison to LDHs clays.

Layered double hydroxides (LDHs) consist of positively charged metal ion layers held together by anions and water molecules present in the inter-layer space. LDHs have higher surface charge density compared to silicate clays and therefore require more advanced techniques for exfoliation into single sheets. LDHs can be prepared in

different metal compositions and inter-layer anions depending upon the application requisites [Nalawade *et al.,* 2009].

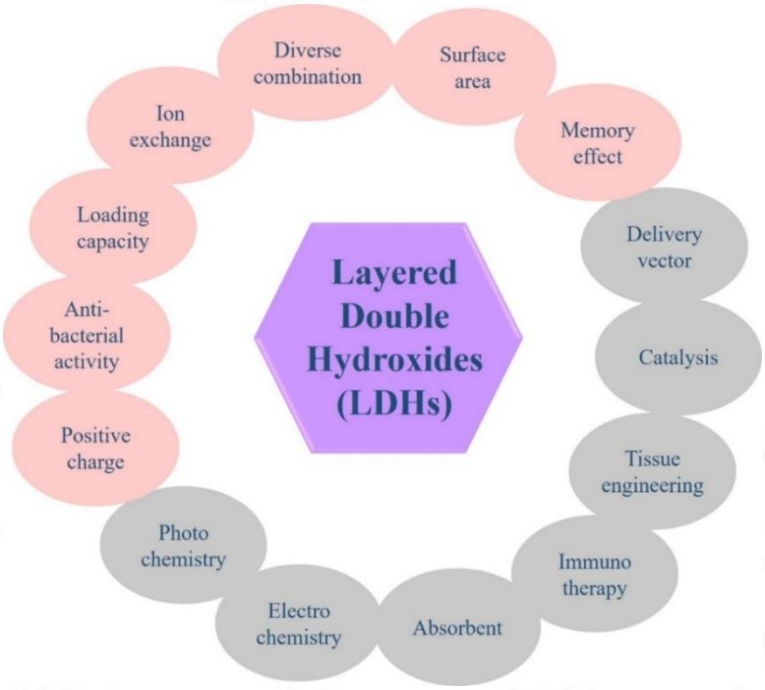

Figure 1.4 Applications of LDHs

1.7 2D clay and its importance in the present era

2D clay materials are now focussed primarily on various applications in both industrial and biomedical fields [Saikia *et al*., 2020]. The unique characteristics of 2D clay materials impart enlightening scope for functionalization. The surface charge of 2D clay materials imparts high reactivity to them. The high surface-to-volume ratio, in addition provides high adsorption capacity. 2D clays also possess the peculiar property of ion-exchange capacity. The ions at the inter-layer space of 2D clays can be exchanged with molecules having higher affinity; and this property opens up the wide scope of using 2D clays as adsorbent, drug/gene delivery vector *etc.,* The ability to bind biomolecules of interest at the clay surface by electrostatic interaction or by intercalation at the interlayer space using ion-exchange or by hydrophobic-hydrophilic interactions indeed further helps to load drugs, anti-inflammatory agents, growth

factors *etc.,* at the target site. The inclusion of 2D clay is also found to improve the mechanical strength, surface properties and degradation profile of scaffold materials used for bone regeneration [Mousa *et al*., 2018]. The anti-bacterial properties and corrosion resistance further make 2D clays ideal for various scaffold applications.

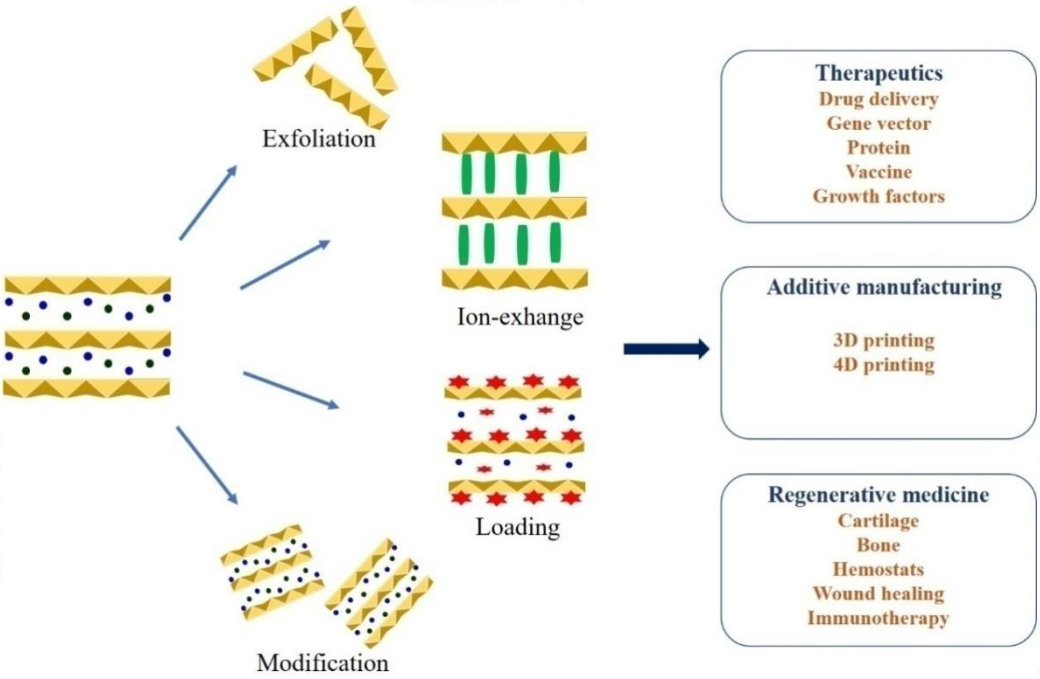

Figure 1.5 2D clays and their importance

The swelling capacity of 2D clays is very much influential on their reactivity. The kaolinite clays undergo no structural change and therefore are of the non-swelling type with low adsorption. Smectites, on the other hand, with their low surface charge undergo easy dissociation which in turn offers gel-forming properties and surface reactivity to them. These properties have turned 2D clay materials to good choice as additives/ composite material.. The composite of polymer – 2D clay composite imparts enhanced functionality like better mechanical strength, thermal stability, chemical stability, degradation, biocompatibility, good cellular interactions, better tissue regeneration, vascularisation and response to stimuli. 2D clays as an additive to polymer results in enhanced reinforcement, improved physic-chemical properties, and

better functionality. Noticeably, 2D clay-polymer composites loaded with bioactive moieties are currently a trending area of research and are utilized in 3D printing and hydrogel applications [Murugesan *et al.,* 2007]. The anti-microbial activity of 2D clays also makes them ideal for wound repair applications. The possibility for modification of 2D clays further expands their activity and applicability [Saikia *et al*., 2020].

REVIEW OF LITERATURE

2. Review of literature

2.12D clays and their importance

Clay materials have been used for traditional medicinal purposes for time-unknown. Recently, 2D clay materials are subjected to exploration for their incredible properties, such as a high surface area to volume ratio, ion-intercalation, exchange capacity, high adsorption capacity, and biocompatibility. 2D clays are thermally and chemically stable and exist in a wide variety of chemical compositions. The interesting surface chemistry of 2D clay is responsible for its wide choice of applications. The surface charge of 2D clays along with the possibility of ion intercalation add to its demand. 2D clay layers are either neutral, anionic or cationic that prefer conjugation/ intercalation of counter-ions to balance the charge and stabilize individual layers. The surface charge and overall surface chemistry of 2D clay materials with a high planar sheet-like structure are advantageous for a handful of applications like catalysis, absorbents, polymer additives, delivery vectors and tissue engineering. The large surface area and charge density promote the conjugation of counter-charged ions/ molecules that could be feasibly used for drug delivery applications [Zhang *et al.,* 2017].

2D clays like silicate clays, can be prepared by exfoliation from natural sources and other 2D clay namely LDHs can be synthesized by using co-precipitation, ion-exchange, sol-gel, hydrothermal or reconstruction methods. The easy synthesis protocols, a wide choice of chemical compositions, the possibility for intercalation of ions/ molecules of interest make 2D clays an economically feasible choice for various applications. The ion-interchangeable property of 2D clay further expands the variability of chemical composition and also facilitates the incorporation of targeted active molecules. 2D clays like LDHs also possess some peculiar properties in

addition. LDHs change to mixed metal oxides at 500^0 C and then revert to its original structure in the presence of water. This peculiar phenomenon of LDHs is called the memory effect and enables the addition of desired anions as per the applicational demands of the application [Mascolo *et al.,* 2015].

The 2D clay nanoparticles when used as an additive, increase the mechanical strength of polymer and provide better rheological properties. Hence 2D clay-polymer composites find many applications not limited to but including tissue engineering [Kurapati *et al*., 2016]. The high drug/biomolecule loading capacity of 2D clay on account of the surface charge, interlayer space and ion-intercalation capability further opens up the opportunity to apply 2D clay for bioactive molecules-loaded scaffolds. Peptide/ growth factor loaded scaffolds can in turn improve the bio-functional performance of the scaffold at the defect site facilitating better and more efficient treatment. The high ion adsorption/ exchange capacity of 2D clays contributes to environmental remedies, especially in wastewater treatment and heavy metal removal from industrial effluents [Fu *et al*., 2018]. 2D clays are biocompatible and undergo degradation to form non-toxic by-products that assure their feasibility as a biomaterial.

From the research findings and exploration into these materials, 2D clay nanosheets are emerging as a potential material for a wide spectrum of fields dominating both pure material science as well as medicine [Padil *et al* 2022, Gaharwar *et al.,* 2019]. 2D nanosheets have marked their space in various chemical applications and have been now explored for regenerative medicinal usage. 2D clay materials have been discussed and focused on as an important alternative biomaterial with tuneable functionality and biocompatible profile.

2.2 Types of 2D clays

2D clays are composed of mixed metal ion crystals of fine particle size. The 2D clay materials can be broadly classified as neutral, anionic and cationic clays depending on

the charge of layers and that of counter ions present at the inter-layer space that balances the net charge (Figure 2.1). The anionic clay includes LDHs which have positively charged layers balanced by water molecules and anions present at the inter-layer spaces. In LDHs, the planar layers compromise metal ions in a divalent oxidation state partially substituted with trivalent (+3) metal ions. The partial substitution with +3 oxidation state is responsive for the net positive charge of the 2D sheets. Cationic clays include silicate clays and have negatively charged sheets of metal ions and cations occupying the space between layers.

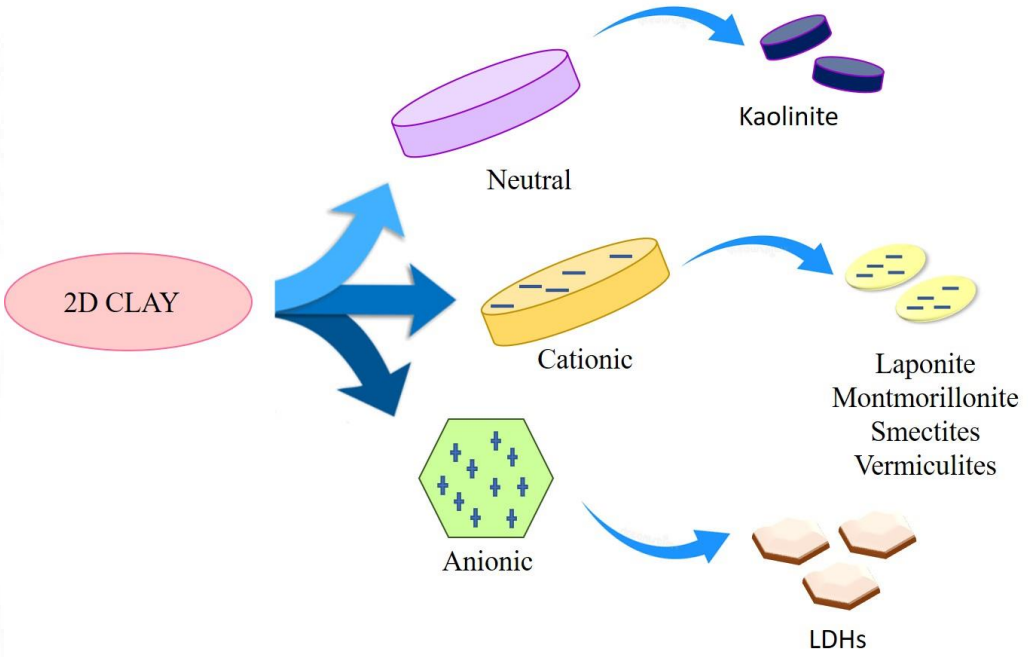

Figure 2.1: Types of 2D clays

2.2.1 LDHs

LDHs has got a brucite-like structure and has got structure comparable to hydrotalcite mineral which is a natural magnesium–aluminium hydroxyl carbonate ($Mg_6Al_2(OH)_{16}CO_3{\cdot}4H_2O$) [Gaines *et al.,* 1997]. LDHs is structurally $[M^{II}_{1-x}M^{III}_{x}(OH)_2]^{x+}[A^{n-}_{x/n}\cdot yH_2O]^{x-}$ with cations in +2 and +3 oxidation states and A represents

anions. The ratio of M(II) and M(III) varies from 2:1, 3:1 and 4:1 and a varied variety of anions, including inorganic moities, organic molecules, organic complexes, biomolecules and surfactants, can be intercalated in between the positively charged layers to balance the structure. The LDHs sheets consist of edge-sharing octahedral units with metal ions connected to six hydroxyl groups. The LDHs layers are stacked together due to their high charge density and can be exfoliated by different techniques and chemical modifications. LDHs can be synthesized in a wide variety of chemical composition since the synthesis protocol make it possible to have a different combination of M(II) and M(III) ions and anions. Mg/Al, Zn/Al and Zn/Fe are the most commonly explored LDHs. The basal spacing of LDHs is determined by the type of anions present, size and charge of the layers. The M (II)/M(III) ratio determines the charge density of layers and is responsive to the amount of anions that can be loaded onto the LDHs structure [Mishra *et al.,* 2018].

2.2.2 Silicate clays

Silicate clays are abundantly found in nature. Layered 2D silicates clays compromises of silicate tetrahedrons along with the presence of other elements like Al^{3+}, Fe^{2+}, Mg^{2+}, Ca^{2+}, Na^{2+}, and $K^{+\cdot}$ 2D silicate clays usually exist in a particle size range of 10-100 nm and thickness of 1 nm. The fundamental units of silicate clays are octahedron and tetrahedron units. In an octahedron, the metal cation is connected to six O^{2-} and/or OH^- groups forming a sheet structure. If the metal cation is divalent, then it results in a brucite-like structure while if the metal cation present in the octahedron unit is trivalent, then gibbsite-like sheets are formed. In the tetrahedron unit, the metal cation Si^{4+} in most cases is coordinated to four O^{2-} anions. The tetrahedron units form a 2D hexagonal mesh by sharing the corner oxygen atoms. Among the four Si^{4+}-O^{2-} bonds, three are shared between tetrahedrons while the other remains perpendicular to tetrahedral sheets [Mosavi *et al.,* 2018]. Silicate clays are again divided into further groups based on the arrangements of tetrahedral and octahedral sheets. Silicate clays are subgrouped as 1:1 and 2:1 type clays depending on the arrangement of octahedral

and tetrahedral sheets. 1:1 type of 2D clays represent clays in which a single octahedral sheet is linked to single tetrahedral sheet. In 2:1 type of clay materials, a single octahedral sheet is sandwiched in between two tetrahedral sheets [Mosavi *et al.,* 2018]. According to the arrangements of octahedral and tetrahedral sheets, 2D silicate clays are classified as below.

2.2.2.1 The 1:1 type clays

1:1 type clay materials have a half unit formulae of $M_xSi_2O_5(OH)_4$. Kaolinite, halloysite and serpentine are the major 1:1 type of clay minerals. In Kaolinite and halloysite, the central metal atom is divalent and in case of serpentine, the central atom is trivalent. These type of clay materials are electrically neutral and possess charge only at the edges [Wan *et al.,* 2022].

2.2.2.1.1 Kaolinite clay

Kaolinite clay is a major 1:1 type clay with silica tetrahedrons and alumina octahedrons. The structural formulae of kaolinite group is $Al_2Si_2O_5(OH)_4$. They are neutral 2D clays. The SiO_2, Al_2O_3, H_2O groups are predominantly found, at the same time elements like Mg, Fe, K, Ti *etc*., are found in trace amounts. Kaolin is also termed china clay and finds usage in catalyst, filler additive, adsorbent and adhesives [Aswathy *et al.,* 2017]. Hydrogen bonding, Van der Waals interactions and dipole-dipole interactions are responsible for upholding the layers. Kaolinite clay does not undergo swelling and therefore some of its application potential is limited.

2.2.2.1.2 Halloysite clay

Halloysite clay materials are 1:1 type of clay materials. The halloysite clay rolls up when hydrated and forms nanotubes and finds applications as drug delivery vectors [Yuan *et al.,* 2015]. They possess high surface area compared to other 1:1 type clay materials and therefore have been explored on various application grounds.

2.2.2.2 The 2:1 type of silicate clays

In 2:1 type, the half unit is $M_xSi_4O_{10}(OH)_2$. The important members of this family are smectite, illite and vermiculite. The smectite group further includes MMT and laponite.

2.2.2.2.1 Smectite clays

Smectite clays are among the most explored 2D clays. Smectite clays are structurally similar to talc or pyrophyllite. The smectite group consists of two main clay minerals: dioctahedral montmorillonite (MMT; $Na_m(Al^{2-}{}_mMg_m)Si_4O_{10}(OH)_2.nH_2O$) and trioctahedral Laponite ($Na_h(Mg^{3-}{}_hLi_h)Si_4O_{10}(OH)_2.nH_2O$) [Van olphen *et al.,*1979].. They have relatively low surface charges. Smectites are chemically very different compared to kaolinite clays. In smectite clays, Mg and Fe in octahedral sheets are

replaced by aluminum.

Vermiculite clays have a higher layer charge than smectites, which restricts water accessibility in the interlayer region. As a result, vermiculites are crystalline and therefore do not swell which is the usual characteristic of 2D clay. Interestingly, vermiculites have a high surface area. With increasing surface charge, the swelling tendency decreases for clays. The same trend is observed with illites with a high overall charge [Van olphen *et al.,*1979].

2.2.2.2.2 Laponite

Laponite clays exist in a diameter range of 25-30 nm and a thickness of 1 nm thickness. They possess a specific surface area of about 800 m^2/g and a cation exchange capacity of about 80 - 150 meq/100g. Laponite clays are negatively charged at the surface and edges are positively charged. These clays have got heavy metal content. The magnesium oxide forms octahedral sheets and silica forms tetrahedral sheets. The octahedral sheets of magnesium oxide are sandwiched between silica sheets.

$Na^{+}_{0.7}[(Si_8Mg_{5.5}Li_{0.3})O_{20}(OH)_4]$ is the structural formulae of laponite. Laponites are synthesized from inorganic mineral salts and have a disk- shaped morphology [Gawarhar *et al.,* 2019].

2.2.2.2.3 Vermiculite Clay

Vermiculite clays are natural hydrate minerals and come under the 2:1 type of clays. The 2D lamellar structure of vermiculite clays involves tetrahedrons. For example, Si-O or Mg-O tetrahedron. They are capable of expanding up to 20 times the initial size on high-temperature treatments. This property aids high performance as adsorbents, catalysts and thermal storage devices. Vermiculite clays when added to polymers, improve the thermal/mechanical properties and make them better flame retardants. When vermiculite clays expanded at elevated temperatures were mixed with polymers, then they impart anti-bacterial properties, better biodegradation profile, and phase change consistency. Vermiculite clays play the role of additives well, and improve strength, and thermal insulation properties. Vermiculite clays are in a large scale explored for catalysis, wastewater treatments, flame retardant *etc.,* [Wan *et al .,* 2019].

2.2.2.2.4 Montmorillonite (MMT)

Montmorillonite (MMT) is a major celebrated 2D clay. MMT is 2D layered clays with chemical formulae $[(Na,Ca)_{0.33}(Al,Mg)_2Si_4O_{10}(OH)_2]\bullet nH_2O$. In MMT, two tetrahedral layers of silica sandwiches single octahedral sheet of alumina. MMT has got high surface area and exists in platelets of diameter 0.2-2 μm and thickness 1 nm. The net charge is slightly negative due to the oxide anions as well as the charge discrepancy of metal cations and therefore allows cations at interlayer space. FDA accepts MMT as a medicinal product additive. They are used as filler material for reinforcement and as additives for various demanded functionality. The high surface area, low cost, excellent mechanical characteristics, and thermal barrier properties make them highly sort after 2D clay. MMT is also enrooting its influence as a high-performer for bone

scaffolds. MMT is found to increase cellular interactions, cell proliferation and differentiation when opted as composite material for bone scaffolds. [Cui *et al.,* 2019].

2.3 Synthesis of 2D clays

Most of the silicate clays have a natural origin and undergo further modification/ intercalation for exfoliation as per demands. The charge density of the 2D clay layers and the opportunity for intercalation helps in modifications and fine-tuning of materialistic properties of 2D clays.

2.3.1 Exfoliation

2D clays are mostly stacked together because of their charge density and are exfoliated to separate the individual layers. A common exfoliation technique is by using surfactant or other bulk ions that can occupy the interlayer space and thereby increase the distance between individual layers. 2D silicate clays undergo modification by (1) intercalation of large molecules (2) exfoliation by thermal treatment (3) sonication to result in individual sheets of cationic clay. The low charge density of cationic clay also facilitates exfoliation. MMT and laponites are well exfoliated to form platelet sheets with uniform dispersion by sonication with beads [Kim *et al.,* 2020].

2.3.2 Synthesis of LDHs

LDHs are synthesized commonly by bottom-up approaches like co-precipitation, ion-exchange and reconstruction methods. Hydrothermal synthesis and sol-gel method are also other opted routes of LDHs preparation. The bottom-up way of approach is highly appreciable since it permits the feasibility of obtaining different chemical compositions of LDHs. LDHs of varying metal ion content can be prepared with a wide choice range of anions. The tuneable, easy and low-cost synthesis protocols are highlights of LDHs profile. LDHs are therefore finding space in diverse applications. The high charge density of LDHs makes the exfoliation of individual sheets a tedious

process. But still, it is possible to further exfoliate the stacked-together layers of synthesized LDHs by using solvent effects, sonication and chemical modifications [Mishra *et al.,* 2012].

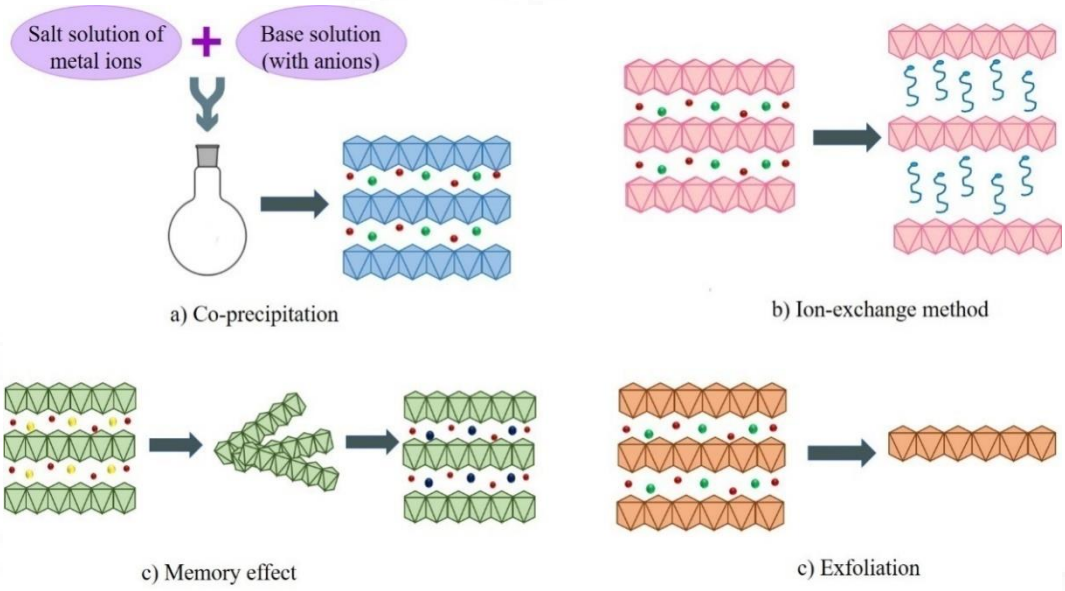

Figure 2.2: Synthesis routes of LDHs

2.3.2.1 Co-precipitation

By this method, anion solution is added to the solution containing a mixture of divalent and trivalent metal cations and then the pH is adjusted by the addition of base. This triggers the nucleation step by precipitation of LDHs particles. The precipitation results as an outcome of the condensation of hexa-aqua salts of metal ions. The precipitated product is a brucite structure with even distribution of M(II) ions partially substituted by M(III) ions. The usually preferred pH range is 8-12 and choice depends on the chemical composition and particle size needed. Co-precipitation involves three stages: (1) nucleation (precipitation) (2) aging (3) drying. The aging stage is achieved by thermal treatment of the reaction mixture and is done to achieve good crystallinity to the synthesized LDHs. The particle size can be fine-tuned by optimizing the pH,

nucleation time, nucleation temperature, aging time and aging temperature. [Evans *et al.,* 2006, Mohapatra *et al.,* 2012].

2.3.2.2 Anion- exchange method

This method is used for the selective intercalation of anions into the interlayer space of LDHs. The anion exchange method works by the principle that the anions present at LDHs initially synthesized by the co-precipitation method are replaced by anions of interest having better affinity. This method is therefore also termed as an indirect method. The synthesized LDHs is stirred in an inert atmosphere in a solution containing an excess of anions to be intercalated. This technique is commonly used for hybrid preparation in which the target molecules like biomolecules, drug moieties can be easily loaded into the LDHs structure without any destructive effects [Rives *et al.,* 2014].

2.3.2.3 Reconstruction method

The reconstruction method is based on a very peculiar property of LDHs known by the name - - memory effect. LDHs loses their structural integrity at high temperatures and become mixed metal oxides. Interestingly, LDHs treated to a temperature of 400^0-500^0 C turn to mixed metal oxide but revert to the original LDHs structure when hydrated in an anionic solution. This curiosity-generating property of LDHs is called the memory effect and is explored on grounds to achieve LDHs structures of interest. This method is used for the intercalation of organic moieties into the LDHs layers. For temperatures above the range of 400^0-500^0 C, the formation of stable spinel structure hinders the tracing back to the original structure when hydrated [Moscolo *et al.,* 2015].

2.3.2.4 Exfoliation of LDHs

Mostly LDHs are synthesized by the abovementioned three methods. But as per demand of certain applications that opt for single layer/ completely uniform dispersion of LDHs, then the top-down approach is preferred. The top-down technique of LDHs

preparation simply involves the exfoliation of LDHs bulk layers by applications of either sonication or bulky anion solution or by using different solvents. The highly charged layers of LDHs make it more difficult to exfoliate individual layers compared to other 2D clays like kaolin, MMT or laponite. The exfoliation of LDHs sheets is achieved by amending the interlayer space chemistry (anion affinity) and by using the proper choice of solvents, usually highly polar solvents are preferred [Wang Q *et al.,* 2012]. e Exfoliated LDHs sheets finds remarkable usage as high-performance catalyst, thin film [Li *et al*., 2005], solar cells [Gunjakar*et al.,* 2011], lithium batteries [Lee *et al.,* 2011] *etc*.,

2.4 Structure and characterization

The structure of 2D clays primarily encloses tetrahedral and octahedral sheets as the basic fundamental unit. In case of the anionic clay, LDHs has got edge-sharing octahedral unit alone. On the other hand, silicate clays consist of tetrahedral and octahedral sheets orientated in either 1:1 or 1:2 ratios.

In case of kaolin clays, which are 1:1 type of clays, the silicon atoms in tetrahedral layers are connected to four oxygen atoms while the aluminium atoms in octahedral sheets are connected to eight oxygen atoms. The ratio of tetrahedral: octahedral sheets of kaolin clays remain as 1:1. In kaolinite, the tetrahedral and octahedral sheets are fused and the oxygen atoms are shared. The structure of kaolin clays is highly stable and shows low expansion coefficient [Miranda-Trevino JC *et al.,* 2003]. The layers are held together by strong H-bonding which is responsible for the overall stability of the structure. The chief component of kaolin clays is kaolinite which is chemically $Al_2Si_2O_5(OH)_4$ with 46.3% silica, 39.8% alumina and 13.9% water [Varga G *et al*., 2007]. Kaolinite morphologically consists of plate-like configuration of pseudohexagons with triclinic crystal structure. The hexagonal structure has got a diameter range of 0.2–10 μm and 0.7 nm thickness along with a density of 2.6 g/cm^3.

The lattice parameters are reported to be are a = 0.515 nm, b = 0.895 nm, c = 0.740 nm, α = 91.68°, β = 104.87°, γ = 89.9° with P1 group symmetry [Varga G *et al.,* 2007].

In contrast to kaolin clays, 2:1 type clays have two silica tetrahedrons fused to one alumina octahedron and oxygen atoms are shared between the tetrahedral and octahedral sheets. The layer thickness of 2:1 type clays is found to be of 1 nm while the lateral dimensions are high and comes usually in the macro range. The aspect ratio is usually high in case of these clays. The 2:1 type clays with silicon tetrahedrons and alumina octahedrons without any other substitutions are called pyrophyllite. Pyrophyllite do not expand in water and has only an external surface area. If the silicon in tetrahedron is substituted with aluminium atom, then it results in mica clays. The substitution imparts partial negative charge balanced by potassium cations at the inter-layer space. Remarkably, the potassium ions size coincides with the hexagonal hole size created by the Si/Al tetrahedral layer and therefore is held very tightly between the layers. Mica clays are held by strong electrostatic interactions between the negatively charged sheets and cations. Mica similar to pyrophyllite does not swell in water nor do have any external surface area. But if the aluminium atom in octahedron is substituted with magnesium ions, it results in the formation of montmorillionite clay, an important member of smectite clays [Pavlidou, S *et al.,* 2008]. The resulting negative charge is balanced by the calcium and sodium ions present in the interlayer space. The interlayer cations remain hydrated and does not fit into the hole size of tetrahedrons. Therefore, the MMT clays are held together by weak forces and water molecules, therefore possess the possibility for expansion.

MMT is layered silicate clay having silica tetrahedral sheets sandwiching octahedrons containing aluminium atoms. The thickness of the 2D montmorillonite clays comes in the range of nm, while the lateral dimension falls in the micrometer range. The isomorphic substitution causes a net negative charge to the layers. The so-developed negative charge is counterbalanced by the cations at the inter-layer space. The cations present at the interlayer space for example, magnesium, sodium and calcium can be

exchanged with positively charged molecules with higher affinity. The incorporation of cationic moieties with higher sizes increases the inter-lamellar distance [Chin I-J *et al.,* 2001]. The high aspect ratio together with the possibility for intercalation makes these clay excellent reinforcement material in polymer composites. Halloysite clays are meanwhile tube-shaped in contrast to other natural clays and have an aspect ratio of 19. The length of the halloysite tube remains to be about 0.2 to 1.5 μm while the inner and outer diameter turns out to be around 15 nm and 50 nm respectively.

Laponite clays consist of silicon ions containing tetrahedrons sandwiching magnesium and lithium ions containing octahedrons. Laponite is composed of 62.34% oxygen, 20.78% silicon, 14.29% magnesium, 1.81% sodium and 0.78% lithium. The individual sheets are stabilized by ionic bonding and van der Waals forces. Laponite clays have a disc-shaped morphological structure with a negative charge which is balanced by inter-layer cations usually sodium ions. Interestingly, laponites self-assemble to form an interconnected network in a so-called house of cards structure. They are synthetic clays coming under smectite clays. They hold structural similarities to hectorite. It contains hydrated magnesium silicate with octahedral magnesium oxide sandwiched between two parallel layers of tetrahedral silica layered in 2:1 ratio. Laponite hydrates and swells when exposed to water. When hydrated laponites release sodium ions present at the interlayer space, causing a negative charge formation at the faces. Meanwhile, the protonation of OH group causes a positive charge. Laponite forms a colloidal dispersion in water with negatively charged faces and positively charged rims [Ruzika *et al.,* 2011].

Anionic clays, namely LDHs are structurally different from silicate clays discussed till now. LDHs has a brucite structure with layers of divalent cations evenly substituted with trivalent anions. The major divalent cations are Mg^{2+}, Zn^{2+}, Ca^{2+} and Ni^{2+} while mostly opted trivalent cations are Al^{3+}, Fe^{3+}, and Cr^{3+}. LDHs consists of an octahedral structure with the metal ions occupying the central position and edges being shared with the adjacent octahedrons forming an edge-sharing octahedral network. Each

cation in the octahedral unit is connected to six OH^- ions that are directed to the corner. The partial substitution of trivalent cations imparts a positive charge to the layers, which are balanced by the counter-anions and water molecules present at the inter-layer space. The columbic force of attraction between the negative and positive counterparts of LDHs, along with the hydrogen bonding among the OH groups of layers and electronegative atoms in the anions are responsible for the overall stability of the LDHs lattice structure [Mishra *et al.,* 2018]. A wide range of anions including inorganic anions, biomolecules, surfactants, anionic complexes, organic moieties can be intercalated into the inter-layer space. LDHs platelets exist as hexagonal plates stacked one over the other due to high charge density. The anions in the inter-layer space may be arranged in diverse ways. The compositional chemistry and ordering at the interlayer space determine the thickness of the interlayer space. Intercalation with large anions like organic molecules results in the widening of interlayer space and results in a stable frame called pillared layered structure [Britvin *et al.,* 2008].

The physico-chemical features of 2D clays hold vital control over the displayed properties of 2D clays. Henceforth, characterizations of 2D clays are done with the help of a range of techniques to affirm its structural and other typical features. X-ray diffraction (XRD) is one of the key characterization techniques opted for conforming the structure of 2D clays. Interestingly, the crystal structure of 2D clays can be inferred from the diffraction pattern obtained from XRD analysis. Also, the lack of impurity peaks in XRD spectra is considered a detector criterion for impurity check.LDHs are reported to show (00l) indices at lower diffraction angles and (110) peak at the higher diffraction angle values [Tonelli *et al*., 2021]. XRD patterns of LDHs direct toward hydrotalcite-like structure [Kim *et al*., 2018]. The size and morphology are two major physico-chemical features of 2D clays that are usually characterized by using transmission electron microscopy (TEM). The size and shape of LDHs structure tend to vary depending on the synthetic conditions. The TEM images of LDHs with different ranges of particle size and size distribution are reported, varying from as low

as 50 nm to even more than 500 nm [Kim *et al*., 2018, Deng *et al*., 2020]. The typical morphology exhibited by LDHs is hexagonal and is well distinguishable in TEM imaging [Deng *et al*., 2020]. FT-IR and Raman spectroscopy provides information on the bonding in 2D clay structure, identifying functional groups and intercalated anions in LDHs structure. FT-IR spectra of MMT usually show vibrational bands notably of OH, Si-O-Si, Al-O-Al, Si-O and Al-O groups [Boudiemaa *et al*., 2014]. The Raman and IR analysis of LDHs structure show hydroxyl group, metal-O bond and also vibrational peak confirming the type of anion intercalated in between the layers [Benício *et al*., 2015].

The thermal performance of 2D clays is notably identified using thermogravimetric analysis. The degradation profiling of LDHs involves the initial removal of absorbed water, followed by intercalated water, then dehydroxylation and later elimination of intercalated anions. Heating LDHs beyond 500^0 C converts them into mixed metal oxide. In the case of MMT, there are two major losses on thermal treatment observed. Initially, between 100^0 C to 350^0 C, a significant weight loss is observed because of the elimination of absorbed and intercalated water. Heating of MMT between 500^0 C to 800^0 C leads to dehydroxylation [Boudjemaa *et al.,* 2014]. The charge of the clay material is another important feature overlooked mainly because of its impact on the applicability of the material. The loading and uptake of nanomaterials are also affected by the net surface charge. Therefore, charge holds a critical influence on the applicability, especially for biomedical applications. 2D silicate clays like laponite and MMT show a net negative surface charge [Xie *et al .,* 2019], with a positive charge at the edges and a net negative charge at the face [Gaharwar *et al.,* 2019]. The hydrodynamic size of the clay material is estimated with the help of dynamic light scattering (DLS) [Kaur *et al.,* 2021].

2.5General and biomedical application

Clay materials have been spotted as traditional remedies over a very long time for medical, anti-oxidant, anti-inflammatory, blood purification *etc.,* [Gorchakov *et al*., 2001, Mousavi *et al*., 2018]. Research updates point out that 2D clay materials have also marked their impact on various medical and non-medical fields [Gaharwar *et al.,* 2019]. The physico-chemical properties and their tuneable nature make 2D clay materials an excellent choice for many applications. Over the years, 2D clay materials have marked their momentous pertinency in tissue engineering, absorbent, catalyst, hybrid materials, drug delivery vector, environmental adsorbent, additives, flame retardant, anti-bacterial agent, bioimaging, biosensor *etc*., [Kuang *et al*., 2010].

The layered structure, high surface area, more active sites, uniform distribution of metal cations and ion-exchange capacity of LDHs have helped them to contribute positively as catalysts. Interestingly, 2D LDHs are finding purpose as electrocatalysts, photocatalysts, solid base catalysts, intercalated catalysts and supported catalysts. The LDHs also serve as nanocatalysts in the form of nanosheets and as composite forms [Fan *et al.,* 2014]. LDHs exhibit appreciable performance and stability over repeated cycles. LDHs can be fabricated with a long range of transition metals like manganese, nickel, iron, cobalt, copper *etc.,* [Morikawa *et al.,* 2014] and are reported to serve as excellent photocatalysts and electrocatalysts [Tian *et al.,* 2016]. Ni-based LDHs showed good catalytic activity for oxygen evolution reaction. Most notably, it was also inferred from the results that the LDHs showed enhanced catalytic activity on exfoliation [Song *et al.,* 2014].

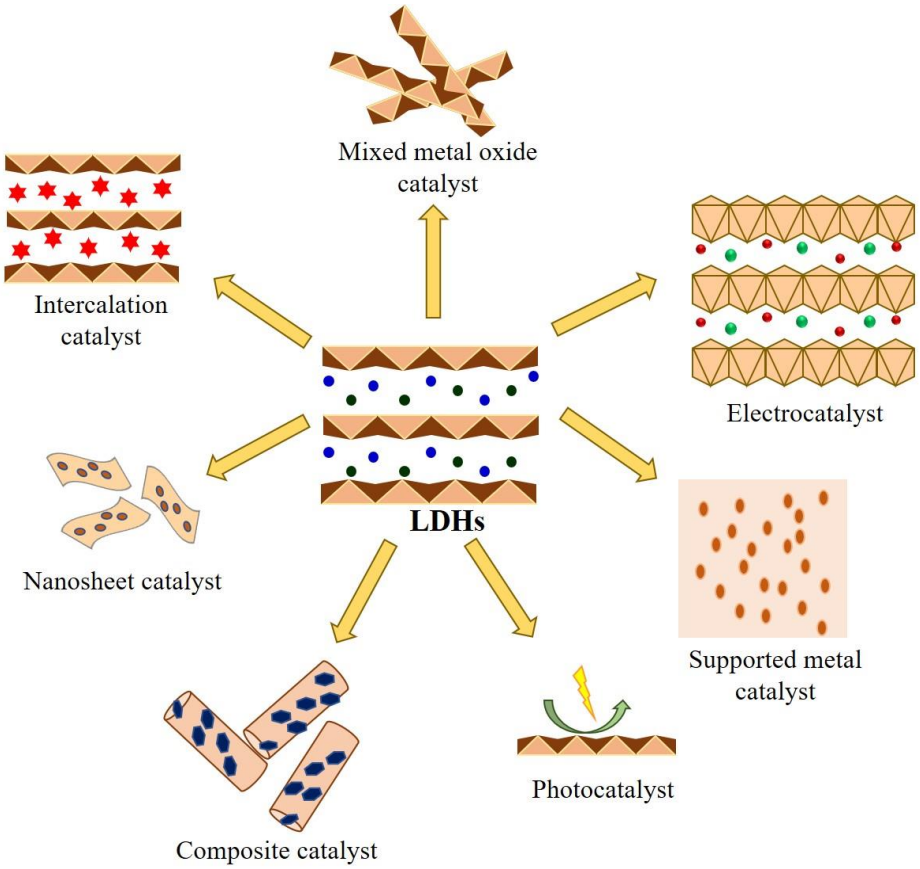

Figure 2.3: LDHs as a catalyst in diverse forms

Another important application of 2D clays is as an adsorbent. More number of active sites over the broader surface area turn out advantageous for 2D clays as adsorbents. Hence 2D clays serve as low on cost, and high on performance in environmental applications. They are being explored for heavy metal ion removal and wastewater treatments [Fu *et al*., 2018]. Indeed, kaolinite clay was reported to show good adsorption of ions like cadmium, lead, copper and zinc in single element as well multi elemental system [Srivastava *et al*., 2005]. MMT nanosheets are reported to exhibit high adsorbent properties. For instance, the charge and the OH groups of MMT facilitate hydrogel formation and MMT-based hydrogels are widely researched for adsorbent applications [Kim *et al.,* 2020]. Incase of LDHs, the memory effect and ion-

exchange capacity work in favour of the role as an excellent adsorbent. Many reports narrate the performance of LDHs nanosheets as well as their hybrid forms to perform well in heavy metal and organic dye adsorption. Therefore, LDHs nanosheets are been suggested as a reliable cost-effective option for wastewater treatments [Zubair *et al.,* 2017].

One of the dominant applications of 2D clay is as delivery vectors. The surface charge, surface area, pH sensitivity are strong points for its vector performance. For example, laponite, positively charged 2D clay nanomaterials facilitate high loading of negatively charged drug molecules. More interestingly, the laponite nanodisks exhibited pH-sensitive drug release at acidic pH which is profitable for cancer therapy. The study also cited that the 2D nanoclay enabled multi-drug loading [Zheng L *et al.,* 2019]. Considering LDHs, room for ion-intercalation, surface loading, ion-exchange potential, and compatibility with biosystems ease their vector function. Also, the positive charge of LDHs helps enhanced cellular uptake and pH-dependent release of loaded cargo and forte for lysosomal escape turns beneficiary to delivery applications [Manisekaran *et al.,* 2021]. Apart from mere drug loading, LDHs roll out to be a marvellous delivery vector capable of loading a wide range of moieties which includes other therapeutic constituents like genes, peptides, growth factors, nucleic acids *etc.*, [Ladewig *et al.,* 2009].

Yet another important application of 2D clay materials is in the field of tissue engineering. 2D nanoclays exhibit are taken to be a strong potential alternative for conventional tissue engineering scaffold materials, especially in bone regeneration applications [Kurapati *et al*., 2016]. 2D clays also show an appreciable mechanical strength, fine-tuning capacity in case of chemical composition, loading flair for growth factor/ anti-inflammatory molecules *etc.,* [Chimene *et al.,* 2015]. Also, they show a compatible profile with non-toxic degradation products. Different 2D clays have been quoted to be helping in better cell adhesion, proliferation and differentiation facilitating osteogenesis [Wu *et al*., 2021]. It is inferred that the presence of bioactive

elements like magnesium, calcium or silicon in 2D silicate clays would be held responsive for alkaline phosphatase activity, regulation of osteogenesis influencing enzyme, calcium deposition or extracellular matrix formation [Paul *et al*., 2014]. LDHs having hydrotalcite-like lamellar structures are esteemed to be a good alternative to bioceramics in bone scaffolds. The ease of fabricating into composites, hybrids or hydrogels, mechanical strength, biocompatibility, option for osteogenesis triggering molecules loading ability forte LDHs as a reliable candidate for tissue engineering [Izbudak *et al*., 2021]. The anti-bacterial property of LDHs also makes them cut above the other traditional substitutes that trigger unwanted inflammatory responses [Peng *et al*., 2018, Cunha *et al*., 2016]. LDHs are cited to improve the mechanical strength of polymer-based scaffolds and most importantly, enhance the proliferation of stem cells, positively influence the regulation of genes responsible for osteogenesis and aid in differentiation [Enderami *et al.,* 2022].

Another domain of 2D clays is their anti-bacterial activity. For instance, 2D MMT clays are specified to generate hydroxyl radicals on light exposure causing bacterial ablation [Pan *et al*., 2021]. Different elemental combinations of LDHs were reported to show varying anti-bacterial properties against E. coli and S. Aureus [Li *et al*., 2020]. Furthermore, silver-deposited LDHs coating was specified to show an enhanced range of anti-microbial activity covering both gram-negative and gram-positive ranges. To add on, the abovementioned coating also showed a success rate of over 99 % against tested microbe systems [Chem *et al.,* 2012].

2D clays are also explored intensively for biosensor applications. The surface charge on 2D clays indeed eases the immobilization of biomolecules onto the surface for biosensor fabrications. The phenol sensing potential of laponite and LDHs-based biosensors was studied by immobilizing polyphenol oxidase. Interestingly, LDHs-based sensors showed an outstanding sensing limit of (≤1 nM) [Shan *et al*., 2003]. The ease of fabrication of 2D clays/ LDHs helps accomplish functionalized LDHs ideal for imaging and recently many research groups have been focussing on the usage of LDHs

in the bioimaging field [Jin *et al*., 2019]. Indeed, there are reports on fabricating LDHs so as make them multifunctional for synergic therapy. There are many reports on fine-tuning and engineering LDHs for targeted imaging with simultaneous drug loading for tumour-specific release. The results from the theranostic research using LDHs are quite promising for more efficient synergic therapy [Andrade *et al.,* 2019].

2.6 Safety issues of 2D clays/ LDHs

Not many in-depth references on toxicity studies of 2D clays are available currently. In a comparative study between two -different types of 2D clays (laponite and MMT), MMT exhibited higher cytotoxicity in human embryonic kidney cells and cervical cancer cells [Rawat *et al*., 2014]. The available reports show varying inferences dependent on the dose, test systems, elemental metal ion type of LDHs, exposure time *etc.,* [Choi *et al*., 2011]. The physicochemical features of LDHs influence the compatibility response with biological systems. The impact of particle size on LDHs-induced toxicity was tested in both cancerous cells and mouse models. The results pointed out that Mg-Al LDHs showed a size-dependent toxic response with smaller particles inducing a more toxic response than higher particle size (Figure 2.4).

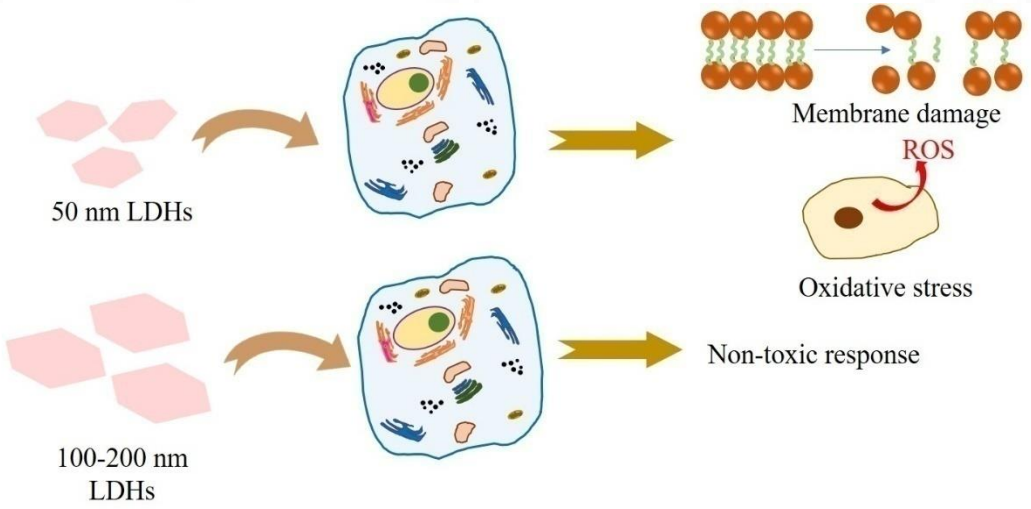

Figure 2.4: Size-dependent interaction of LDHs with *in-vitro* systems

The cell membrane rupture was higher in 50 nm LDHs exposed cells rather than 100-200 nm ones. However, for the *in-vivo* systems, no evident toxic response was evident in the test groups exposed to each of the LDHs types [Choi *et al.,* 2008].

In another study, MMT was reported to cause oxidative stress and membrane breakage at concentrations higher than 500 µg for time periods of 48 h / 72 h and no evident effect for 24 h exposure. *In-vivo* model however, no remarkable toxicity was observed for MMT exposure [Baek *et al.,* 2014]. The repeated exposure of LDHs of six times caused accumulation over the lungs and an inflammatory response leading to mortality. During the study, Mg-Al LDHs on intraperitoneal administration in mice showed a severe toxic response even for a low dose of 30mg/kg. Interestingly, the lipid functionalization of LDHs caused amelioration of the toxicity of LDHs and showed variation in biodistribution from the lungs to the liver [Yan *et al.,* 2017]. In another study, Mg-Al LDHs in their bare form was found to induce a negligible reduction in cell proliferation and the fabricated LDHs were used further as a delivery vector for cancer treatment [Chakraborty *et al.,* 2013].

The literature on LDHs toxicity has been concentrated mostly on Mg-Al LDHs as test substances and there are very few available on other types of LDHs like Zn-Al or Mn-Al LDHs in comparison to the former. Since elemental composition influences toxicity, it is also important to overlook other types of LDHs as well to have a more comprehensive outlook. Overall, reports on the compatibility of LDHs require more enhanced evaluation particularly since the material holds promising medicinal sco

MATERIALS AND METHODS

3. Materials and methods

3.1 Chemicals

Aluminium nitrate nonahydrate, Zinc nitrate hexahydrate, sodium hydroxide and sodium carbonate required for the LDHs synthesis were purchased from Sigma Aldrich, USA. For cell culture, maintenance and *in-vitro* assays, Dulbecco's Modified Eagles Medium (DMEM), Modified Eagles Medium (MEM), Fetal bovine serum (FBS), trypsin-EDTA, antibiotic and antimycotic (Ab/Am) solution wereprocured from Gibco, Grand Island, NY, USA. Similarly, 3-(4,5- Dimethylthiazol-2-yl)-2,5-diphenyltetrazolium bromide (MTT), Neutral red, trypan blue, dimethyl Sulphoxide (DMSO), Griess reagent were purchased from Sigma Chemicals Co. Ltd. (St. Louis, MO, USA). Acridine orange, ethidium bromide, 4',6-diamidino-2-phenylindole (DAPI), propidium iodide (PI) were from Himedia, India. Rhodamine phalloidin for cytoskeleton staining was from cytoskeleton Inc. Coomassie brilliant blue stain was obtained from Merck, India. For the DCFH-DA assay, the dye was purchased from Molecular probes, Invitrogen, CA, USA. Fluorescent dyes for staining like Calcium AM and JC1 were purchased from Thermofisher Scientific, USA. DNA ladder kit was from Gen elute mammalian genomic DNA miniprep kit, Sigma was used for the DNA laddering assay. For the *in-vivo* study, histopaque, L-glutathione (GSH), sodium dodecyl sulphate (SDS), thiobarbituric acid and tris base were purchased from Sigma, USA. Hematology study was carried out using reagents from Horiba, Japan. Reagents for urine and blood analysis were from Erbamannhiem, Germany. Folin's reagent was obtained from Merck, US. Tritiated thymidine for immunotoxicity study was purchased from American radiolabelled chemicals Inc. For histopathology, Eosin and Hematoxylin were procured from Himedia, India.

3.2 Equipments

Synthesis was done with the help of hot plate (IKA RCT basic), Hot-air oven (Heraeus Hot air oven) and centrifuge (Eppendorf centrifuge 5810 R). TEM was done using JEOL JEM 2100 TEM, China. XRD analysis was done with the help of Bruker D8 advanced PXRD. IR Tracer 100, Shimadzu was used for the FT-IR analysis. The Raman spectra were taken in the Confocal Raman microscope, Alpha 300A, witec Inc, Germany. TGA analysis and DTA spectra were obtained from SDT Q 600 V8.3 Built-101, TA Instruments, USA. For. DLS and Zeta potential data were attained from Malvern zetasizer nano ZS, UK. For the *in-vitro* study, Mark Air particulars Laminar air flow (India), fluorescence microscope from Axio Scope A1 Carl Zeiss, Germany), Nikon Phase Contrast Microscope, New Brunswick Scientific Incubator shaker (USA), Sanyo CO2 incubator (Japan), UV 1601, Shimadzu UV Visible Spectrophotometer (Japan), PerkinElmer Lamda 25 UV Visible Spectrophotometer, (Singapore), BD FACS Flow cytometer, Aria III, Biosciences, US were opted. For *in-vivo* study, Horiba Vet ABC hematology analyzer (Japan), Polytron P 3100 tissue homogenizer (Switzerland), Erba Mannheim XL300 biochemistry analyser (Germany) and Leica RM 2125 RT Microtome, Germany were used.

3.3 Animal handling

After animal ethics committee approval, Wistar rats weighing about 200-250g needed for the study were obtained from the Division of laboratory animal sciences, BMT wing, Sree Chitra Tirunal Institute for Medical Sciences and Technology, Trivandrum. The Wistar rats were maintained at the light-dark cycle of duration 12 h. The temperature and humidity were upheld at 22 ± 2°C and 30-70% humidity. The animals were fed with standard pellets and water *ad libitum*. All twelve rats were acclimatized 5 days before starting the experiment. For identification purposes, Wistar rats were marked using picric acid. Apart from that, proper labeling on the cages with the date of experiments, experiment name, experimental start date, animal numbers, group

number and end of experiment date was specified. The animals were observed visually daily throughout the experiment. Efforts were taken to ensure the safe handling of the experimental animals with a humane approach, avoiding chances of pain and distress for the experimental animals. The welfare of the animals was committed to par with the regulatory guidelines of the committee for the Purpose of Control and Supervision of Experiments on animals (CPCSEA).

3.4 Animal ethics

The *in-vivo* study was done after obtaining approval from the Institute Animal Ethics Committee (IAEC). The i*n-vivo* experiments were done in accordance to the approved guidelines of CPCSEA, Govt. of India. The IAEC approval number for the study was SCT/IAEC-379/NOVEMBER/2020/107.

3.5 Motivation for the study

Over the years, bone grafts show up to be a highly demanding clinical need. Natural bone possesses the ability for self-repair and regeneration. But in cases of fractures with above-critical size defects, a decrease in bone strength and regeneration capacity over old age demands external support for defect repair [Zhao *et al.,* 2021]. As per reports, worldwide per-year spending on bone fractures is around 5.5 million U.S dollars and the overall cost on 17 million U.S dollars [Ling *et al.,* 2018]. On average, two million bone implantations are done across the globe over a year [Campana *et al.,* 2014]. Autograft implants remain the typical option but availability and morbidity at the donor site remain major concerns. On the other end, unwanted immunological responses, chances of rejection and disease transmission have been a concern for the allografts/xenografts-based methods for bone implantation [Zhang *et al.,* 2019, Zhao *et al .,* 2021].

The shortcomings of conventional methods like autografts, allografts or xenografts have triggered research for a more advanced option. The possibility of tissue

engineering for developing bone substituents was explored in this context [Amini *et al.,* 2012]. Although yet to be translated to clinical applications, bone engineering is considered capable of settling issues of availability shortage and immune rejection associated with current clinical-run bone-implantation choices. Bone engineering aims at fabricating bone substituent materials that could mimic natural bone in its mechanical strength and bio-environment to facilitate bone repair and new bone formation [Tang *et al.,* 2021]. Apart from the mechanical strength, osteo-regeneration requires the availability of bioactive factors for new bone formation.

Among the various materials under cross-analysis for bone bio-engineering, materials capable of loading and releasing growth factors and proteins promoting cell proliferation, stem cell differentiation, osteogenesis, angiogenesis *etc.,* would be highly favorable [Parent *et al.,* 2017, Rather *et al.,* 2019]. Layered double hydroxides being anionic 2D clays with high loading capacity and sustained release serve this purpose [Peng *et al.,* 2018]. LDHs showed a loading capacity of 197 % for Alendronate, a drug used for osteoporosis treatment. Interestingly, the loaded LDHs exhibited 2.7 times increment in intergeneration at *in-vitro* level in comparison to the negative control group and 1.4 times increase compared to the autologous bone-implant sample [Wang *et al.,* 2020].

LDHs are considered a new-generation material for bone applications. Captivatingly, LDHs showed an elastic modulus comparable to corticol bone [Peng *et al.,* 2018]. Like hydroxyapatite, LDHs are reported to exhibit high osteointegration properties and hold potential bone-regeneration applications. LDHs is reported to influence pre-osteoblast metabolism and contribute to osteogenic differentiation [Kang *et al.,* 2018]. LDHs have been reported to be a reliable material for bone bio-engineering applications with high osteointegration properties. Though LDHs hold bright prospects in futuristic applications, only limited resources are available on their toxicity profile. It is of absolute necessity that any material with potential biomedical applications needs to be critically evaluated for its compatibility with bio-systems and gather a compact

understanding of the biological interaction of the material. Within this frame of reference, we designed the following work to understand the interactions of LDHs when exposed to *in-vitro* and *in-vivo* systems.

3.6 Hypothesis

2D Zn-Al Layered Double Hydroxides (LDHs) can be a less toxic potential material for biomedical applications.

3.7 Aim

To evaluate the biological interactions of 2D Zn-Al Layered Double Hydroxides (LDHs) in *in-vitro* and *in-vivo* systems

3.8 Objectives of the study

The aim of the work is to evaluate the biological interactions of 2D Zn-Al layered double hydroxides (LDHs) in *in-vitro* and *in-vivo* systems. Three objectives were designed to accomplish the aim as follows.

Objective I: *Synthesis and Physico-chemical characterization of 2D Zn-Al LDHs.*

Objective II: *Evaluation of cellular interactions of 2D Zn-Al layered double hydroxides in in-vitro system.*

Phase I: *Cellular interaction of 2D Zn-Al LDHs with L929 fibroblast cells.*

Phase II: *Cellular interaction of 2D Zn-Al LDHs with human osteoblast cell line (HOS cells).*

Objective III: *Toxicity evaluation of 2D Zn-Al layered double hydroxides in rat model.*

3.9 Rational behind selection of the material

Research groups over the globe have been evincing LDHs as a capable 2D material beyond graphene. These 2D structures with hydrotalcite structure, having metal ion pattern with even distribution, ion-exchange property, anion intercalation possibility and positive charge finds far- stretching application possibility in industrial as well as biomedical scenario and therefore has been cast as multi-functional material [Karan *et al.,* 2011]. The tunability in metal composition and physicochemical properties along with high loading capacity, charge, ion-exchange, enhanced cellular uptake, pH-sensitive response, has made LDHs a wonderful option for biomedical applications. Over the years, the different types of LDHs have shown promising results in different medical applications including drug delivery, gene vector, tissue engineering, PTT, PDT, cancer therapy, sensing, imaging and anti-bacterial activity [Hu *et al.,* 2022].

The high surface area, planar structure, intercalation capacity and high positive surface charge enable high loading of drugs, genes or any preferred anions. Therefore, LDHs have been extensively explored for biomedical delivery applications [Shirin *et al.,* 2021]. Negatively charged drugs/DNA/genes can be loaded onto positively charged LDHs by electrostatic interaction facilitating delivery purposes with the added advantage of tunability. Also being positively charged, LDHs are reported to attract negatively charged cornea enabling targeted drug delivery and enhancing drug availability at the target site [Cao *et al*., 2011]. The pH sensitivity of LDHs also enables its usage for cancer therapy by providing access to selective drug delivery to acidic pH environments. For example, Cu-Al LDHs have been reported as multi-functional material for cancer treatment with targeted drug delivery combined with anti-bacterial activity [Bangherzadeh *et al.,* 2022]. Another noteworthy property of LDHs is their memory effect which allows them to trace back to the actual lamellar structure on hydration after the mixed metal oxide structure adapted at calcination at 300-500^0 C.

The memory effect is also explored for many applications and mainly for vector and sensing applications [Wong *et al.,* 2004].

Among all these interesting applications, one that has attracted the most focus is the applicability of LDHs in tissue engineering. Literature reviews highlight the reliability of LDHs as bone implants. The tuneable chemical/ physical characteristics of LDHs, lamellar structure, ease of composite preparation, capacity to load drugs, anti-inflammatory molecules or growth factors have turned out to be merited for its usage in tissue engineering. As per reports, LDHs also aid in cell adhesion to the target site, proliferation at implant position and differentiation to facilitate osteogenesis [Rojas *et al.,* 2022]. Most importantly, the anti-bacterial activity of LDHs especially Zn-Al LDHs facilitated in overcoming the unwanted inflammatory response at the implant site which is one of the major concerns during implantation [Peng *et al.,* 2018].

LDHs are a new generation material for bone applications. Similar to hydroxyapatite, LDHs are reported to exhibit high osteointegration properties and hold potential bone-regeneration applications. Reports with combinations of hydroxyapatite and LDHs hold promising potential in futuristic bone implant applications [Donnadio *et al*., 2021]. Even with the promising results from LDHs-based research on tissue engineering and other medical applications, one of the shortcomings in the field remains the limitation in resources about the biocompatibility and toxicity concerns.

In this context, we selected Zn-Al LDHs as the test material to get an enhanced understanding of the toxicity profile with reference to the biomedical applications. Zn-Al LDHs with high potency in drug delivery, bone scaffold and anti-bacterial applications remain less addressed in toxicity concerns compared to Mg-Al LDHs. Hence, the study was designed with synthesis and detailed toxicity evaluation of Zn-Al LDHs in *in-vitro* and *in-vivo* systems.

3.10 Rational behind the selection of the cell lines

For the *in-vitro* evaluation of LDHs toxicity, L929 fibroblast and human osteoblast (HOS) cells were selected. L929 is a fibroblast cell line. They are isolated from subcutaneous connective mouse tissue. L929 cells are included as approved cell lines as per ISO-10993-5-2009 tests for *in-vitro* toxicity and have been widely used for nanomaterial toxicity evaluations [Chaicherd *et al.,* 2019]. L929 cells are common cells in connective tissue and are involved in aiding extracellular matrix formation for tissue support. L929 cells are regarded as a reliable system for understanding toxicity concerns of nanomaterials [Chaicherd *et al.,* 2019]. Previous studies have also used L929 cells as a test system for the biocompatibility evaluation of 3D bone scaffolds [Gurgit *et al*., 2022].

Bone tissue engineering being the most noticed medical application of LDHs, it is uncompromisable to evaluate its compatibility with osteoblast cells. Osteoblasts are key bone cells and are closely involved in bone formation, repair and major functions of bone [Gong *et al.,* 2015]. Osteoblast cells are considered one of the best test models for examining the toxicity potential of bone tissue engineering materials [Albers *et al.,* 2013]. Therefore, HOS cells were selected as the second *in-vitro* test system for the examination of potent toxicity with Zn-Al LDHs. HOS contains mixed, fibroblast and epithelial-like cells. Since the material is explored for bone applications, HOS is the most appropriate cell model.

3.11 Methods

The methodology was designed and adopted to meet the three objectives of present study (Figure 3.1).

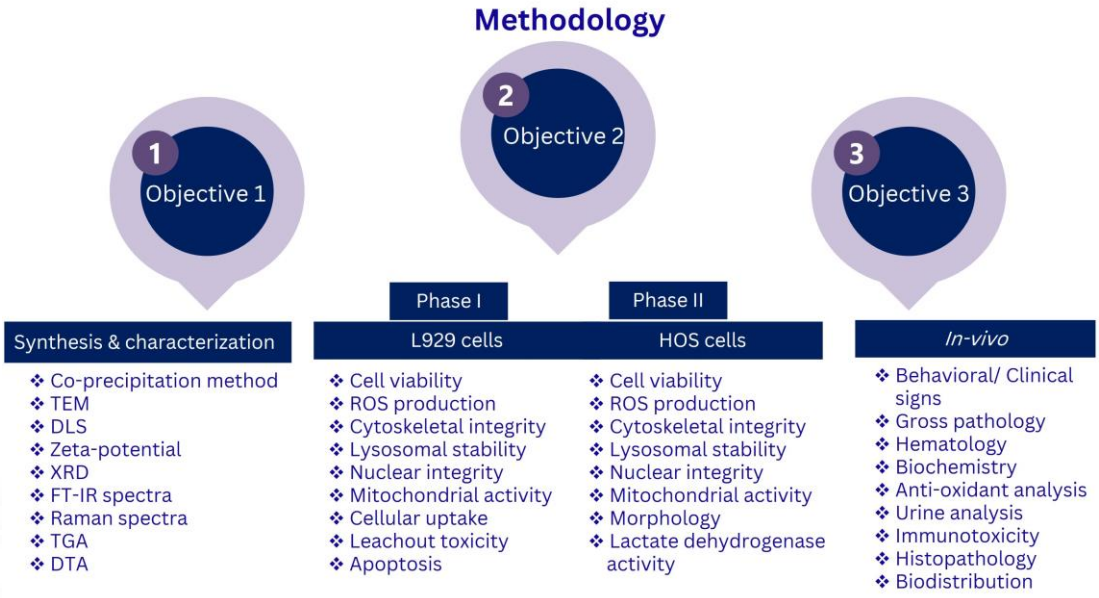

Figure 3.1 Methodology adopted for the study

3.12 Objective I

3.12.1 Synthesis of Zn-Al LDHs

Zn-Al LDHs was synthesized using the co-precipitation method with small amendments from the previous reports [Tathod *et al* 2016, Abderrazek *et al* 2017] so as to suit our laboratory conditions [Figure 3.2]. Nitrate salts of Zinc and Aluminium in the ratio of 2:1 was opted for the synthesis. Solution X containing mixed metal salts and solution Y having alkali mixture were the precursors needed for the synthesis. 10 mL of 30% ethanol having $Zn(NO_3)_26H_2O$ (2 mmoles) and $Al(NO_3)_3.9H_2O$ (1 mmole) was prepared as solution X. Another solution containing 0.15 M NaOH and 0.013 M Na_2CO_3 in 30% ethanol (40 ml) was prepared as solution Y and kept in ice-cold condition. For co-precipitation, solution X containing the metal nitrate mixture was quickly added with the help of a syringe to solution Y (alkali solution) under vigorous stirring. NaOH of molarity 2M was used to adjust the pH to 8 and then stirred for 20

min. Then, the solution was transferred to a Teflon autoclave and treated hydrothermally at 80^0 C for a period of 4 h. Later, the solution was continually washed in de-ionized water by repeated centrifugation and separation till the pH of the supernatant turned 7. Centrifugal separation of Zn-Al LDHs using Eppendorf Refrigerated centrifuge, USA was done by initially centrifuging at a low rpm of 2000 to remove higher particle-sized LDHs. The supernatant obtained after 2000 rpm was centrifuged at 10000 rpm to collect the pellet containing smaller particle-sized LDHs. The washed pellet was then dried at 80^0 C overnight.

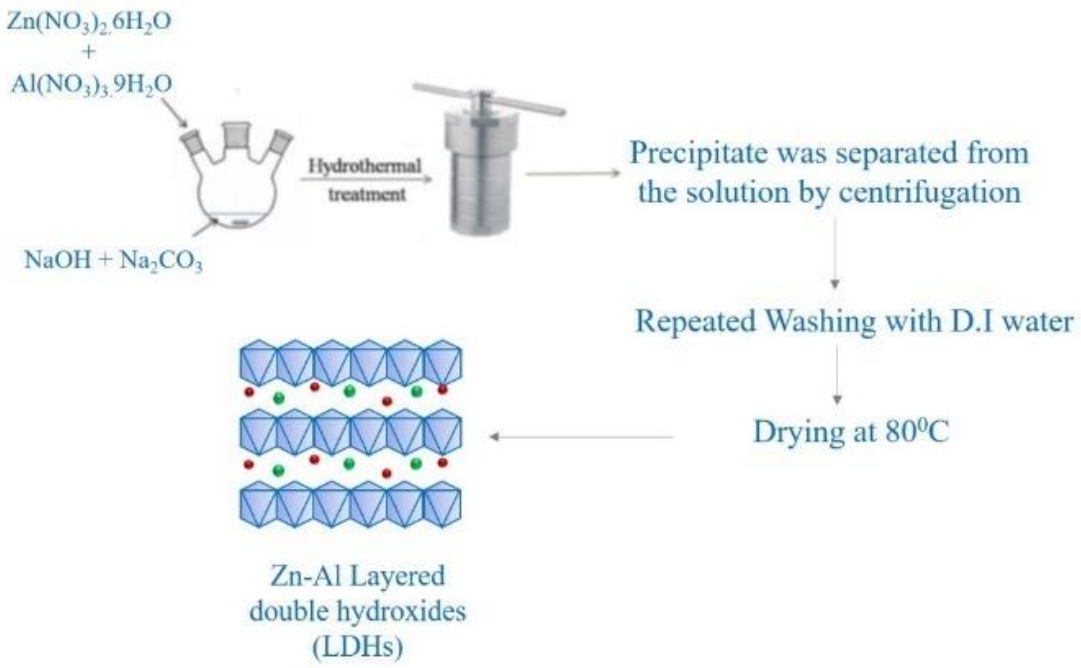

Figure 3.2 Synthesis of Zn-Al LDHs

3.12.2 Characterization of Zn-Al LDHs

The characterization of Zn-Al LDHs in solid-state and in suspension was done. The crystal structure, functional groups, and thermal degradation of the as-synthesized Zn-Al LDHs was carried out using XRD, TEM, Raman spectroscopy, FT-IR, zeta potential, DLS, TGA and DTA. The size and morphology of the synthesized Zn-Al

LDHs were obtained using TEM analysis. The hydrodynamic size, particle size distribution and charge of the LDHs suspension were identified using DLS and zeta-potential analysis.

3.12.2.1 Size and morphological characterization using TEM

The size and shape of the synthesized LDHs, two critical factors were analyzed using the microscopic technique TEM. The dried samples were redispersed in ethanol and sonicated for 20 min in the water bath (Maxwell Professional ultrasonic cleanser, India). The sonicated samples were loaded on to TEM grid of specification 300 mesh copper grid with carbon coating and the ethanol was left to evaporate. After drying, the TEM images were taken using JEOL JEM 2100 TEM, China.

3.12.2.2 Crystal structure and phase identification using XRD

XRD technique was opted for the identification of lattice parameters, crystalline structure and phase of the synthesized Zn-Al LDHs. XRD peak patterns were recorded using a Bruker D8 advanced PXRD. The Cu *K*α (λ=1.5418, Ni monochromator) radiation was applied. The samples were run for the 2Θ value ranging from 10°–90^0. The dried samples were used for the analysis.

3.12.2.3 Chemical group identification using FT-IR spectroscopy

The functional group corresponding to Zn-Al LDHs structure was identified with the help of FT-IR spectroscopy. The spectra of Zn-Al LDHs powder samples were taken using IR Tracer 100, Shimadzu. The spectrum was taken for the range 350-4500 cm^{-1} so as to cover all the characteristic peaks of Zn-Al LDHs.

3.12.2.4 Chemical group identification using Raman spectroscopy

The chemical/ functional groups present in LDHs were identified using Raman spectroscopy. The spectra of dried sample powder were collected from a Confocal

Raman microscope, Alpha 300A, WITec Inc, Germany at an excitation wavelength of 532 nm.

3.12.2.5 Thermal degradation profiling using TGA

LDHs mass change as a function of temperature was evaluated using TGA analysis. The powder Zn-Al LDHs samples were subjected to temperature conditions increasing from room temperature to 850^0 C. The calcinated alumina was kept as reference material. Both reference and samples were kept in platinum cups. The heating rate was 10^0 C/min and the samples were under a nitrogen atmosphere. The DSC-TGA analysis was done in SDT Q600 V8.3, TA instruments, USA.

3.12.2.6 Thermal stability check using DTA

The thermal stability of the synthesized Zn-Al LDHs was examined by DTA analysis. The samples and reference material (calcinated alumina) were heated from room temperature to 800^0 C. The samples were under nitrogen gas with a purge rate of 100±5 ml/min. The analysis was carried out in SDT Q600 V8.3, TA instruments, US.

3.12.2.7 Hydrodynamic size analysis using DLS

Hydrodynamic size represents the size of the nanoparticle in solution based on Brownian diffusion principle [Mourdikoudis *et al.,* 2018]. Zn-Al LDHs was dispersed in ethanol and serum free culture medium and sonicated for 20 min prior to analysis under Malvern Zetasizer Nano ZS (UK). 80 % of the 10 mm cuvette was filled with the Zn-Al LDHs dispersions for the DLS analysis. The polydispersity index (P.D.I) data gives an idea about the dispersity of the Zn-Al LDHs in both the solutions.

3.12.2.8 Charge confirmation using Zeta potential analysis

Zeta potential is a reliable mark for colloidal stability. Hence, the zeta-potential value for the synthesized material in solution was measured to understand its stability and overall charge [Mourdikoudis *et al .,* 2018]. Zn-Al LDHs was dispersed in D.I water

and sonicated for 20 min before the analysis. The sonicated sample was transferred to a capillary cuvette for zeta potential measurement. The net charge of the material was measured with the help of Malvern Zetasizer Nano ZS, UK.

3.13 Evaluation of cellular interactions of 2D Zn-Al LDHs

3.13.1 2D Zn-Al LDHs treatment on *in-vitro* systems

For the particle treatment, 2D Zn-Al LDHs of different concentrations were dispersed in serum free media and sonicated for 15 min before the addition. The exposure doses of Zn-Al LDHs selected for the study were 10 µg/mL, 20 µg/mL, 40 µg/mL, 80 µg/mL and 160 µg/mL and were added 24 h after cell seeding. The statistical analysis was carried out using Student's T test. The data are presented as mean ± standard deviation (S.D). P values < 0.05 were marked * significant, < 0.01 noted ** significant and < 0.001 were given *** significant.

3.13.2 Evaluation of cellular interactions of 2D Zn-Al LDHs with L929 cells

The interaction of the synthesized LDHs with L929 cells was analyzed as the function of different cellular parameters, mechanism of toxicity and compatibility. The cellular uptake permeability, cell viability, mitochondrial activity, lysosomal health, oxidative stress, cytoskeletal integrity, nuclear stability and apoptosis were monitored in L929 cells post-exposure to Zn-Al LDHs.

3.13.2.1 L929 cells culturing and maintenance

L929 cells were cultured in DMEM media provided with 10% FBS and 1% antibiotic/antimycotic (AB/AM) solution. The cells were maintained at incubator conditions set at 37°C and 5% CO_2. The cells were sub-cultured upon attaining 70-80% confluency. For experiments, L929 were seeded either at a density of $1x10^4$cells/well, $5x10^4$cells/well, $1x10^6$cells/well for 96-well plate, 4-well plate and 6-well plate respectively. Particle treatment was done 24 h post cell- seeding.

3.13.2.2 Cellular uptake of 2D Zn-Al LDHs by L929 cells

L929 cells were counted and seeded on to 6-well plate at a density $1x10^6$cells/well. After 24 h, Zn-Al LDHs of concentrations ranging from 10 µg/mL to 160 µg/mL were added to 6-well plate and incubated for 24 h. For negative control, cells were maintained without any particle treatment. Later on, the cells were washed with PBS and trypsinized. The cells were then analysed for side scattering and for cytotoxicity using multichannel Imaging flow cytometry analysis (Amnis Flowsight Imaging flow cytometer).

3.13.2.3 Cellular metabolic activity check using MTT assay

For quantitative cell toxicity assessment, 3-(4, 5-Dimethylthiazol-2-yl)-2, 5-Diphenyl tetrazolium bromide (MTT) assay was adopted. For this, $1x10^4$ L929 cells/well were seeded on to 96-well plate and incubated at 37^0 C and 5 % CO_2. After 24h incubation, the cells were exposed to adopted test concentrations of Zn-Al LDHs. L929 cells with culture media change alone were kept as the negative control. For positive control wells, L929 cells were exposed to phenol. The period of exposure for the assay was selected as 3 h, 6 h, 24 h, and 48 h. After the exposure, the media was removed and 50µg of MTT was added per well and incubated in the dark for 3 h. Later, 100 µl of solubilization solution (DMSO) was added to each well to dissolve the formed formazan crystals and again kept in a dark condition for 15 min. The quantification of formazan is directly correlatable to the active mitochondrial metabolism and quantifiable to the number of viable cells [Riss *et al ., 2016*]. The absorbance of the samples was then measured at wavelength 540 nm using Bio-Tek Instruments Inc, USA. The cell viability was found as a function of mitochondrial activity. The % cell viability was calculated from the absorbance of test groups relative to the control negative group.

3.13.2.4 Cell viability assessment using Live/dead assay

Live dead assay using Calcein AM/ PI staining was done to get an idea of the potential toxicity response of L929 cells when exposed to the synthesized Zn-Al LDHs for a period of 24 h. Calcein AM-PI stains ideally aid for the pictorial representation of viable-dead cell proportion when subjected to microscopic imaging. Theoretically, endogenous esterase enzymes present in viable cells hydrolyses calcein-AM to calcein, which emits green fluorescence [Monteiro-Riviere *et al.,* 2009]. PI enters only through the damaged/ ruptured membrane and stains only dead cells red. Therefore, live cells are stained green by calcein AM stain while damaged cell structure/ dead cells are seen as red. 5×10^4 cells /well were seeded for the imaging purpose. The cells were subjected to particle exposure for 24 h. Untreated cells were kept as the negative control. After 24 h, the cells were double stained with 1 µg/ml calcein AM stain for 15 min, followed by 0.25 µl PI stain for 5 min. The cells were later washed with PBS to remove the excess stain. The cells were observed under the microscope and images were captured for different treatment groups.

3.13.2.5 Cellular viability and lysosomal damage check by NRU assay

NRU is a calorimetric cell viability assay and serves as a reliable indicator for lysosomal damage [Repetto *et al.,* 2008]. For experimentation, $1x10^4$ L929 cells/well were seeded on 96 well plates and left to get 70-80 % confluent under incubation conditions for 24 h. The cells were then treated with Zn-Al LDHs in incrementing concentrations, except for negative control for which cells were provided with culture media alone. Phenol (0.1mM) was added to wells kept as the positive control. The cells were exposed to treatment for 3 h, 6 h, 24 h and 48 h and then replaced with neutral red dye (10 µl of 1% solution). The cells were incubated for 2 h for NRU uptake. The cells were then washed well with sterile PBS. Plates were observed under a compound microscope for imaging. 100 µl of solubilizing solution (acid alcohol: 1% glacial acetic acid and 50% ethanol) was added to all the respective wells and shaken using Innova

4080 incubator shaker- New Brunswick Scientific, for 20 min for proper extraction. Then the absorbance was measured at wavelength 540 nm using a microplate reader (Bio-Tek Instruments Inc, USA).

3.13.2.6 Lysosomal integrity assessment using Acridine orange staining

Acridine orange (AO) staining was carried out to confirm the lysosomal integrity after exposure to Zn-Al LDHs. AO comes under the lysosomotropic type of dyes and fluoresces red in normal healthy lysosomes where the pH is acidic. On the other hand, when the lysosomes undergo damage leading to lysosomal membrane rupture and leakage to cytoplasm, AO is stained green (alkaline pH of cytoplasm). So, shift in red florescence to green is noted as an indicator of lysosomal damage and dysfunction (Jiang, Q *et al.,* 2016). L929 cells were added to a 4-well plate (of 5×10^4 cells /well) and left to adhere to the plate surface. Particle exposure was given 24 h after cell seeding and then maintained for 24 h at 5% CO_2 condition and at a temperature of 37^0 C. After the specified time of exposure, media was replaced with media containing 2 µg/ml acridine orange and incubated in dark for 15 min. The cells were then PBS washed thrice to get rid of surplus dye. The images were taken in red and green filters under a fluorescence microscope (Axio Scope.A1, Carl Zeiss, Germany).

3.13.2.7 Oxidative stress assessment using DCFH-DA assay

ROS production, a major marker for oxidative stress-induced cellular toxicity was evaluated with the help of DCFH-DA (2,7-dichlorodihydrofluorescein diacetate) assay [Aranda *et al.,* 2013]. $1x10^4$ L929 cells/well were seeded on 96 well plates. After 24 h, the plate was observed under the microscope to confirm confluency to be around 70%. Then, DCFH-DA (100 µl of 1 µM concentration) was added to the specific wells and incubated in dark for 45 min. Followed by particle treatment in varying concentrations of 10 µg/mL, 20 µg/mL, 40 µg/mL, 80 µg/mL and 160 µg/mL of LDHs for 24 h. The positive control wells were exposed to 0.09% hydrogen peroxide (H_2O_2).

After the treatment period, fluorescence was measured at excitation and emission wavelengths 450 and 535 nm using a microplate reader (Plate Chameleon TM V, Hidex, Finland).

3.13.2.8 Cytoskeletal and nuclear integrity screening using Rhodamine-phalloidin-DAPI staining

The cytoskeleton structure of L929 cells post-exposure to Zn-Al LDHs was examined by using the F-actin stain – rhodamine-phalloidin and the chances of nuclear destruction were evaluated by counter-staining the cells with DAPI. Rhodamine-phalloidin is an F-actin (a major component of the cytoskeleton) marker that fluorescence in red [Chazotte 2010]. DAPI is a fluorescent dye that preferentially binds to the minor grooves of DNA (Thymine-Adenine) and labels nuclei strongly in bright blue [Chazotte 2011]. Rhodamine-phalloidin/ DAPI dual staining is an excellent option for cytoskeleton-nuclei visualization.

Therefore, 5×10^4 cells /well were added to a 4-well plate and incubated for 24 h inorder to attach and attain 70% confluency. The cells were then exposed to selected doses of Zn-Al LDHs (10 µg/mL, 20 µg/mL, 40 µg/mL, 80 µg/mL and 160 µg/mL). Control cells were supplemented with media alone. Therefore, cells were fixed before staining. Cell fixing was done after particle exposure by initially providing PBS washing to all wells and then exposing them to 4 % paraformaldehyde for 10 min. Excess aldehyde

was quenched by incubating with 0.1 M glycine (in PBS) for 5 min. The cells were then permeabilized by exposing them to 0.1 % Triton-X 100 solution for two min. Then rhodamine- phalloidin stain in PBS in ratio of 1: 250 was added and incubated for 15 min. Later, the solution was replaced with DAPI stain for 1 min. The cells were then PBS washed to remove excess stain and were imaged under the red and blue filter of a fluorescence microscope (Axio Scope.A1, Carl Zeiss, Germany).

3.13.2.9 Nuclear integrity and apoptosis estimation using DNA laddering

DNA fragmentation is a major marker of apoptosis and nuclear toxicity. DNA laddering has been used for ages as a detection technique for apoptosis and it works by utilizing electrophoresis for screening DNA fragmentation. For this, DNA isolated from cells exposed to the test material (scrutinized for toxicity) is loaded onto agarose gel and visualized using stains like EtBr. The loaded agarose gel is then run under electrophoresis to separate the DNA fragments before imaging [Marquis *et al.,* 2009]. In the present study, DNA laddering was done as a marker test for the apoptosis-inducing tendency of Zn-Al LDHs. For the assay, 1 $x10^6$ cells were seeded in 6-well plate and incubated for cell attachment. The seeded cells were exposed to the chosen concentrations of Zn-Al LDHs. Cells in untreated wells served as the negative control group. Genomic DNA was isolated and ladder assay was executed strictly following the instructions in the manufacture's guidelines of Quick Apoptotic DNA ladder detection kit. After the treatment period of 24 h, the cells were harvested, washed with PBS and lysed with the addition of 35 µl of TE lysis buffer and 5 µl Enzyme A. The cells were then incubated in the water bath (37^0 C) for 10 min. Later enzyme B was added and incubated for half an hour at 50 °C. DNA was precipitated at -20 °C with the help of ammonium acetate and absolute ethanol. The pellet obtained was left for 10 min to air-dry and then resuspended in DNA suspension buffer of volume 30 µl. Meanwhile, 1.2 % agarose gel was prepared having 0.5 µg/ml ethidium bromide in 1X TBE (Tris/Borate/EDTA). The isolated DNA was loaded onto the prepared agarose gel and run for 1-2 h at 5 V/cm. DNA bands were imaged using gel doc imager (Bio Imaging system, Syngene, UK).

3.13.2.10 Apoptosis/ Necrosis detection by Annexin-PI flow cytometry analysis

Inorder to look over the possible cell fate on Zn-Al LDHs exposure and quantify the number of cells undergoing necrosis/ apoptosis pathway, flow cytometry analysis using Annexin/PI staining was adopted. The working principle behind Annexin

staining for apoptosis detection is as follows. Apoptotic cells project phosphatidylserine (PS) on the cell membrane surface contrary to normal cells and therefore projected PS are used as a marker for apoptosis. Annexin contains phospholipid-binding protein with phosphatidylserine affinity. Further, FITC conjugated Annexin binding onto phosphatidylserine group makes apoptotic cells fluoresce in green. PI is taken up only in case of the damaged cell membrane by dead cells and is therefore internalized only in dead cells. Hence, cells dead via the necrosis pathway are distinguishable with apoptotic cells-stained fluorescent red [Lu X *et al.,* 2011]. For this experiment, L929 cells were seeded onto a 6-well plate with a density of 1 $x10^6$ cells/ well. n attachment, the cells were subjected to Zn-Al LDHs exposure. The control cells were given media change alone. The cells after 24 h were trypsinized and the pellet was resuspended in 50 µl annexin binding buffer. Further, 5 µl of Annexin V and incubated for 15 min. Then, 1 µl of propidium iodide was added and incubated for 5 min. The cells were then analyzed using Amnis Flowsight Imaging flow cytometer.

3.13.2.11 Leachout toxicity

Since the synthesized LDHs contain Zn and Al ions, chances of leach-out toxicity were considered for examination. For this, leachout were collected as per ISO-10993-5-2009(e) Test on extracts. Zn-Al LDHs were incubated for 24 and 72 h in serum-free DMEM media at 37^0 C. The supernatant solution (media) was collected after 24 h and 72 h by centrifugation at 10000 rpm.

3.13.2.11.1 Metabolic activity assessment using MTT assay

The cytotoxic effect of the particle dissolution in DMEM culture media was inspected using MTT assay. $1x10^4$ L929 cells/well were seeded on to a 96-well plate and after attaining confluency for test, the cells were exposed to varying concentrations of

collected supernatants. Further, MTT assay was carried out as described in section 3.11.2.3.

3.13.2.11.2 Lysosomal activity evaluation using NRU assay

NRU assay was further carried out to confirm the cytocompatibility and lysosomal activity of L929 cells on contact with Zn-Al LDHs extract. The extract at different concentrations were added to wells 24 h post-seeding in 96 well plate with a density of $1x10^4$ / well. After 24 h and 72 h, NRU assay was done as per protocol given in section 3.11.2.5.

3.13.3 Evaluation of cellular interactions of 2D Zn-Al LDHs with HOS cells

Since one of the prime applications of 2D Zn-Al LDHs is in bone tissue engineering, it is of supreme importance to check its compatibility with osteoblast cells. On this thread, the cytotoxicity of the synthesized Zn-Al LDHs was scrutinized on light to HOS cells. The dose concentrations selected were the same as described in section 3.9.1. The HOS cells were examined for mitochondrial damage, lysosomal activity, morphological changes, ROS production, lactate dehydrogenase enzyme release, cytoskeletal integrity, nuclear integrity on introduction to Zn-Al LDHs.

3.13.3.1 HOS cell maintenance

HOS cells were grown in MEM culture media supplemented with 10% FBS and 1% antibiotic/antimycotic (AB/AM) solution. The cells were maintained at temperature of 37°C and 5% CO_2. For different assays, the cells at 70-80% confluency were used and seeded at a density of $1x10^4$cells/well, $5x10^4$cells/well, $1x10^6$cells/well on 96-well plate, 4-well plate and 6-well plate respectively depending upon the experimental requirement.

3.13.3.2 Cellular viability and metabolic activity check by MTT assay

The consequence of Zn-Al LDHs treatment on the mitochondrial activity of HOS cells was examined with MTT assay. HOS cells were counted and added to 96 well plate at $1x10^4$ HOS cells/ well. Next day, the cells were exposed to Zn-Al LDHs doses for 3 h, 24 h and 48 h. For the negative control wells, media change alone was given while phenol was added to wells specified for the positive control. MTT assay was then carried out as given in section 3.11.2.3.

3.13.3.3 Cellular cytotoxicity examination using live-dead assay

For getting a qualitative figure on the potential cytotoxicity of Zn-Al LDHs on HOS cells, the live-dead assay was executed using AO/ ethidium bromide (EtBr) staining. With the dual staining, the AO stains viable cells as green while the PI enters only damaged cells giving red fluorescence to dead cells. For AO/Et Br staining of Zn-Al LDHs on HOS cells, $5x10^4$cells/well were plated on 4-well plate for the assay. Next day, the cells were then treated with 10 µg/mL, 20 µg/mL, 40 µg/mL, 80 µg/mL and 160 µg/mL concentrations of Zn-Al LDHs. The cells in each well were trypsinized after 24 h and the pellets collected were incubated with MEM media containing AO stain for 10 min followed by EtBr for 5 min. The cells were washed and resuspended well to have even distribution of cells in media. Fixed volume of the cell suspension was positioned on glass slide and a coverslip was placed over the droplet. The glass slide was further observed under fluorescence microscope.

3.13.3.4 Mitochondrial membrane potential (MMP) by JC1 staining

JC1 is a fluorescent dye that fluoresces in red when agglomerated and emit green fluorescence in monomeric form. The JC1 dye shows preferential piling up and agglomerate formation in the mitochondria of normal active cells. For weak and injured cells having mitochondrial damage, the JC1 exists as monomer. The red/ green fluorescence showcases drop in MMP, indicative of mitochondrial damage/

cytotoxicity [Elefantova, K *et al.,* 2018]. For a qualitative understanding on the latent chances of mitochondrial damage caused by Zn-Al LDHs, the exposed cells were subjected to JC1 staining. $5x10^4$ cells/well were seeded onto 4-well plate and the cells were then left to attain 70-80 % confluency. Then, the cells were treated with selected dose concentrations of Zn-Al LDHs and the cells were placed in the incubator for 24 h. After the opted exposure period, the cells were then incubated with JC1 stain for 15 min. The cells were PBS-washed to remove the excess stain and imaged under red and green filters in a fluorescence microscope.

3.13.3.5 Morphological analysis by Giemsa staining

In order to estimate the possibility of morphological damage post exposure to Zn-Al LDHs, giemsa staining on HOS cells was done. $5x10^4$cells/well were grown on 4-well plates and 24 h after seeding, the cells were treated with varying concentrations of Zn-Al LDHs. After the selected treatmenttime of 24 h, the culture media was replaced with ice-cold PBS followed by 4 % paraformaldehyde for 15 min. After fixing, the cells were stained by incubating for 5 min with 10 % Giemsa solution. The cells were then again washed with PBS before imaging under the compound microscope.

3.13.3.6 Morphological analysis by Coomassie brilliant blue staining

Coomassie brilliant blue staining of HOS cells was done for further confirmation on morphological integrity. $1x10^6$ HOS cells/well were seeded onto 6- well plate and the cells were left for 24 h to attain 70-80% confluency. The cells were later on treated with chosen concentrations of Zn-Al LDHs for 24 h. Next day, the media was removed and the wells were washed with ice-cold PBS before fixation using 4 % paraformaldehyde. The fixed cells were later stained using Coomassie brilliant blue staining for 5 min. The cells were washed thoroughly with PBS before imaging under the compound microscope.

3.13.3.7 Oxidative stress assessment using DCFH-DA assay

HOS cells were counted and seeded on to 96- well culture plates with a density of $1x10^4$ cells/ well. The cells were then treated with opted concentrations of Zn-Al LDHs in the range 10 to 160 µg/mL for 6 h, 24 h and 48 h. The cells were then subjected to DCFH-DA assay following the protocol described in section 3.11.2.7.

3.13.3.8 Cell membrane damage check using lactate dehydrogenase enzyme assay

Lactate dehydrogenase is an enzyme exclusively found in cytoplasm and gets released onto extracellular portion only after membrane breakage. Therefore, the detection of the abovementioned enzyme in supernatant solution is used as a marker of cell membrane damage. The membrane destruction is involved in different cell death mechanisms inclusive of apoptosis and necrosis. Therefore, lactate dehydrogenase enzyme assay is used as a checkpoint for mechanical stress [Kumar *et al.,* 2018]. $1x10^4$ HOS cells/ well were plated on a 96-well culture plate and left to attain 70-80 % confluency. The cells were then exposed to Zn-Al LDHs (chosen doses). HOS cells treated with LPS served for positive control while untreated cells were kept as negative control group. After 6 h and 24 h exposure, the supernatant media from each treatment group was collected and added on to another clean 96 well plate. The activity of lactate dehydrogenase enzyme in the collected supernatant was estimated following the maker's protocol specified in lactate dehydrogenase detection kit. The plate was then read at 540 nm using Bio-Tek Instruments Inc, USA microplate reader.

3.13.3.9 Lysosomal integrity assessment using Acridine orange staining

The effect of Zn-Al LDHs on lysosomal integrity of osteoblast cells was analyzed by qualitatively by AO staining of HOS cells. 4-well culture plates were seeded with $5x10^4$cells/well and on 80 % confluency, the cells were treated with different concentrations of Zn-Al LDHs. Media was removed after 24 h treatment period and

replaced with media containing AO stain. The AO staining assay was carried out as described in section 3.11.2.5.

3.13.3.10 Cytoskeletal and nuclear integrity screening using Rhodamine-phalloidin-DAPI staining

$5x10^4$cells/well were seeded onto culture plate (4-well) and incubated for 24 h. Later the cells were treated with different concentrations of Zn-Al LDHs for 24 h and stained with Rhodamine-phalloidin -DAPI dual staining to visualize the effect of the particles on osteoblast cytoskeleton and nuclei. The cells after the specified exposure time were stained following the protocol discussed in section 3.11.2.8.

3.13.3.11 Nuclear integrity and apoptosis estimation using DNA laddering

The consequence of Zn-Al LDHs exposure on osteoblast DNA was analyzed using DNA laddering, which also serves as a sure-shot marker for apoptosis. The HOS cells were seeded on to culture plates (6-well) with a density of $1x10^6$ HOS cells per well. The cells were exposed to opted Zn-Al LDHs concentrations on the next day. Later DNA laddering assay was carried out as per procedure given in section 3.9.2.9.

3.14 Toxicity evaluation of 2D Zn-Al layered double hydroxides in rat model

Toxicity study using Wistar rat model was conducted to understand the impact of the Zn-Al LDHs at *in-vivo* level. Figure 3.3 represents the design followed for the *in-vivo* study. The parameters overlooked were behavioral/ Clinical signs, gross pathology, hematology, serum biochemistry, anti-oxidant analysis, urine analysis, immunotoxicity, histopathology and biodistribution.

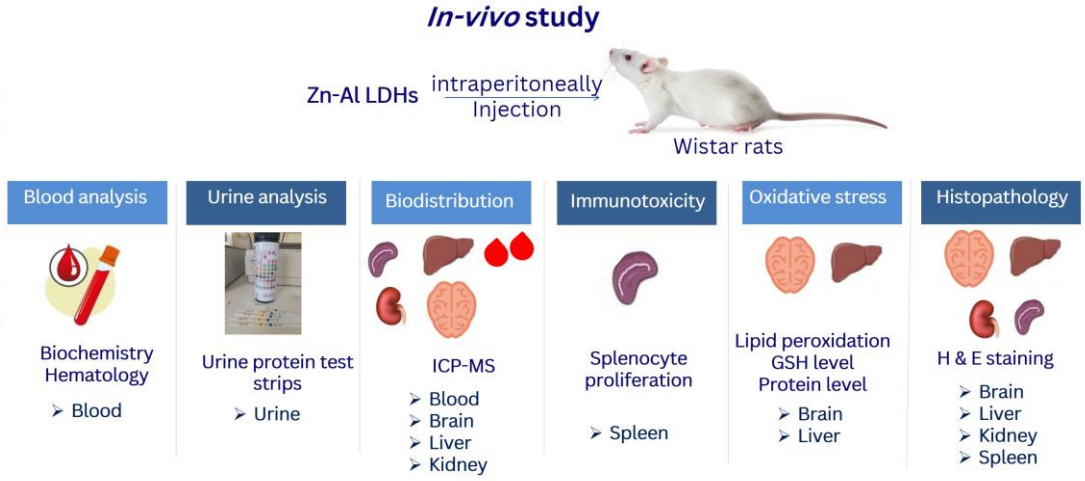

Figure 3.3: *In-vivo* toxicity study of Zn-Al LDHs using Wistar rats

3.14.1 Animal experiment design and dose

The purpose of the study was to get a toxicity profile of Zn-Al LDHs when exposed to Wistar rats and the profound effects upto 14 days. The protocol followed for the study was approved by the animal ethical committee at Sree Chitra Tirunal Institute for Medical Sciences and Technology, TVM. For the experimentation, 12 Wistar rats were divided into 4 groups with 3 animals each (Table 3.1). The timeline for the study was upto 14 days from the day of exposure and the animals were monitored for any abnormal activity throughout the study period. The group 1 rats were injected with

saline alone and were kept as the control group. Group 2, 3 and 4 received 10mg/Kg dose concentration of Zn-Al LDHs intraperitoneally and was sacrificed on day 3rd, 7th and 14th respectively.

The body weight of the test rats were noted on the exposure as well as on the sacrificing days. The blood and urine samples were collected before the euthanization for analysis. Animals were checked for gross pathology upon sacrifice. Brain, kidney, liver and spleen were obtained from the experimental animals and the organ weights were noted. The organs were subjected to biodistribution and histopathological studies. Brain and liver were also analyzed for oxidative stress. The collected spleen was checked for proliferation capacity as well.

	Group	Mode of exposure	Dose	No of animals
I	Control	i.p	Saline	3
II	3 days	i.p	10mg/Kg of Zn-Al LDH	3
III	7 days	i.p	10mg/Kg of Zn-Al LDH	3
IV	14 days	i.p	10mg/Kg of Zn-Al LDH	3

Table 3.1: *In-vivo* experiment design.

3.14.2 Clinical signs

The rats in all groups were monitored throughout the study timeline to figure out any differences in behavioral or clinical patterns. Features of the Wistar rats like eyes, fur, ear, nose mouth, skin were observed for any visible change. Also, deviations in eating, drinking, grooming,motion, posture, piloerection, responsiveness to the surroundings

from normal behaviour were overlooked. Also, chances of dehydration, weight loss, swelling *etc*., were monitored throughout the experimental period.

3.14.3 Body weight

The body weight of Wistar rats on the 0^{th} day (day of dose administration) and on the day of sacrifice were noted. The weight was noted to check for any aberration in body weight on account of toxic response to the administered Zn-Al LDHs.

3.14.4 Urine and blood collection

Blood and urine samples were procured from all the test animals for analysis. Blood was collected from orbital sinus and collected in tubes for biochemistry, hematology and ICP analysis.

3.14.5 Hematology

The blood samples from the Wistar rats on the day of sacrifice were collected into anticoagulant tubes for hematology. The collected samples were analyzed for platelet, white blood cells, red blood cells and haemoglobin content using automated hematology analyzer (Horiba Vet abc (Japan).

3.14.6 Biochemistry

Serum was isolated from the acquired blood samples by initially allowing the blood to clot, followed by centrifugation for 15 min at a centrifugal speed of 3500 rpm. The various parameters like albumin, protein, creatinine, cholesterol, alkaline phosphatase (ALP), aspartate aminotransferase (AST), alanine transaminase (ALT) in collected samples was scrutinized using biochemical analyzer (Erba Mannheim, Germany) in order to get a portrait of the effect on liver and kidney function as well.

3.14.7 Urine analysis

Urine was collected from the rats on day of sacrifice post-administration of test samples and analysed for presence of different factors including leucocytes, nitrites, blood, ketones, bilirubin and glucose. The amount of urobilinogen and protein was also estimated. In addition, the pH and specific gravity of the collected samples were also inspected with the help of Uro-dipchek 300 (Erba Mannheim, Germany).

3.14.8 Gross pathology

The animals were euthanized on 3rd, 7th and 14th day of i.p administration by cervical dislocation. Upon sacrifice all the rats were checked for any gross abnormalities and lesions. The animals were cross-examined for any observable colour change or lumps at the surface of tissues.

3.14.9 Organ collection

On euthanization, four organs- brain, kidney, liver and spleen were collected. The organ weight for all four organs from all the animals were weighed and noted for concluding inference on any potential organ toxicity. The organs were further divided and allotted for biodistribution and histopathology studies. Part of the liver and brain were also used for anti-oxidant assays. Portions of the isolated spleens were allocated for splenocyte proliferation studies.

3.14.10 Anti-oxidant assays

Anti-oxidant assays were carried out on liver and brain collected from euthanized mice belonging to all four test groups. The organ samples were washed with the help of saline and then kept at ice-cold condition. Tissue homogenate (10%) was prepared using 0.1 M phosphate buffer. The pH of the buffer was cross-checked to be 7.4 before use. Polytron P 3100 (Switzerland) tissue homogeniser was used to homogenize the tissue and the opted speed was 1000 rpm. The formed homogenate was centrifuged at

3500 rpm for a time period of 10 min using a refrigerated centrifuge set at 4 °C. The supernatant was collected and stored at ice-cold temperature till use.

3.14.10.1 Protein level in brain and liver

Lowry's method was opted for estimating the protein level in brain and liver collected from the *in-vivo* study rats. Table 3.3 holds the summarized format of the followed protocol. The blank was constituted with 1 ml distilled water and 5 ml solution C made by mixing 1 mL of solution containing 10 mg sodium potassium tartarate & 5 mg copper sulphate along with 50 mL solution of sodium carbonate (Na_2CO_3). The Na_2CO_3 solution was made by dissolving 1 g in 50 ml distilled water.

The test samples were prepared by mixing 0.1 mL of sample in 0.9 mL distilled water and adding 5 mL of solution C. The samples were then incubated for 15 min at room temperature. Then 0.5 mL of Folin's reagent was added and incubated for 30 min in dark and then read at 660 nm using Lambda 25, UV/Vis spectrophotometer, Perkin Elmer, USA. The BSA standard graph was used for obtaining the protein concentration.

Reagent	**Distilled water**	**Sample**	**Solution C**	**Folin's reagent (added after 15 min incubation)**
Blank	1 mL	-	5 mL	0.5 mL
Test	0.9 mL	0.1 mL	5 mL	0.5 mL

Table 3.2: Lowry's method for protein estimation.

3.14.10.2 GSH level

Moron's method was followed to find the GSH level in liver and brain procured from the Zn-Al LDHs exposed rats. Moron's method involves usage of DTNB [5, 5'-

dithiobis-(2-nitrobenzoic acid)] and the used DTNB reacts with the GSH forming a yellow product. The blanks were prepared with 4 mL of 0.2M phosphate buffer having pH 8, 0.5 mL of 2mM DTNB and 0.5 mL of distilled water. The samples were prepared by mixing 0.5 mL tissue homogenate (liver/ brain) in solution of 4 mL of 0.2M phosphate buffer having pH 8 and 0.5 mL of 2mM DTNB. The end product was quantified by detecting absorbance at 412 nm using UV-Vis spectrophotometer, Perkin Elmer, USA.

3.14.10.3 LPO level

The LPO levels in liver and brain were estimated by Ohkawa *et al.,* 1979. In Ohkawa method, thiobarbituric acid (TBA) was used as for the detection of malondialdehyde (MDA): a lipid peroxide by measuring using Lambda 25, UV/Vis spectrophotometer, Perkin Elmer, USA spectrophotometer. For the blank, 1.5 ml of 0.8% TBA, 0.2 mL 1% SDS, 1.5 mL of 20% acetic acid mixed in 1 ml distilled water while for the samples, 1.5 ml of 0.8% TBA, 1.5 mL of 20% acetic acid, 0.2 mL 1% SDS, 0.2 mL tissue homogenate was mixed in 0.8 ml distilled water. The blanks and the samples were kept for 1 h in water bath maintained at 90^0 C. After the incubation, 1 ml distilled water was added again and then centrifuged for 10 min at 3500 rpm. The absorbance measurement of the collected supernatant was measured at 532 nm.

3.14.11 Biodistribution

Fate of the nanoparticles at *in-vivo* level is a major concern associated with its application and exposure. Biodistribution is a major decisive factor influencing the applicability as well as the toxicity concerns of nanoparticles. In this study, ICP-MS was done to evaluation of accumulation of Zn-AL LDHs in liver, kidney and brain. The amount of Zn^{2+} and Al^{3+} in blood was also estimated. The procured samples were stored at -20^0 C till analysis. For the analysis initially, dried samples were homogenized and then digested. Microwave-assisted digestion was done as given in figure 3.6. 0.1g of the sample was digested and analyzed using Inductively coupled

plasma spectrometer iCAP RQ (Make: Thermo Scientific) equipped with quadrupole mass analyser and an autosampler ASX-280 (Teledyne, CETAC Technologies, USA).

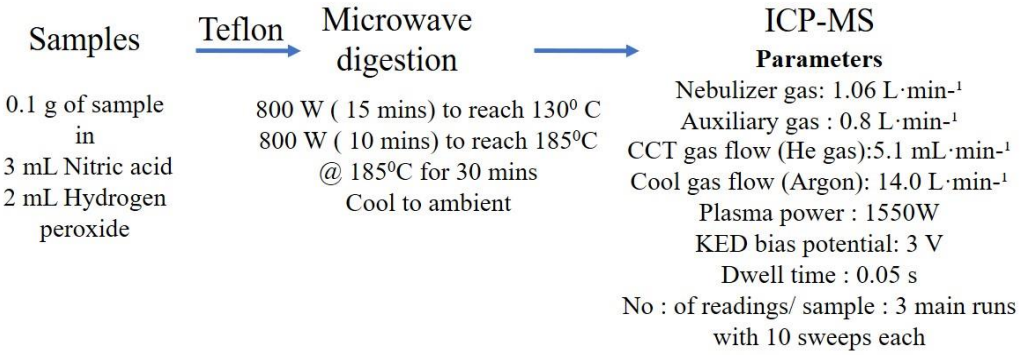

Figure 3.4: Processing and operation for ICP analysis

3.14.12 Splenocyte proliferation

Splenocyte proliferation assay was done as a marker for potential toxicity to spleen on exposure to Zn-Al LDHs. The collected spleens were kept in ice-cold PBS containing AB/AM. The spleen was mashed over a metallic strainer and the single-cell suspension was collected in a Petri plate underneath. The suspension was then placed slowly over histopaque and then centrifuged for 40 min at a speed of 4000 rpm. The centrifugation yields a buffy coat that is washed three times with PBS. The cells after counting and were added to 6-well plate with a density of $2x10^5$cells/well in RPMI medium containing 10% FBS and 1% AB/AM. The cells were incubated for 72 h before adding 0.5µCi of 95 tritiated thymidine. The seeded cells were again incubated for 72 h at 37^0 C and 5% CO_2. The cells were then fixed with 5% trichloroacetic acid and lysed with SDS/NaOH lysis buffer. After that the radioactivity was measured using scintillation counter (Hidex, Finland).

3.14.13 Histopathology

Histopathology examination was done on major collected organs like liver, brain, kidney and spleen. The collected organs were immediately washed with PBS and fixed in 10% formaldehyde. The histopathology experiment involved 6 major steps: tissue processing, embedding, sectioning, slide preparation, Hematoxin and eosin (H & E) staining and imaging. Three biological and technical triplicates were taken for the study.

3.14.13.1 Tissue processing

Tissue samples (Liver, kidney, brain and spleen) were cut into small pieces and then kept inside the cassette. The samples were then dehydrated using isopropanol, cleared in xylene and steadily infiltrated in paraffin wax to make thin sectioning possible (Figure 3.8).

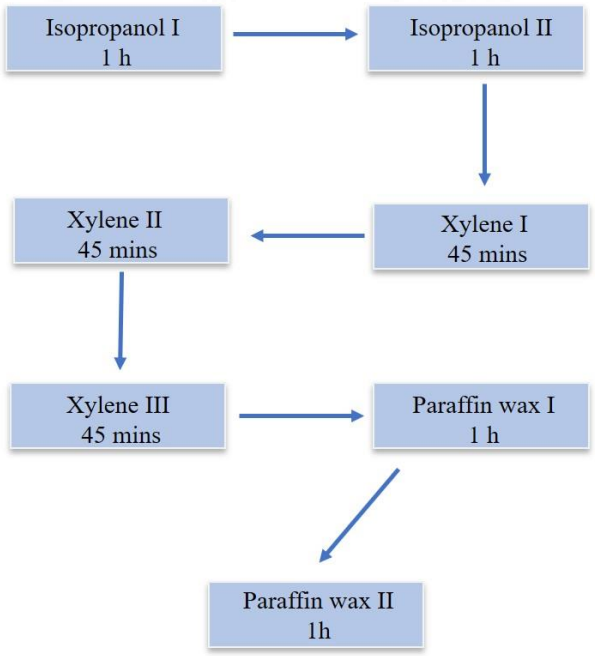

Figure 3.5: Tissue processing for histopathology

3.14.13.2 Embedding

The processed tissue sections were removed from cassettes, placed over molds and filled with liquid paraffin wax. The molds were then cooled to fix the tissue sections in paraffin wax.

3.14.13.3 Sectioning

The paraffin blocks embedded with processed tissue sections were sectioned using disposable metal knives (Leica RM 2125 RT, Germany). The blocks were cooled and trimmed before sectioning to expose the embedded tissues. The sections with 5 µm thickness were cut and let to float on warm water bath for proper expansion and to avoid unwanted folds. The sections were then taken onto albumin precoated glass slides and kept in an incubator set at 37^0 C to dry. The used glass slides were pre-coated with Meyer's egg albumin for proper adhesion of the tissue sections onto glass slides.

3.14.13.4 Staining using H& E stain

For checking on any possible tissue degeneration on exposure to Zn-Al LDHs, H & E staining was opted so as to have pictorial evidence. Hematoxylin stains the acidic components of cells purple while Eosin stains the basic components as pink. The staining was done following a set of consecutive steps as depicted in the table 3.9.

STEP NO	SOLUTION	EXPOSURE TYPE	TIME
1	Xylene I	Immersion	10 min
2	Xylene II	Immersion	10 min
3	Absolute alcohol	Immersion	5 min
4	70 % alcohol	Immersion	5 min

5	Distilled water	Immersion	5 min
6	Harris Hematoxylin	Immersion	20 min
7	Distilled water	Rinse	Once
8	Acid alcohol	Dip	1-2 dip
9	Distilled water	Rinse	Once
10	Scott's tap water	Immersion	3 min
11	Distilled water	Rinse	once
12	Eosin	Immersion	1 min
13	Distilled water	Rinse	Once
14	70 % alcohol	Immersion	2 min
15	Absolute alcohol	Immersion	1 min

Table 3.3: Steps for H and E staining of tissue sections

The stained slides were kept for drying (evaporation of excess solvents) and then mounted with DPX.

3.14.13.5 Imaging

The mounted slides were observed and imaged under microscope.

RESULTS

4. RESULTS

4.1 *Synthesis and Physico-chemical characterization of 2D Zn-Al LDHs*

4.1.1 Synthesis of Zn-Al LDHs

Zn-Al LDHs was synthesized by co-precipitation method. Upon quick injection of nitrate salts of Zinc and Aluminium (2:1 ratio) into basic solution containing NaOH and sodium carbonate at ice-cold condition, a white precipitate was formed. The resulting colloidal solution was further aged at 80^0 C for 4 h. The white dispersion obtained after hydrothermal aging was repeatedly washed with de-ionized water to remove unwanted reactants. Higher-sized particles were separated by centrifugation at 2000 rpm. Low-particle size Zn-Al LDHs were obtained by centrifugation at 10000 rpm. Pellets obtained were dried at 80^0 C and redispersed according to experimental needs. The Zn-Al LDHs redispersed in water/ ethanol/ culture media were sonicated for 20 min to obtain stable dispersion.

4.1.2 Characterization of Zn-Al LDHs

The synthesized Zn-Al LDHs was characterized using different techniques.

4.1.2.1 Size and morphological characterization using TEM

TEM imaging is a relied characterization technique to confirm two of the important parameters of nanoparticles: morphology and particle size. The TEM imaging of the synthesized Zn-Al LDHs showed a size distribution of 85 nm to 150 nm. The average size was obtained as ~102 nm. The electron microscope images also showed that the formed Zn-Al LDHs possessed a hexagonal morphology (Figure 4.1).

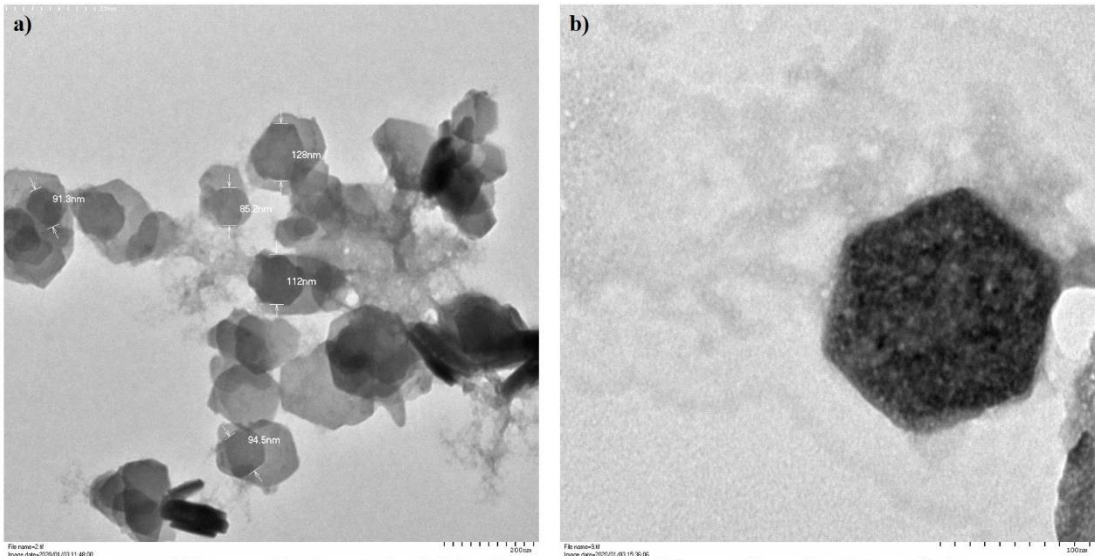

Figure 4.1: TEM images of synthesized Zn-Al LDHs. a) Size and particle size distribution, Magnification 15.0k, scale bar 200 nm b) Morphology of Zn-Al LDHs, Magnification 50.0k, scale bar 100 nm.

4.1.2.2 Crystal structure and phase identification using XRD

XRD analysis confirmed the lamellar structure of LDHs. The peaks were sharp depicting crystalline nature for the prepared Zn-Al LDHs. The XRD spectra obtained showed reflections at 2Ɵ value 11.74, 23.48, 34.61, 39.18, 46.8, 60.19, 61.56. Upon calculation, corresponding miller indexes were obtained as (003), (006), (009), (015) (018), (110) and (113). The (003), (006), and (009) correspond to basal peaks denoting characteristic reflections of Zn-Al LDHs. The peaks corresponding to (015), (018), (110) and (113) were from the non-basal reflections of Zn-Al LDHs. The d spacing (003), a value and c value of the synthesized Zn-Al LDHs was found to be 0.75 nm, 0.307 nm and 2.25 nm. The XRD pattern is shown in Figure 4.2.

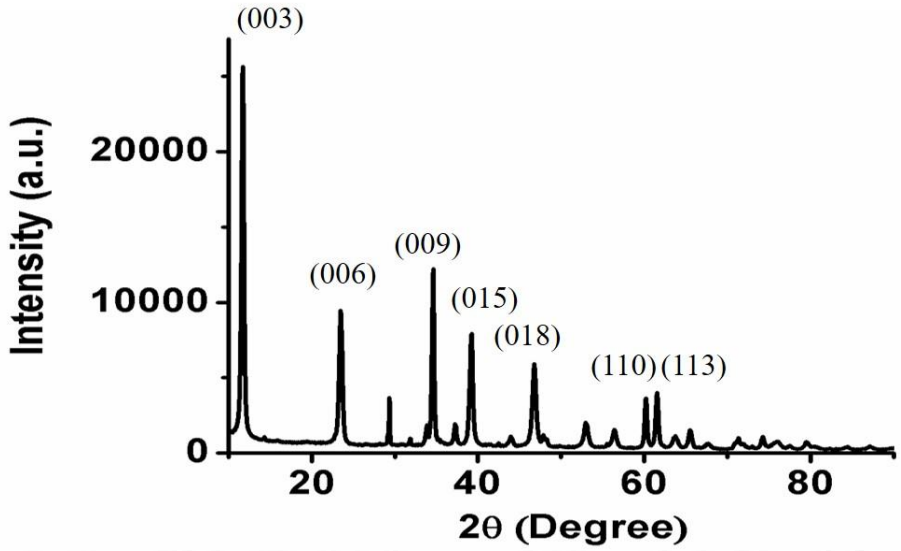

Figure 4.2: XRD pattern of Zn-Al LDHs

4.1.2.3 Chemical group identification using FT-IR spectroscopy

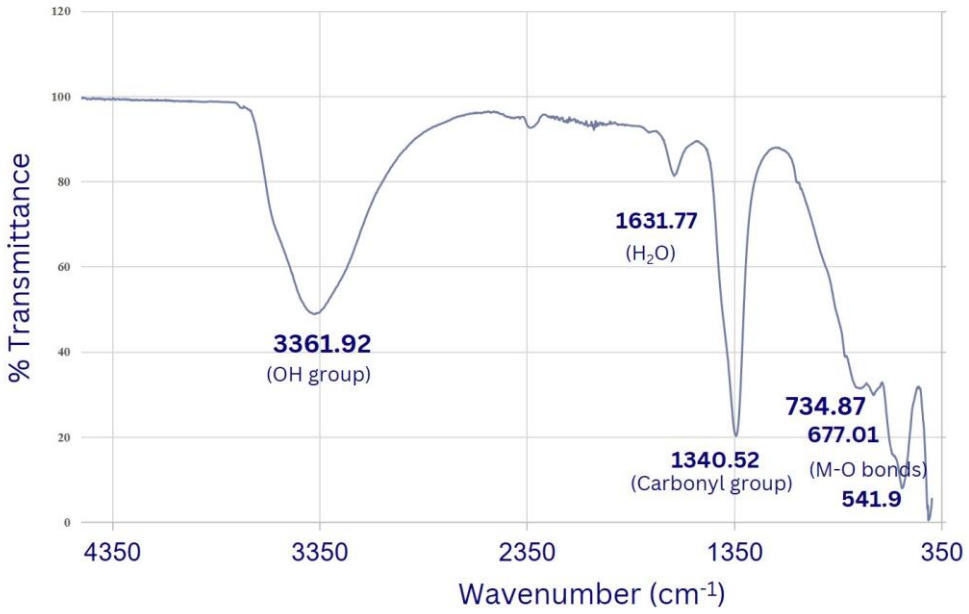

Figure 4.3: FT-IR spectra of Zn-Al LDHs

FT-IR spectroscopic study was done to find the functional groups in the synthesized LDHs (Figure 4.3). The spectra showed a broad peak at 3361.92 cm^{-1} corresponding to OH group of hydroxyl and water molecules. A sharp peak at 1340.52 cm^{-1} was also observed, matching to carbonyl group. Small peak was detected at 1631.77 cm^{-1} agreeing with presence of water molecules at the interlayers. The fingerprint region of the spectra showed peaks at 734.87 cm^{-1}, 677.01 cm^{-1} and 541.9 cm^{-1} conforming metal-oxygen bonds.

4.1.2.4 Chemical group identification using Raman spectroscopy

Raman spectra of Zn-Al LDHs showed a peak at 3471 re.1/cm corresponding to carbonate-water bridging bond. The peak depicting absorbed carbonate at the interlayers was found around 2885 re.1/cm. The characteristic peaks of carbonate were found at 1388 and 1052 re.1/cm. The bands for metal-oxygen bonds were seen at 555, 495 and 152 re.1/cm. The Raman spectrum obtained for Zn-Al LDHs is given in Figure 4.4.

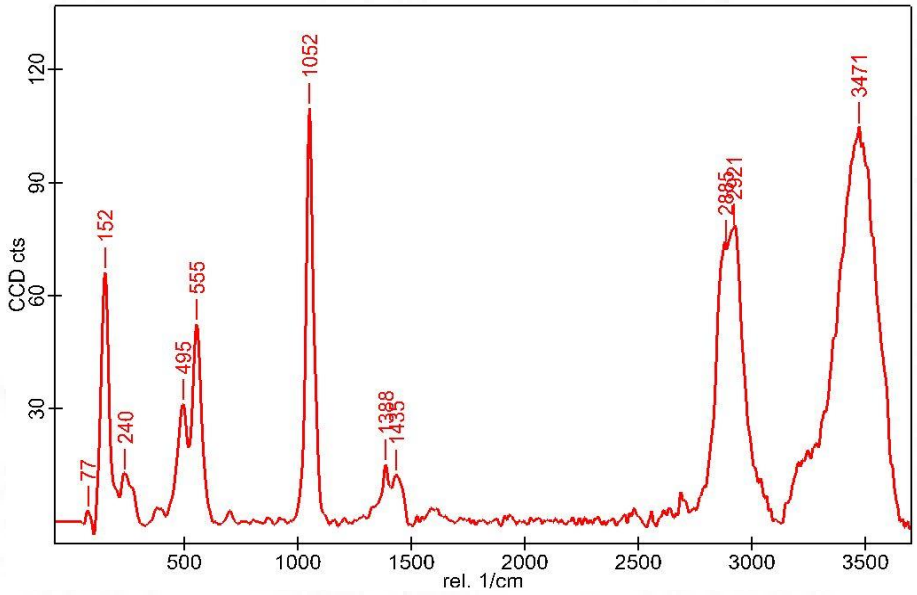

Figure 4.4: Raman spectra of Zn-Al LDHs

4.1.2.5 Thermal degradation profiling using TGA

Thermal degradation profiling of Zn-Al LDHs was done by TGA analysis. The TGA graph showed four major weight losses of 4 %, 17.3 %, 5.58 % and 4.49 % at 108^0 C, 255^0 C, 375^0 C and 563^0 C. The loss at 108^0 C corresponds to elimination of adsorbed water molecules while the 17.7 % loss at 255^0 C matches to dehydration of the layers. The elimination of carbonate ions and formation of mixed metal oxide were observed in the spectra at 375^0 C and 563^0 C. Figure 4.5 gives the thermal degradation profile of Zn-Al LDHs as per TGA analysis.

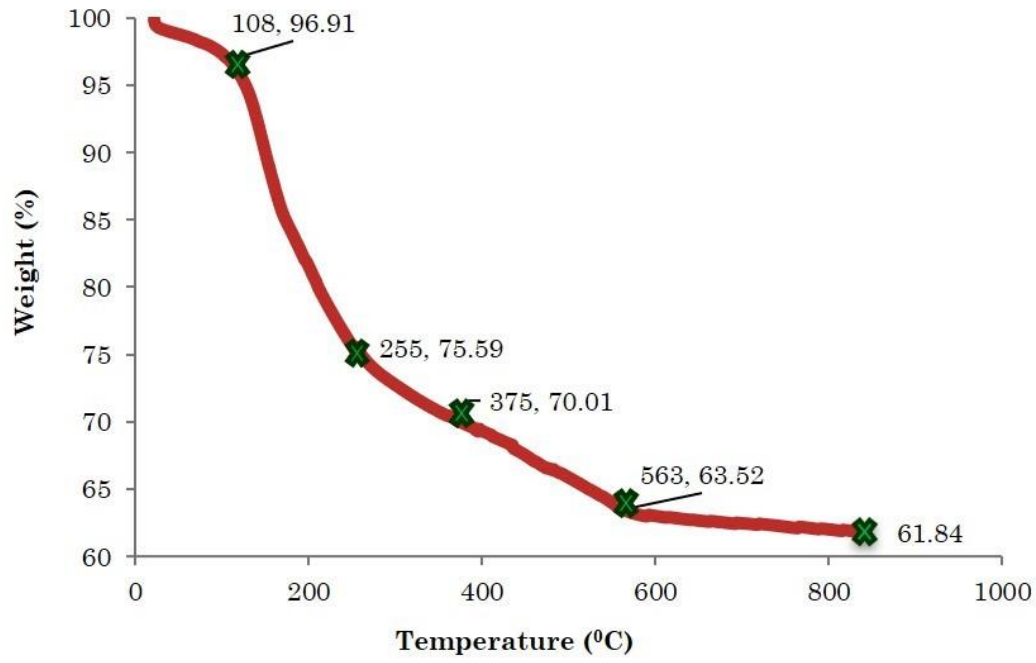

Figure 4.5: TGA graph of Zn-Al LDHs

4.1.2.6 Thermal stability check using DTA

Thermal degradation of Zn-Al LDHs was further evaluated with the help of DTA analysis. DTA analysis showed continued dehydration and dehydroxylation of layers

at 165 ^{0}C and 250 ^{0}C. The elimination of interlayer carbonate ions was observed in DTA curve between 250^0 C and 350 ^{0}C. The pattern beyond 312 ^{0}C showed a fall corresponding to collapse of the LDHs layered structure. Figure 4.6 shows the DTA curve pattern observed for Zn-Al LDHs.

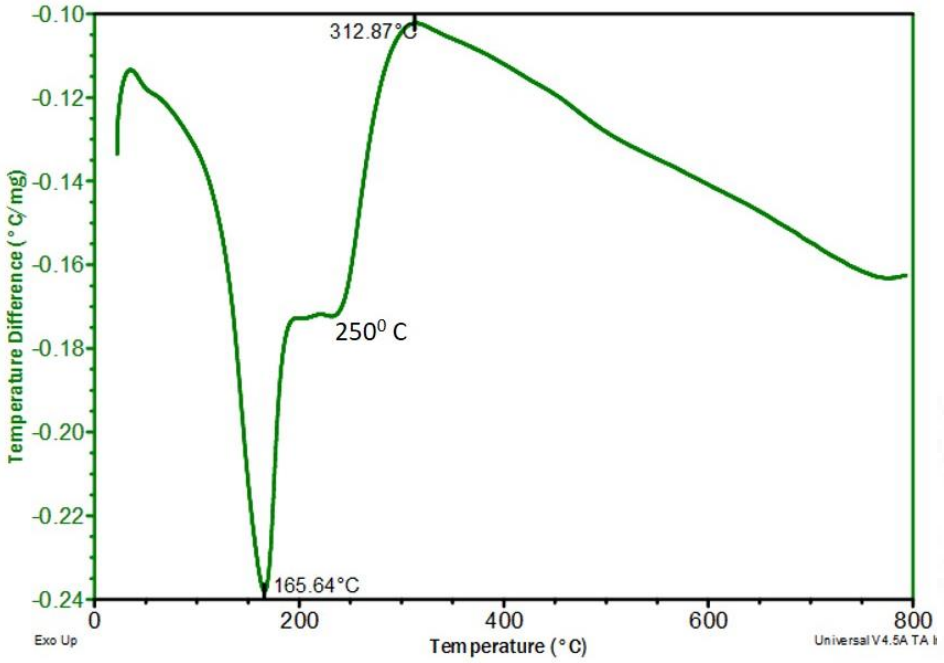

Figure 4.6: DTA analysis of Zn-Al LDHs

4.1.2.7 Hydrodynamic size analysis using DLS

The hydrodynamic size of Zn-Al LDHs in ethanol found to be 136.2 nm (Figure 4.7a). The size distribution was monomodal and the polydispersity index was 0.352 in ethanol. The hydrodynamic size obtained for Zn-Al LDHs dispersed in DMEM culture media was found to be 102 nm with a polydispersity index of 0.421 (Figure 4.7 b). Figure 4.7 includes the graphs showing results of the DLS analysis done for Zn-Al LDHs.

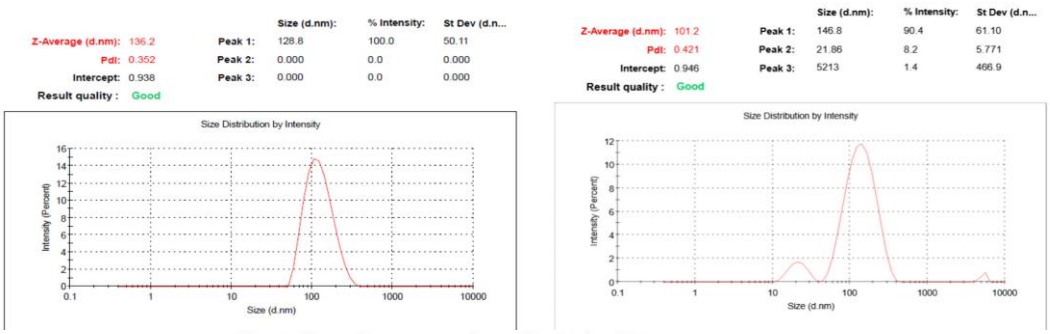

Figure 4.7: DLS analysis of Zn-Al LDHs in a) ethanol and b) DMEM culture media.

4.1.2.8 Charge confirmation using Zeta potential analysis

The charge estimation of Zn-Al LDHs gave a net positive value. Zeta potential analysis showed the charge to be +24.3 ± 3.47 mV. Figure 4.8 shows the zeta potential graph obtained for Zn-Al LDHs.

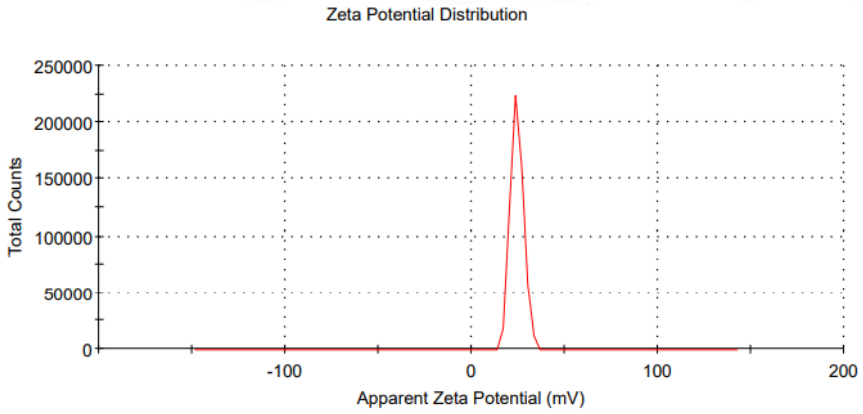

Figure 4.8: Zeta potential of Zn-Al LDHs

4.2 Evaluation of cellular interactions of 2D Zn-Al LDHs

4.2.1 Evaluation of cellular interactions of 2D Zn-Al LDHs with L929 cells

4.2.1.1 Cellular uptake of 2D Zn-Al LDHs by L929 cells

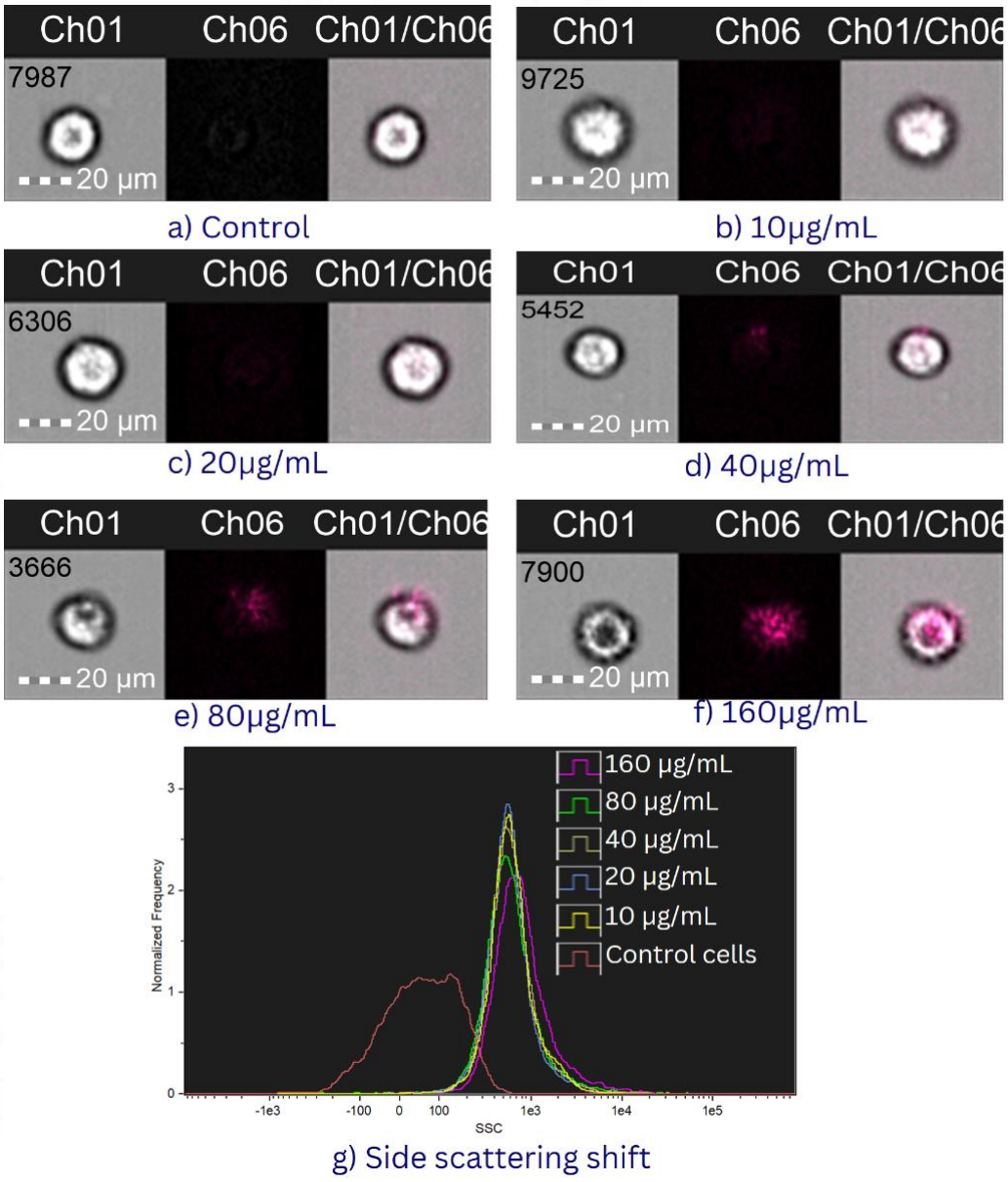

Figure 4.9: Flow cytometry analysis for cellular uptake of Zn-Al LDHs by L929 cells. a) control (untreated), (b) 10µg/mL, (c) 20µg/mL, (d) 40µg/mL (e) 80µg/mL, (f)

160µg/mL of Zn-Al LDHs, Chanel 06 represents side scattering (g) Graph showing shift in side scattering. Scale bar: 20 µm.

The uptake of Zn-Al LDHs in L929 cells was examined using flow cytometry analysis. From the flow cytometry data, channel 6 showed side scattering. The cells exposed to Zn-Al LDHs showed increased side scattering shift compared to control L929 cells (Figure 4.9 a-f). Among the different treated groups, the cells exposed to highest concentration of Zn-Al LDHs showed the highest shift in side scattering (Figure 4.9g). The increased cellular uptake with increment in exposure dose was reflected in the increased shift in side scattering (Figure 4.9g). The results are summarized in Figure 4.9.

4.2.1.2 Cellular metabolic activity check using MTT assay

MTT assay was used to calorimetrically quantify the metabolic activity post-exposure to Zn-Al LDHs. No effect in the metabolic activity was observed in L929 cells when treated with Zn-Al LDHs for 6 h compared to the untreated cells (Figure 4.10). The cell viability showed minor decrease with increasing concentrations of Zn-Al LDHs for exposure times 24 h and 48 h. The total viability in the highest concentration (160 µg/ml) exposed cells was 95.75 ± 0.06 % and 81.22 ± 0.08 % for 24 h and 48 h respectively. The corresponding viable cell % in treated cells after 48 h with respect to negative control were 97.13 ± 0.05 % (10 µg/ml), 96.21± 0.03 % (20 µg/ml), 95.77 ± 0.13 % (40 µg/ml), 96.96 ± 0.03 (80 µg/ml) and 81.22 ± 0.08 % (160 µg/ml) respectively.

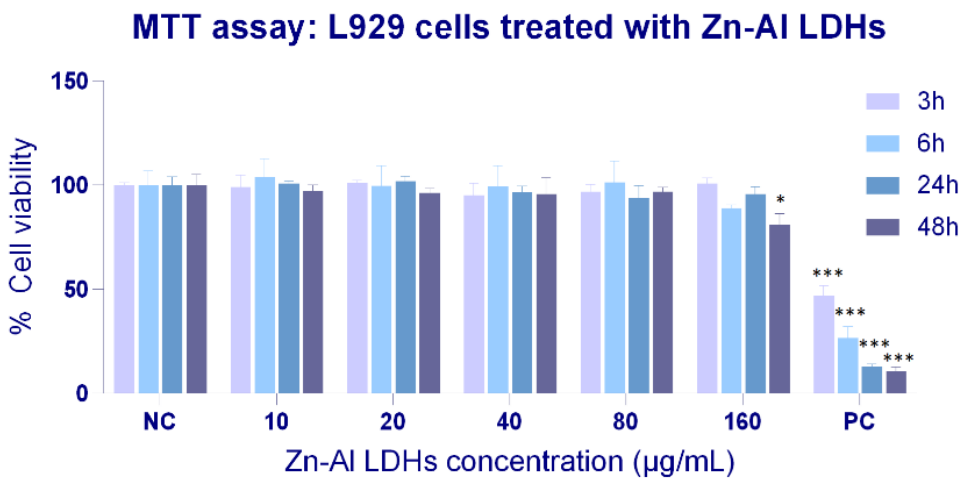

Figure 4.10: MTT assay on L929 cells treated with different concentrations of Zn-Al LDHs (10 µg/mL, 20 µg/mL, 40 µg/mL, 80 µg/mL and 160 µg/mL) to estimate the mitochondrial activity: NC represents negative control: untreated cells and PC stands for positive control: L929 cells exposed to phenol. *p<0.05, **p<0.01, ***p<0.001

4.2.1.3 Cell viability assessment using Live/dead assay

The viable and dead cells were marked with calcein-AM and PI staining respectively. The fluorescence imaging under green and red filters showed green-stained adherent L929 cells with about 80 % confluency (Figure 4.11). The cells showed calcein stained L929 cells in all Zn-Al LDHs exposure concentrations and no visible changes from the control cells were noted. The predominant calcein stained population was observed even at the highest Zn-Al LDHs exposure concentration and dead cell proportion was very low compared to viable cells.

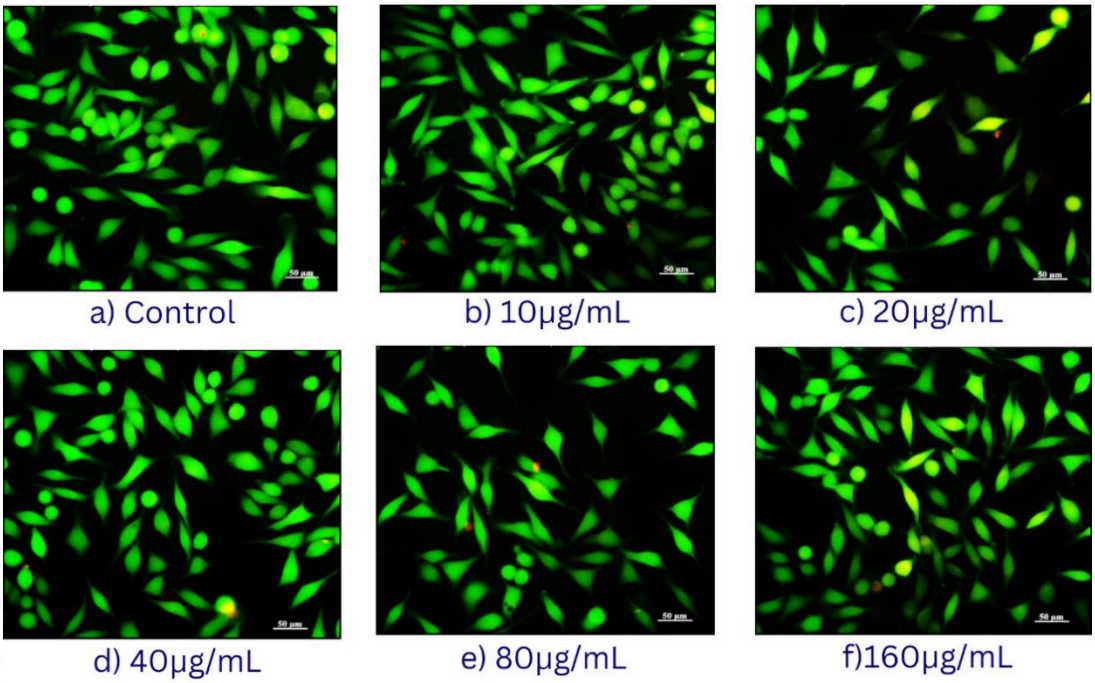

Figure 4.11: Live/dead assay of L929 cells exposed to Zn-Al LDHs using Calcein AM -PI staining. a) control (untreated), (b) 10µg/mL, (c) 20µg/mL, (d) 40µg/mL, (e) 80µg/mL and (f) 160 µg/mL of Zn-Al LDHs. Magnification: 20x.

4.2.1.4 Lysosomal activity evaluation using NRU

The lysosomal activity of LDHs was found to be uncompromised with 3 h, 6 h, 24 h and 48 h exposure of Zn-Al LDHs (Figure 4.12a). Even for the highest selected dose (160 µg/ml) and exposure time (48 h), the cell viability of L929 cells was 80 ± 0.09%. When L929 cells were exposed to 160 µg/ml of Zn-Al LDHs for 3 h, 6h, 24 h, the live-cell populations were 94.77 ± 0.94, 94.54 ± and 84.48 ± 0.09%. The microscopic imaging of L929 cells treated with Zn-Al LDHs for 24 h showed neutral red uptake by the lysosomes (Figure 4.12b-h). Images displayed healthy lysosomes in all the seeded wells.

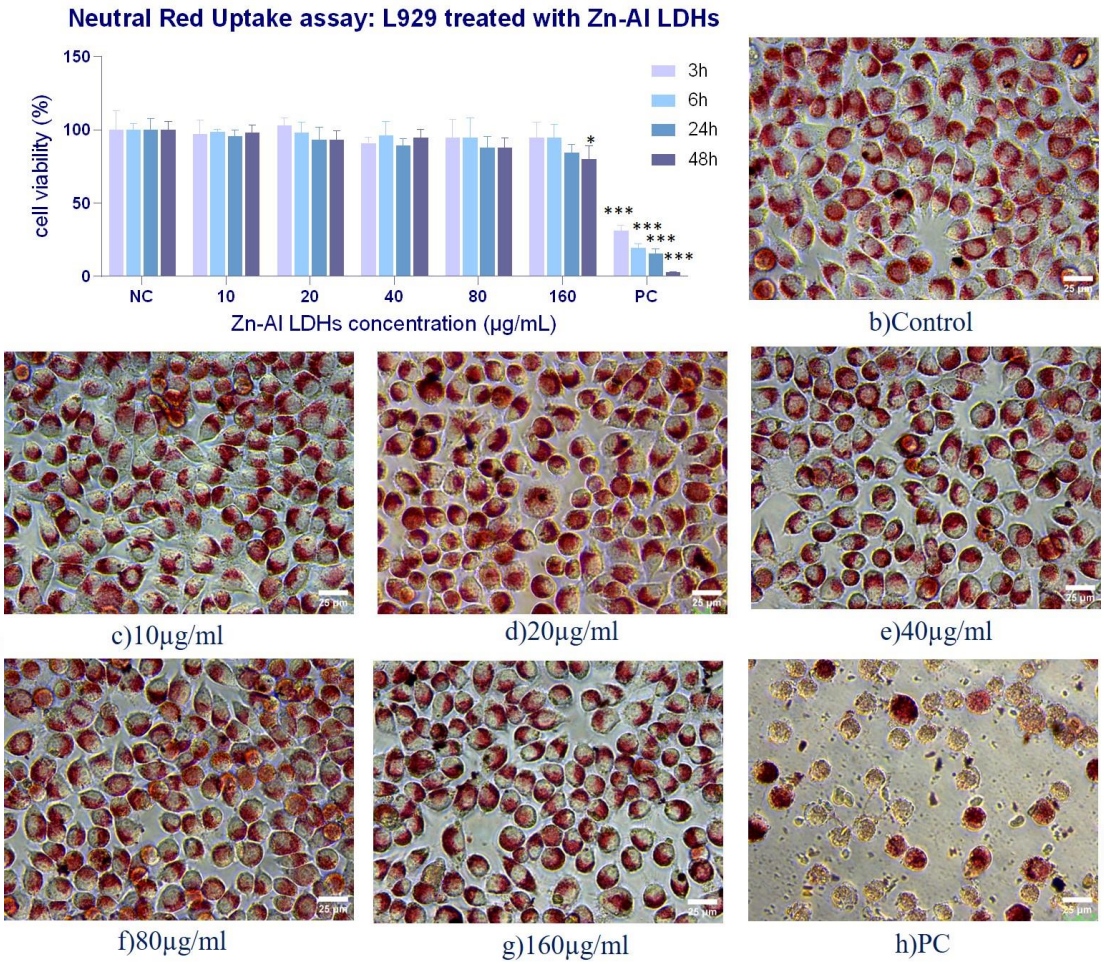

Figure 4.12: a) NRU assay on L929 cells treated with various doses of Zn-Al LDHs (10 µg/mL, 20 µg/mL, 40 µg/mL, 80 µg/mL and 160 µg/mL for different exposure time: Images of L929 cells (b) control cells, treated for 24 h with chosen concentrations, (c) 10µg/mL, (d) 20µg/mL, (e) 40µg/mL, (f) 80µg/mL and (g) 160 µg/mL of Zn-Al LDHs (h) PC (positive control cells). Magnification: 20x. Control (C) represents negative control: untreated cells. L929 cells exposed to phenol were kept as positive control. *p<0.05, **p<0.01, ***p<0.001

4.2.1.5 Lysosomal integrity assessment using AO staining

The L929 cells exhibited bright red and green fluorescence when stained with AO dye. The lysosomes were seen as localized red spots in all the test concentrations (10 – 160

µg/ml) and were comparable to the normal cells. Neither lysosomal enlargement nor visible reduction in red fluorescence was detected in the exposed cells for the increasing doses of Zn-Al LDHs upto 160 µg/ml. The fluorescence microscope images of AO staining are given in figure 4.13.

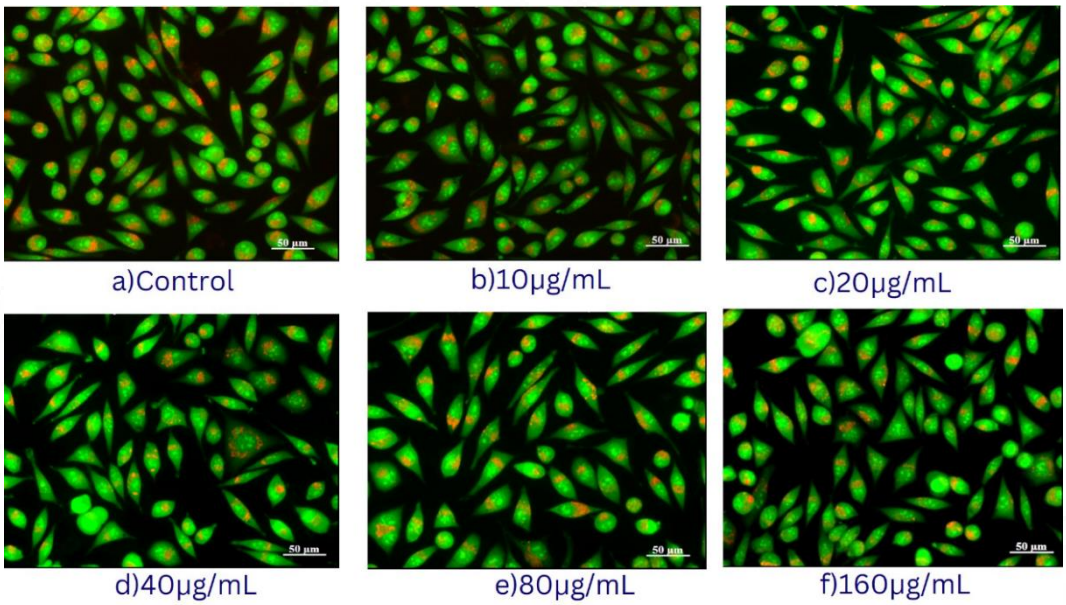

Figure 4.13: Acridine orange staining of L929 cells exposed to Zn-Al LDHs. a) control (untreated), (b) 10µg/mL, (c) 20µg/mL, (d) 40µg/mL, (e) 80µg/mL, (f) 160 µg/mL of Zn-Al LDHs. Magnification: 20x.

4.2.1.6 Oxidative stress assessment using DCFH-DA assay

The fluorescent plate reader detected no significant ROS release in exposed L929 cells compared to control untreated cells under the checked conditions. The RFU values for the highest dose exposed cells was 18283.3±533 against control cell value of 17182.67±660. The positive control cells marked an ROS production of 33357±3901.5. The graphical plot of the DCFH-DA results is given in Figure 4.14.

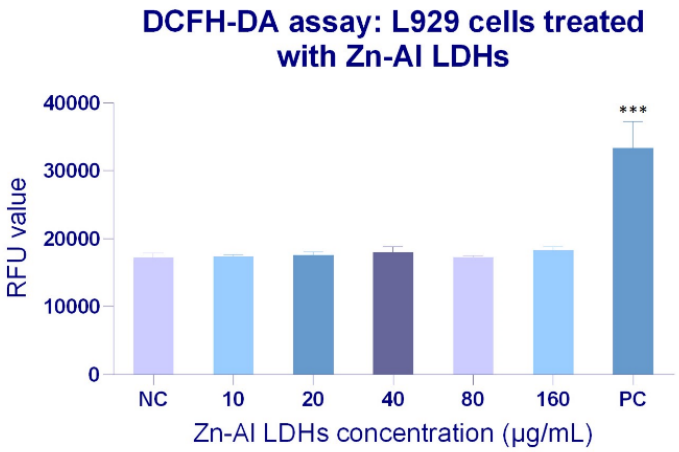

Figure 4.14: DCFH-DA assay on L929 cells treated with different concentrations of Zn-Al LDHs (10 µg/mL, 20 µg/mL, 40 µg/mL, 80 µg/mL and 160 µg/mL) to evaluate oxidative stress. NC represents control: untreated cells and PC stands for positive control: L929 cells exposed to phenol. **p<0.01.

4.2.1.7 Cytoskeletal and nuclear integrity screening using Rhodamine-phalloidin-DAPI staining

The actin filaments and nuclei were labeled using rhodamine-phalloidin and DAPI dual staining. The fluorescence imaging showed actin fibers as bright red and nuclei were stained blue. The fluorescence intensity was not faded in any of the treatment groups. The actin filaments in Zn-Al LDHs exposed cells were stable, organized and without any visible changes/ depolymerization from the control cell cytoskeleton. Nuclear condensation was not detectable in L929 cells treated with chosen doses of Zn-Al LDHs. The L929 cells showed regular cytoskeletal and nuclei in normal cells as well in LDHs exposed cells. The Figure 4.15 includes the cytoskeleton-nuclei counter-stained fluorescent images.

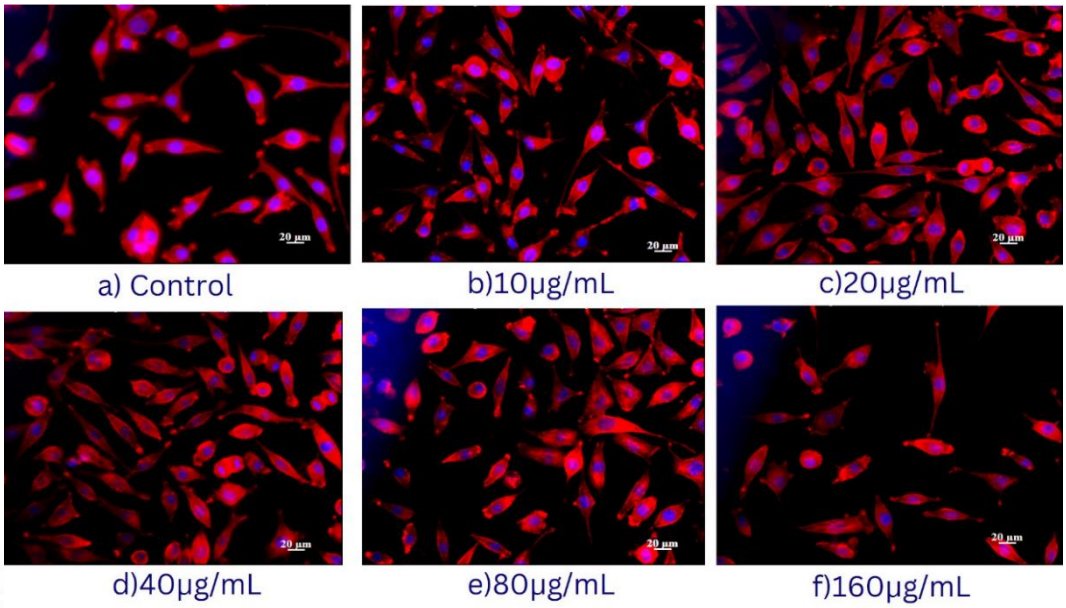

Figure 4.15: Rhodamine phalloidin staining of L929 cells exposed to Zn-Al LDHs. a) control (untreated), (b) 10µg/mL, (c) 20µg/mL, (d) 40µg/mL, (e) 80µg/mL, (f) 160 µg/mL of Zn-Al LDHs. Magnification: 20x.

4.2.1.8 Nuclear integrity and apoptosis estimation using DNA laddering

The gel doc image obtained after electrophoresis showed no DNA fragmentation in control as well as in treatment groups. The gel photograph after the DNA laddering assay is included as Figure 4.16. Lane 1 shows DNA fragments of 1 kb ladder and was used to identify the band's molecular weight. Lane 2 loaded with isolated DNA from the negative (unexposed) control group showed no fragmentation. Lanes 3 to 7 were loaded with DNA from L929 cells exposed to 10 µg/ml, 20 µg/ml, 40 µg/ml, 80 µg/ml and 160 µg/ml dose of Zn-Al LDHs. Lanes 3-7 showed only a single band without any fragmentation. Smearing was also absent in any of the treatment group loaded wells. Overall laddering pattern of test groups was comparable to that of control well. Fragmented bands appeared in lane 8 which was loaded with positive control.

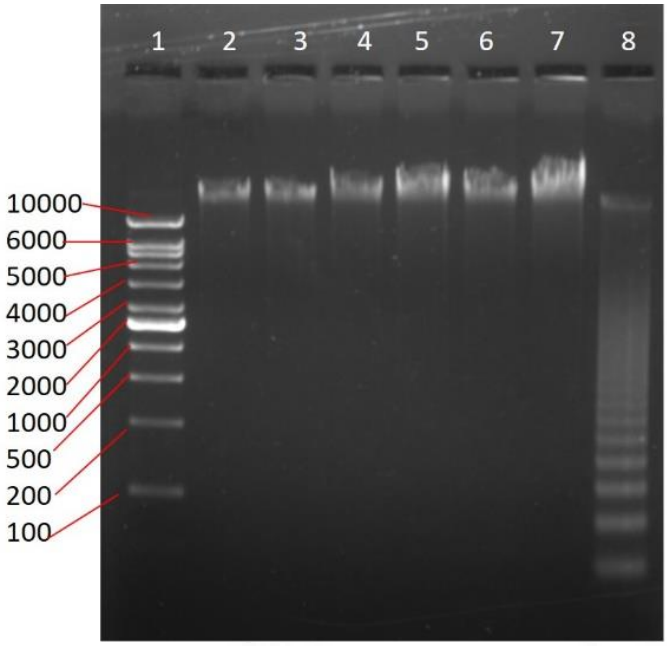

Figure 4.16**:** DNA laddering assay with L929 cells exposed to Zn-Al LDHs. Lanes 1 to 8 represents 1) DNA ladder, 2) Negative Control, 3) 10µg/mL, 4) 20µg/mL, 5) 40µg/mL, 6) 80µg/mL, 7) 160µg/mL of Zn-Al LDHs, 8) Positive control (GenElute Mammalian Genomic DNA Miniprep Kit Sigma Aldrich.

4.2.1.9Apoptosis/ Necrosis detection by Annexin-PI flow cytometry analysis

Annexin-PI labeling of LDHs exposed cells was done so as to check on potential cell death induction and to identify the mechanism of action as either via apoptosis or necrosis. The flow cytometry results are included in figure 4.17. The grating results showed an increase in the Annexin-positive cell population (quadrant 2). The cell population in early apoptosis stage increased from 1.71 % in control cells to 13% in L929 cells exposed to 160 µg/ml dose of Zn-Al LDHs for 24 h. No significant increase in the % of necrotic cells was found in the flow cytometry analysis. The % of necrotic cells were 0.22 % (Control), 0.14 % (10 µg/mL), 0.12 % (20µg/mL), 0.21 % (40 µg/mL), 0.25 % (80 µg/mL) and 0.31 % (160 µg/mL) respectively. The % of apoptotic cells were as follows, 0.19 % (Control), 0.36 % (10 µg/mL), 0.38 % (20µg/mL), 0.36

% (40 µg/mL), 1.05 % (80 µg/mL) and 1.3 % (160 µg/mL) respectively.

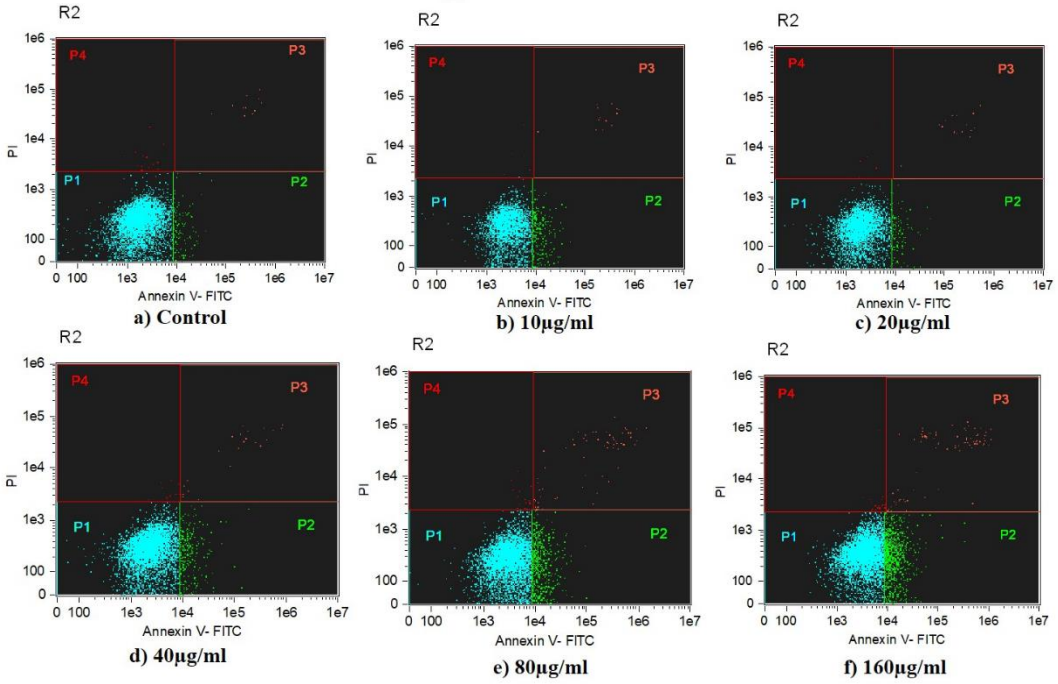

Figure 4.17**:** Flow cytometry: Apoptosis analysis of L929 cells treated with Zn-Al LDHs using flow cytometry. a) control (untreated), (b) 10µg/mL, (c) 20µg/mL, (d) 40µg/mL, (e) 80µg/mL, (f) 160µg/mL of Zn-Al LDHs.

4.2.1.10 Leachout toxicity

4.2.1.10.1 Metabolic activity assessment using MTT assay

The MTT assay results showed that L929 cells exposed to 24 and 72 h LDHs extraction did not induce any significant change in the metabolic activity of the cells, even though a dose-dependent decrease in cell viability was observed (Figure 4.18 a). The live-cell % for the cells exposed to 10 µg/ml dose of 24 h extract was 106± 0.02 while the same for 160 µg/ml dose was 81.93± 0.02. The 24 h positive control was marked with total cell viability of 33.69 ± 0.04 %. With the 72h extract, the % of cell viability was obtained as 83.03 ± 0.17 % for 160 µg/ml dose and 18.23 ± 0.01% for positive control cells.

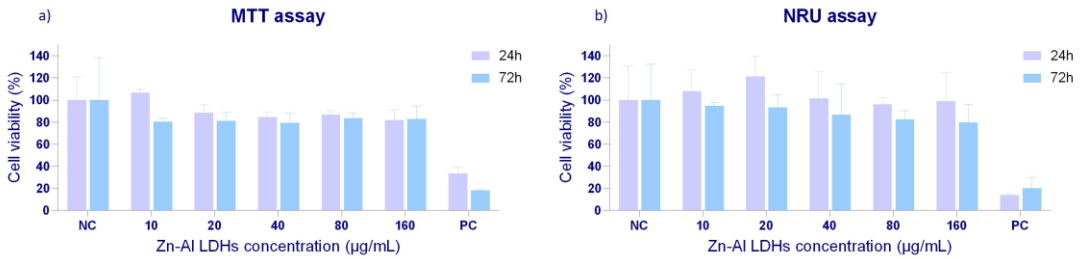

Figure 4.18: Leachout toxicity check on L929 cells treated with different concentrations of Zn-Al LDHs extracts (10 µg/mL, 20 µg/mL, 40 µg/mL, 80 µg/mL and 160 µg/mL). NC and C represents negative control: untreated cells and PC stands for positive control. a) MTT assay, b) NRU assay. Phenol exposed cells were kept as positive control for MTT and NRU assay while H_2O_2 exposed cells were kept as positive control. **p<0.01, ***p<0.001

4.2.1.10.2 Lysosomal activity evaluation using NRU assay

No drastic differences in the lysosomal activity were observed in L929 cells exposed to Zn-Al LDHs extracts compared to untreated cells. The total viable cell % of L929 cells exposed to 160 µg/ml of Zn-Al LDHs extract (24 h) was 98.91 ± 0.33 and that of 72 h extract was 80 % (79.87 ± 0.33). Figure 4.18 b includes the effect of Zn-Al LDHs extract on L929 cells.

4.2.2 Evaluation of cellular interactions of 2D Zn-Al LDHs with HOS cells

4.2.2.1 Cellular viability and metabolic activity check by MTT assay

The mitochondrial activity of HOS cells did not show any drastic change in comparison to untreated cells for the opted test conditions (exposure 3 h, 24 h and 48 h). The cell viability % for 160 µg/ml concentration treated cells for 3 h, 24 h and 48 h were 98.5 ± 0.01, 87.1 ± 0.05 and 82.53 ± 0.05. The % of live L929 cells after exposure to phenol for 3 h, 24 h and 48 h were 80.38 ± 0.04, 22.31± 0.09 and 19.75 ± 0.03 % respectively. The MTT results were included in figure 4.19.

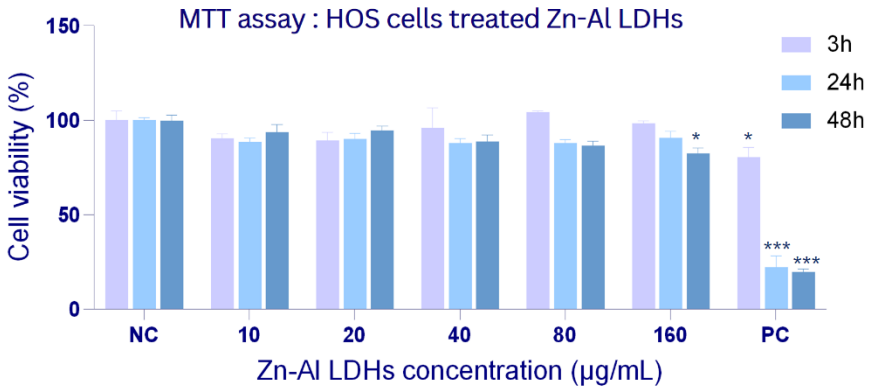

Figure 4.19: MTT assay on HOS cells treated with different concentrations of Zn-Al LDHs (10 µg/mL, 20 µg/mL, 40 µg/mL, 80 µg/mL and 160 µg/mL) to estimate the mitochondrial activity: NC represents negative control: untreated cells and PC stands for positive control: HOS cells exposed to phenol. *p<0.05, ***p<0.001

4.2.2.2 Cellular cytotoxicity examination using Live/dead assay

Live/dead assay was done by staining the seeded HOS cells with AO-EtBr fluorescent dyes (Figure 4.20). The live cells were stained green by AO and dead cells were stained red by EtBr. No evident shift from green to red fluorescence was detectable. The fluorescence photomicrographs showed an increase in EtBr-stained cells with an increase in Zn-Al LDHs exposure concentrations but where within non-cytotoxic limit. The overall viable cell population was high and the dead cell population was low compared to the total live cells.

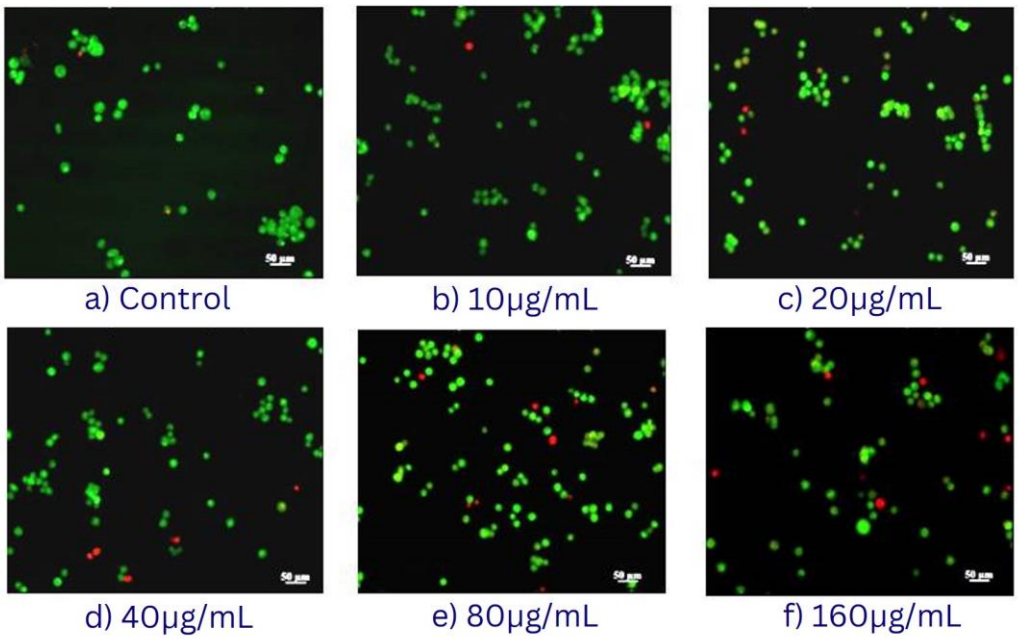

Figure 4.20: Live/dead assay using AO-EtBr staining of HOS cells treated with a) control (untreated), (b) 10µg/mL, (c) 20µg/mL, (d) 40µg/mL, (e) 80µg/mL, (f) 160 µg/mL of Zn-Al LDHs. The green signal indicates cells stained with Calcein AM and the red signal indicates cells stained by PI. Magnification: 20x

4.2.2.3 Mitochondrial membrane potential (MMP) by JC1 staining

The MMP in HOS cells were imaged using JC1 staining and are included in Figure 4.21. The photomicrographs showed healthy mitochondria in normal and treated cells. No visible changes in MMP or drastic drop in red fluorescence were found in HOS cells with extended doses of Zn-Al LDHs. Figure 4.21 shows the fluorescence microscope images of HOS cells stained with JC1 staining.

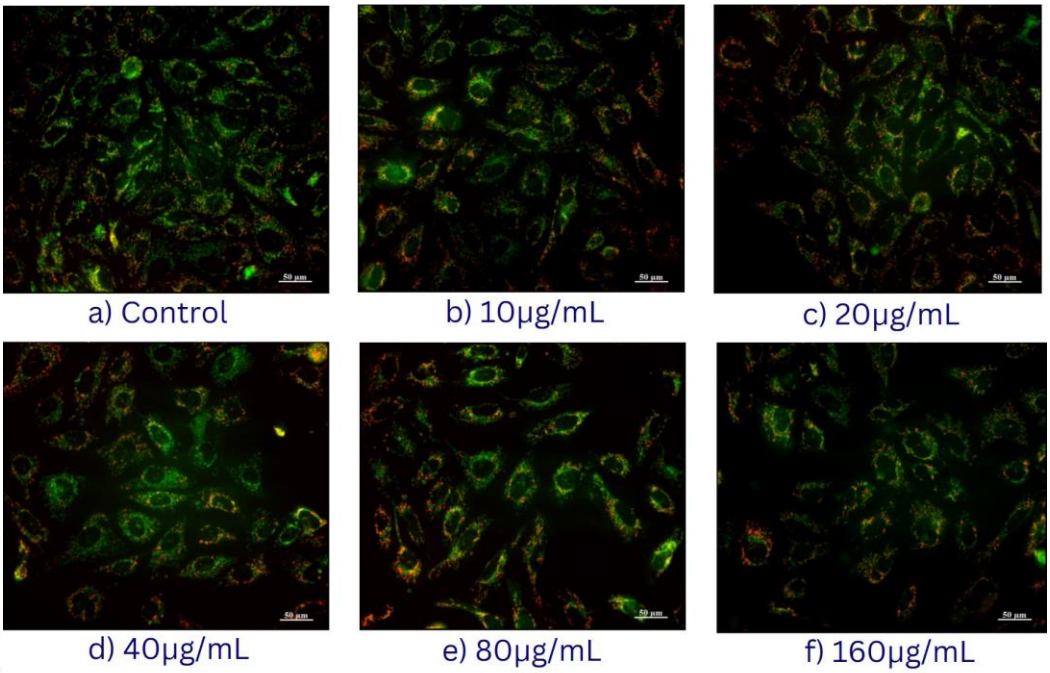

Figure 4.21: JC1 staining images of HOS cells after post-exposure to Zn-Al LDHs to analyze the MMP. a) control (untreated), (b) 10µg/mL, (c) 20µg/mL, (d) 40µg/mL, (e) 80µg/mL, (f) 160 µg/mL of Zn-Al LDHs. Magnification: 20x

4.2.2.4 Morphological analysis by Giemsa staining

Giemsa-stained HOS cells showed normal morphology in treated and untreated cells. The microscopic images of Giemsa-stained HOS cells are given in figure 4.22. The morphological integrity was not compromised in the Zn-Al LDHs exposed cells up to 160 µg/mL dose concentration for 24 h exposure. The micrographs showed absence of any cell shrinkage or breakage in HOS cells exposed to different concentrations of Zn-Al LDHs.

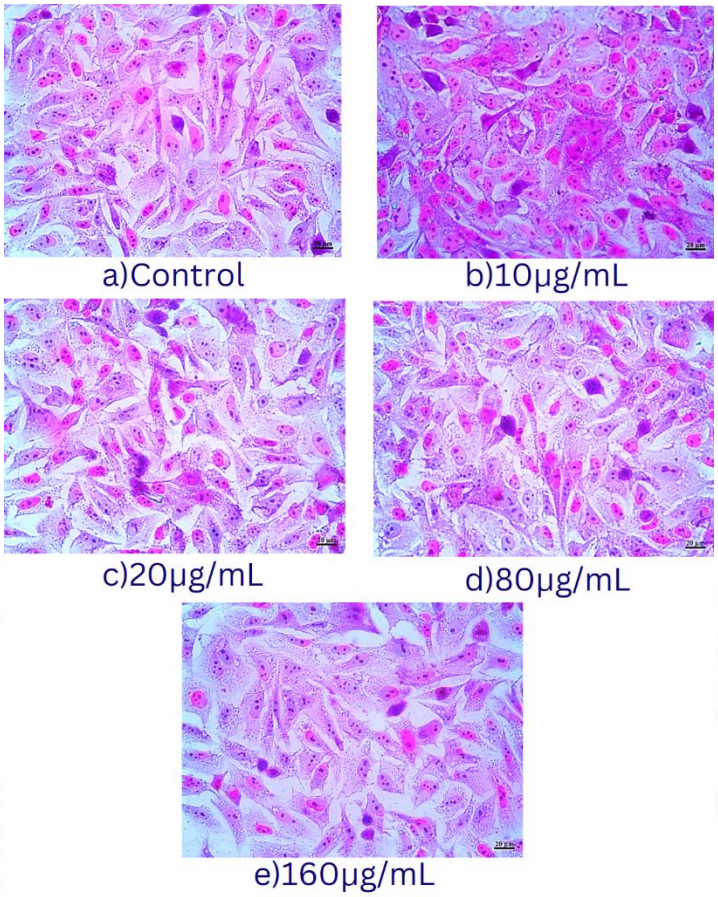

Figure 4.22: Morphology analysis using Giemsa staining of HOS cells exposed to Zn-Al LDHs. a) control (untreated), (b) 10µg/mL, (c) 20µg/mL, (d) 80µg/mL, (e) 160 µg/mL of Zn-Al LDHs. Magnification: 20x.

4.2.2.5 Morphological analysis by Coomassie brilliant blue staining

HOS cells were labelled with Coomassie brilliant blue stain and it was found that all the seeded cells including treated ones displayed regular morphological features. The compound microscope images of exposed cells showed regular osteoblast cell morphology for all dose concentrations. Figure 4.23 includes the images of Coomassie brilliant blue staining on HOS cells after Zn-Al LDHs exposure.

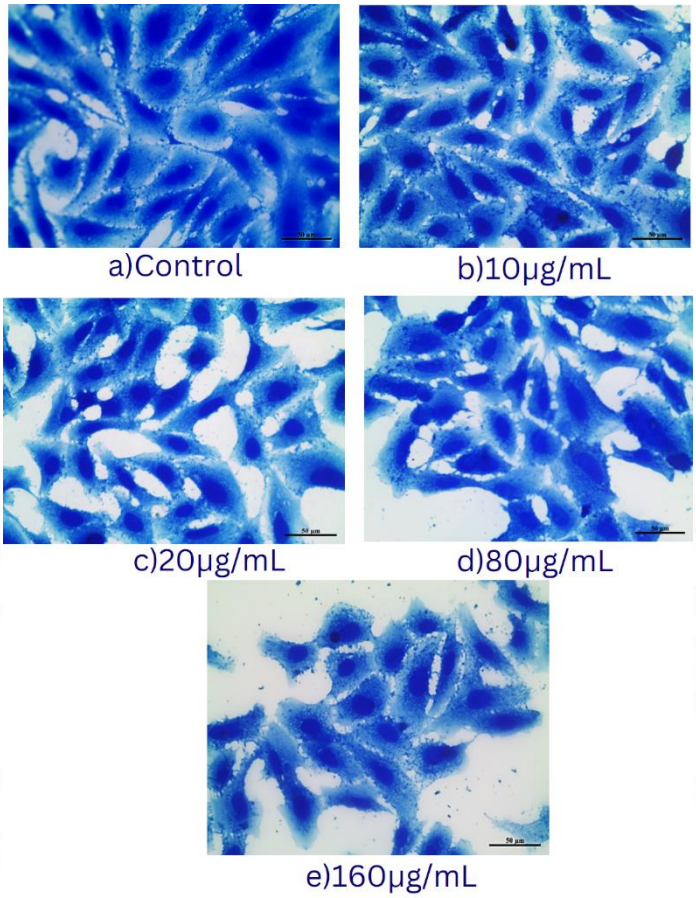

Figure 4.23: Coomassie brilliant blue staining of HOS cells exposed to Zn-Al LDHs. a) control (untreated), (b) 10µg/mL, (c) 20µg/mL, (d) 80µg/mL, (e) 160 µg/mL of Zn-Al LDHs. Magnification: 20x.

4.2.2.6 Oxidative stress assessment using DCFH-DA assay

The ROS generation in exposed cells with respect to the unexposed cells was expressed in RFU values (Figure 4.24). For the 3 h treatment, the treated cells and normal cells followed a similar pattern and no severe variation in RFU values was observed. The RFU for control (6 h) was 2377.33 ± 240.54 and the RFU value for the highest selected dose and positive control were 2558.67 ± 94.74 and 35406.33 ± 6287.99. In 24 h exposed cells, a dose-dependent increase in RFU value was observed but the variation was not significantly different from control. The RFU values

estimated in 24 h treatment was 1093 ± 85.46 (negative control cells), 1305 ± 138.88 (40 µg/ml exposed cells), 1738.67 ± 381.49 (160 µg/ml exposed cells) and 40627.33 ± 4820.35 (positive control cells). Also, in the case of 48 h exposure, not much elevation in RFU values was observed for the treatment groups, the RFU values were 3387.33 ± 1055.75 (negative control group), 3478.67 ± 661.58 (160 µg/ml exposed cells) and 39152 ± 4820.25 (positive control).

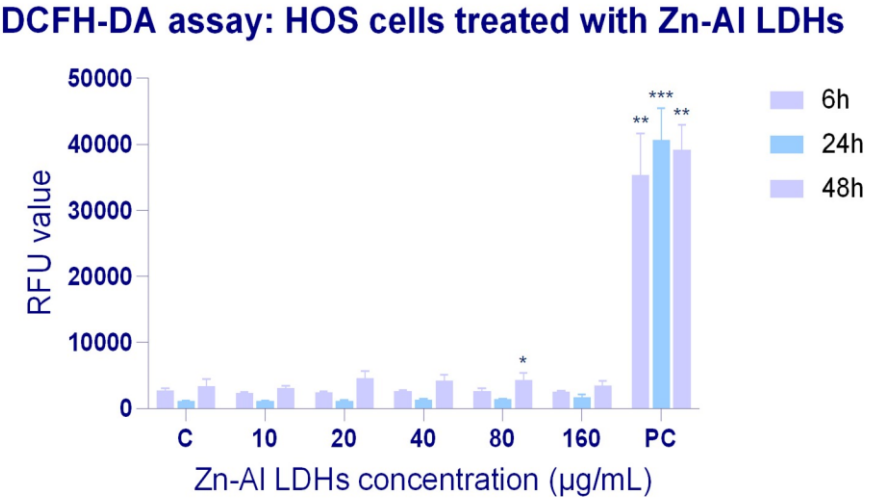

Figure 4.24: DCFH-DA assay on HOS cells treated with different concentrations of Zn-Al LDHs: 10 µg/mL, 20 µg/mL, 40 µg/mL, 80 µg/mL and 160 µg/mL. C represents negative control: untreated cells and PC stands for positive control: HOS cells exposed to H_2O_2. *p<0.05, ***p<0.001

4.2.2.7 Cell membrane damage check using lactate dehydrogenase enzyme assay

The lactate dehydrogenase enzyme release on exposure to Zn-Al LDHs was monitored and featured in figure 4.25. It was found that compared to the respective untreated control cells, the 6h exposure of Zn-Al LDHs did not trigger an increase in the enzyme release. Whereas in the case of 24h exposure, 9.77 ± 0.08 % and 13.12 ± 0.02 % increase in LDHs release was observed in 80 µg/ml and 160 µg/ml concentrations of exposed HOS cells.

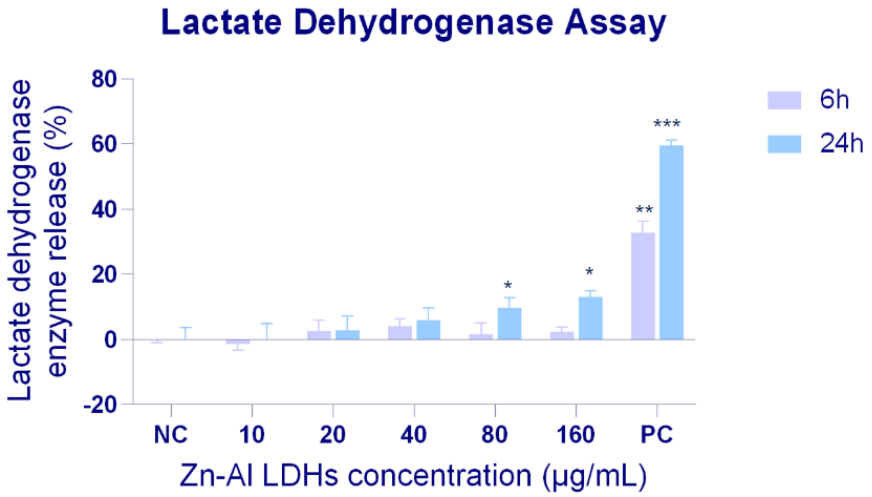

Figure 4.25: Lactate dehydrogenase activity in HOS cells exposed to different concentrations of Zn-Al LDHs: 10 µg/mL, 20 µg/mL, 40 µg/mL, 80 µg/mL and 160 µg/mL. NC represents negative control: untreated cells and PC stands for positive control: HOS cells exposed to H_2O_2. For *p<0.05, **p<0.01, ***p<0.001.

4.2.2.8 Lysosomal integrity assessment using Acridine orange staining

The effect of Zn-Al LDHs on the lysosomal integrity of HOS cells was examined using AO staining. As per the fluorescence images in figure 4.26, the lysosomes were seen as bright red fluorescent dots and no decrease in red fluorescence intensity in all the treatment groups: control, 10 µg/mL, 20 µg/mL, 40 µg/mL, 80 µg/mL and 160 µg/mL was observed.

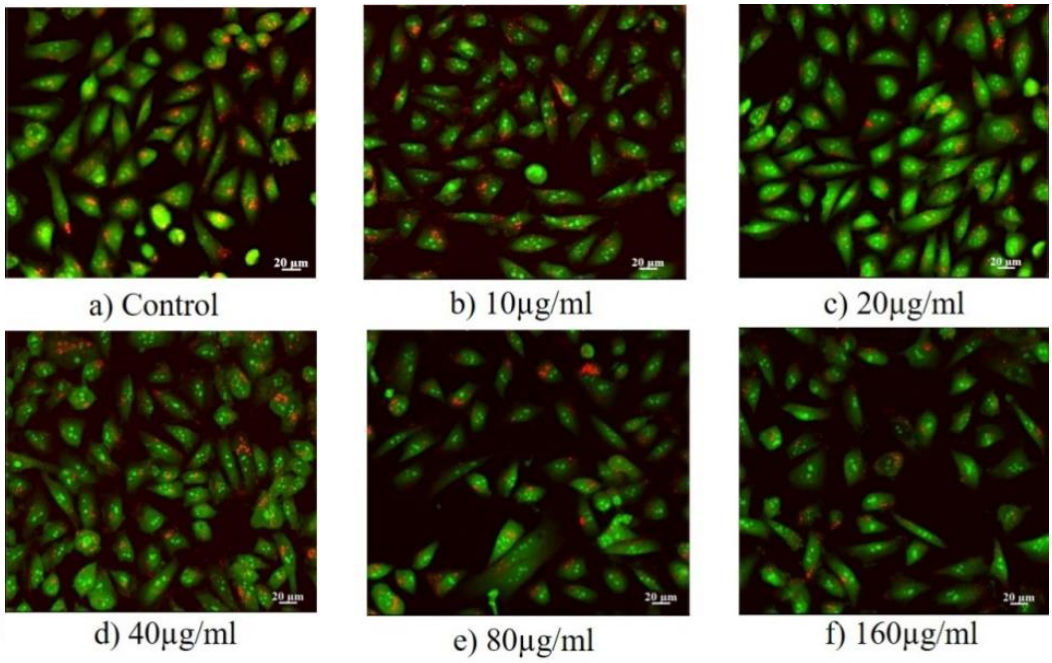

Figure 4.26**:** Acridine orange staining to assess the lysosomal integrity of HOS cells post-exposure to Zn-Al LDHs. a) control (untreated), (b) 10µg/mL, (c) 20µg/mL, (d) 40µg/mL, (e) 80µg/mL, (f) 160 µg/mL of Zn-Al LDHs. Magnification: 20x.

4.2.2.9 Cytoskeletal and nuclear integrity screening using Rhodamine-phalloidin-DAPI staining

Integrity of the cytoskeleton and nuclei of HOS cells post-exposure was examined by dual labeling with rhodamine-phalloidin-DAPI fluorescent dyes (Figure 4.27). The counterstained microscope had well-organized actin filaments stained bright fluorescent red and healthy nuclei stained blue. The HOS cells exposed to different concentrations of Zn-Al LDHs maintained the structural integrity of the cytoskeleton. The nuclei in all the treatment groups: normal, 10 µg/mL, 20 µg/mL, 40 µg/mL, 80 µg/mL and 160 µg/mL of Zn-Al LDHs showed no nuclei fragmentation or condensation.

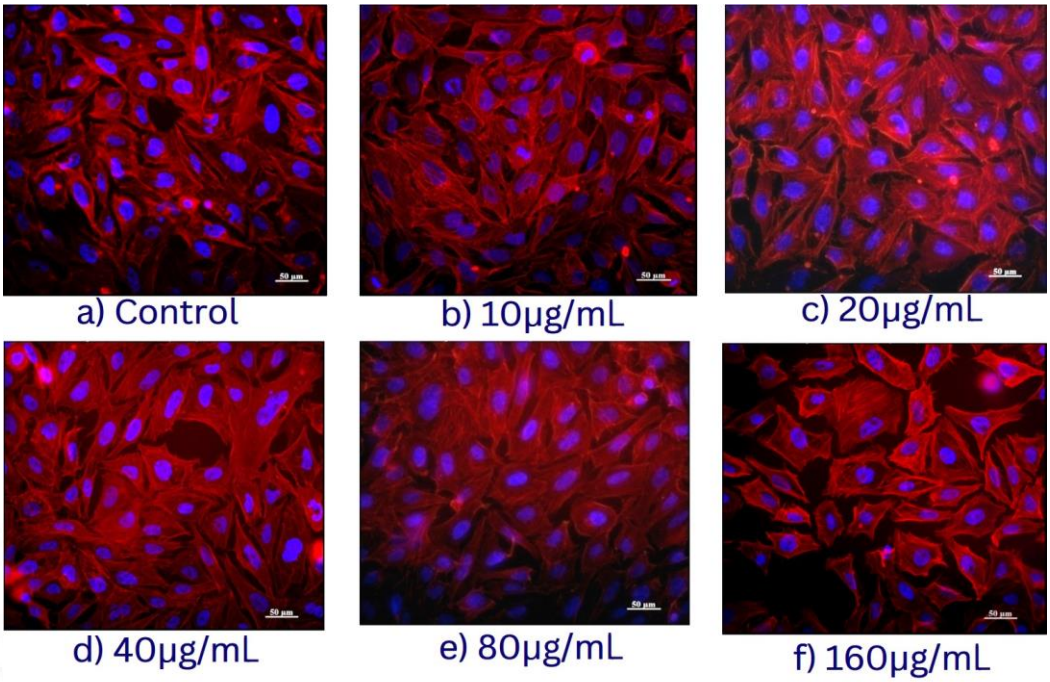

Figure 4.27: Rhodamine phalloidin- DAPI labeling of actin filaments and nuclei of HOS cells exposed to Zn-Al LDHs. a) control (untreated), (b) 10µg/mL, (c) 20µg/mL, (d) 40µg/mL, (e) 80µg/mL, (f) 160 µg/mL of Zn-Al LDHs. Magnification: 20x

4.2.2.10 Nuclear integrity and apoptosis estimation using DNA laddering

DNA laddering was done to check if Zn-Al LDHs exposure was capable of inducing DNA fragmentation, genotoxicity, or apoptosis. The Figure 4.28 shows the gel doc image of gel loaded with isolated DNA from normal cells (lane 2), 10 µg/mL (lane 3), 20 µg/mL (lane 4), 40 µg/mL (lane 5), 80 µg/mL (lane 6) and 160 µg/mL (lane 7) of Zn-Al LDHs. Lane 1 represents the DNA ladder, lane 9 stands for positive control and was kept for reference. From the gel doc image, it is evident that DNA fragmentation was absent in all treatment groups in which Zn-Al LDHs exposure was given.

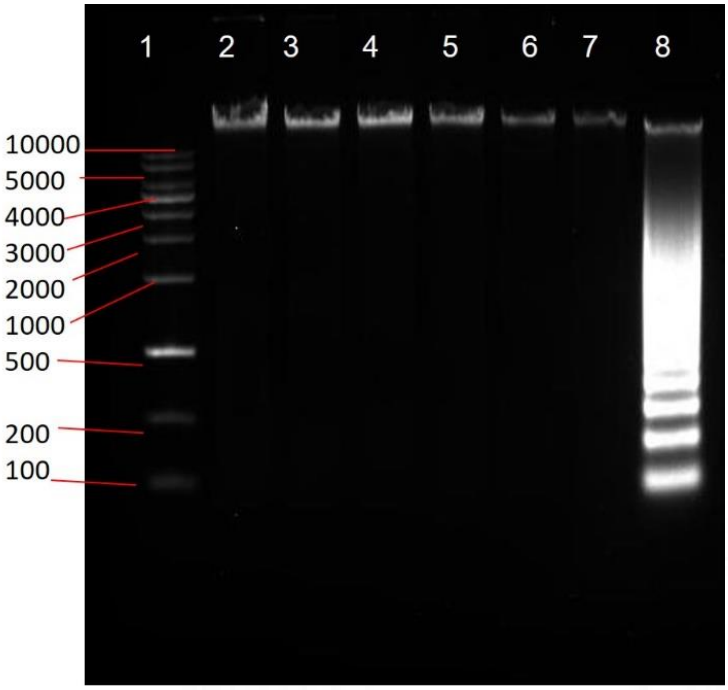

Figure 4.28: DNA ladder assay with HOS cells exposed to Zn-Al LDHs. Lanes 1 to 8 represents 1) DNA ladder, 2) Negative Control, 3) 10µg/mL, 4) 20µg/mL, 5) 40µg/mL, 6) 80µg/mL, 7) 160µg/mL of Zn-Al LDHs, 8) Positive control (GenElute Mammalian Genomic DNA Miniprep Kit Sigma Aldrich.

4.3 Toxicity evaluation of 2D Zn-Al layered double hydroxides in rat model

4.3.1 Clinical signs

The behaviour of the Wistar rats was evaluated for the entire study period (14 days). The indexes monitored were behavioural patterns like eating, drinking, grooming and cage movement, stimuli response, *etc.*, and also appearance/physical features like eyes, ears, nose, mouth and skin. The clinical signs considered were all normal throughout the time period and no abnormal behaviours were observed. The parameters overlooked and the results obtained are listed in Table 4.1.

SIGNS	GROUP I	GROUP II	GROUP III	GROUP IV
Eyes	N	N	N	N
Skin	N	N	N	N
Nose, ear, mouth	N	N	N	N
Eating	N	N	N	N
Drinking	N	N	N	N
Grooming	N	N	N	N
Stimuli response	N	N	N	N
Piloerection	N	N	N	N
Weight loss	A	A	A	A
Posture	N	N	N	N
Movements	N	N	N	N
Respiration	N	N	N	N

Table 4.1: Record of behavioural and clinical signs in Wistar rats after exposure to Zn-Al LDHs. N denotes for normal and A denotes absent.

4.3.2 Body weight

The body weight of Wistar rats in all the experimental groups showed normal increment in weight gain. No drastic weight loss was observed on exposure to Zn-Al LDHs. The recorded body weight was tabulated in Table 4.2.

GROUP NO	TREATMENT GROUP	BODY WEIGHT
I	Control	207.95 ± 24 g
II	3rd day	214.38± 68 g
III	7th day	229.02± 59 g
IV	14th day	234.27± 17 g

Table 4.2: The body weight of Wistar rats on the day of sacrifice after exposure to Zn-Al LDHs.

4.3.3 Hematology

Blood samples were collected from all four groups: control, 3rd day, 7th day and 14th day for hematological analysis. The checked indices which include platelet, RBC, WBC and HGB showed an initial slight decrease from the control group on 3rd and 7th day and then an increase on 14th day. The RBC count showed a significant increase on the 14th day (8.54 x 10^6/mm^3) and HGB showed a significant decrease on the 3rd day (13.2). Although fluctuations were observed, all the hematological parameters showed values within the normal reference r The obtained levels of hematological parameters were included in figure 4.29.

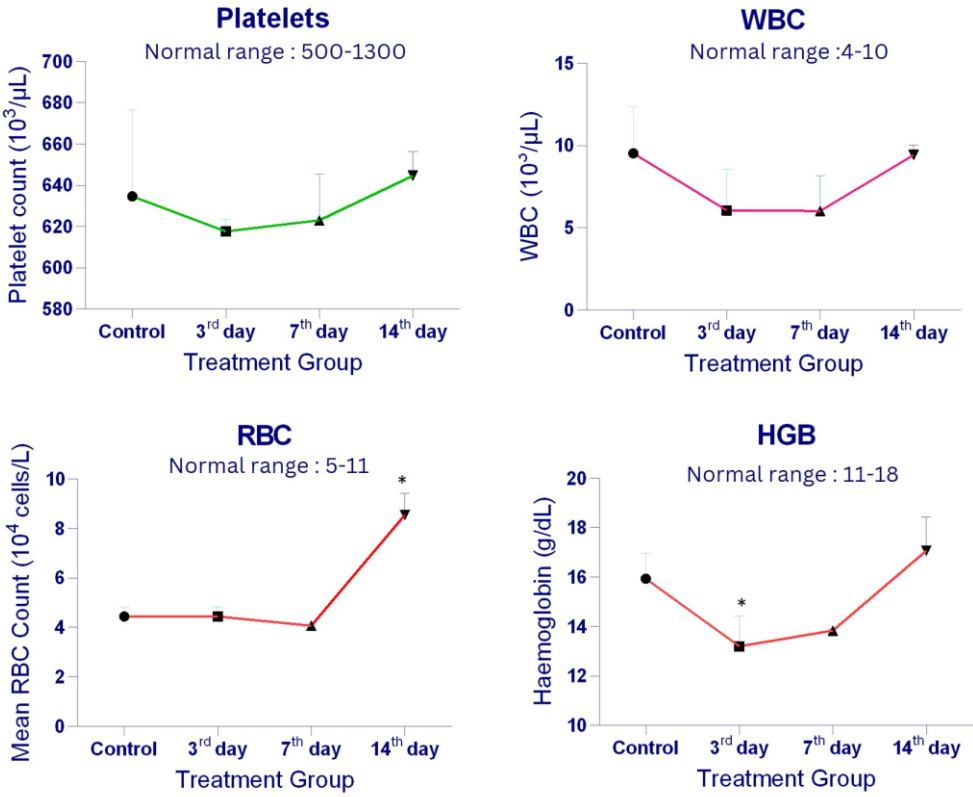

Figure 4.29: Hematology analysis (a) platelet count, (b) RBC count, (c) WBC and (d) HGB of blood samples collected from Zn-Al LDHs exposed Wistar rats. *p<0.05.

4.3.4 Biochemistry

Serum was obtained from the blood collected from the control and test group rats. Among the parameters analyzed, the levels of albumin, creatine and protein remained comparable to control after 3-, 7- and 14-day exposure. The albumin level was 4.87± 0.4 mg/dl, 4.13 ± 1.00 mg/dl, 5.1 ± 0.78 mg/dl and 5.37 ± 0.15 mg/dl on control rats, 3rd day, 7th day and 14th day (Figure 4.30 a). The protein levels of control group were 10.27 ± 1.00 mg/dl while that on 3rd day, 7th day and 14th day were 11.03 ± 1.34 mg/dl, 10.67± 1.39 mg/dl and 10.47± 0.47 mg/dl (Figure 4.30 b).. The amount of creatine (Figure 4.30 c). was found to be 0.99± 0.12 mg/dl (control), 0.96± 0.06 mg/dl (3rd day), 0.97± 0.02 mg/dl (7th day) and 0.99± 0.10 mg/dl (14th day). The cholesterol and

glucose levels showed deviation from the control group but remained within the normal range (Figure 4.30 d). In the case of cholesterol levels, the values were 154.6 mg/dl (control) compared to 73.3 mg/dl (3rd day), 72.66 mg/dl (7th day) and 148 mg/dl (14th day). The glucose level increased on 3rd day (67.05 mg/dl) and 7th day (71.65 ± 9.1 mg/dl) compared to control (55.25 ± 8.9 mg/dl). On the 14th day, the level of glucose was 49.7 ± 1.97 mg/dl (Figure 4.30 e). Fluctuations were also observed in the level of AST but the values were within the normal reference range (Figure 4.30 f). The ALP level showed a decrease on 3rd and 7th day, but higher level on 14th day compared to the ALP levels of control unexposed Wistar rats (Figure 4.30 g). The ALT levels were similar to control on 3rd and 7th day while an increase though insignificant was observed on the 14th day (Figure 4.30 h). The results obtained from the biochemistry analysis were graphically represented in figure 4.30.

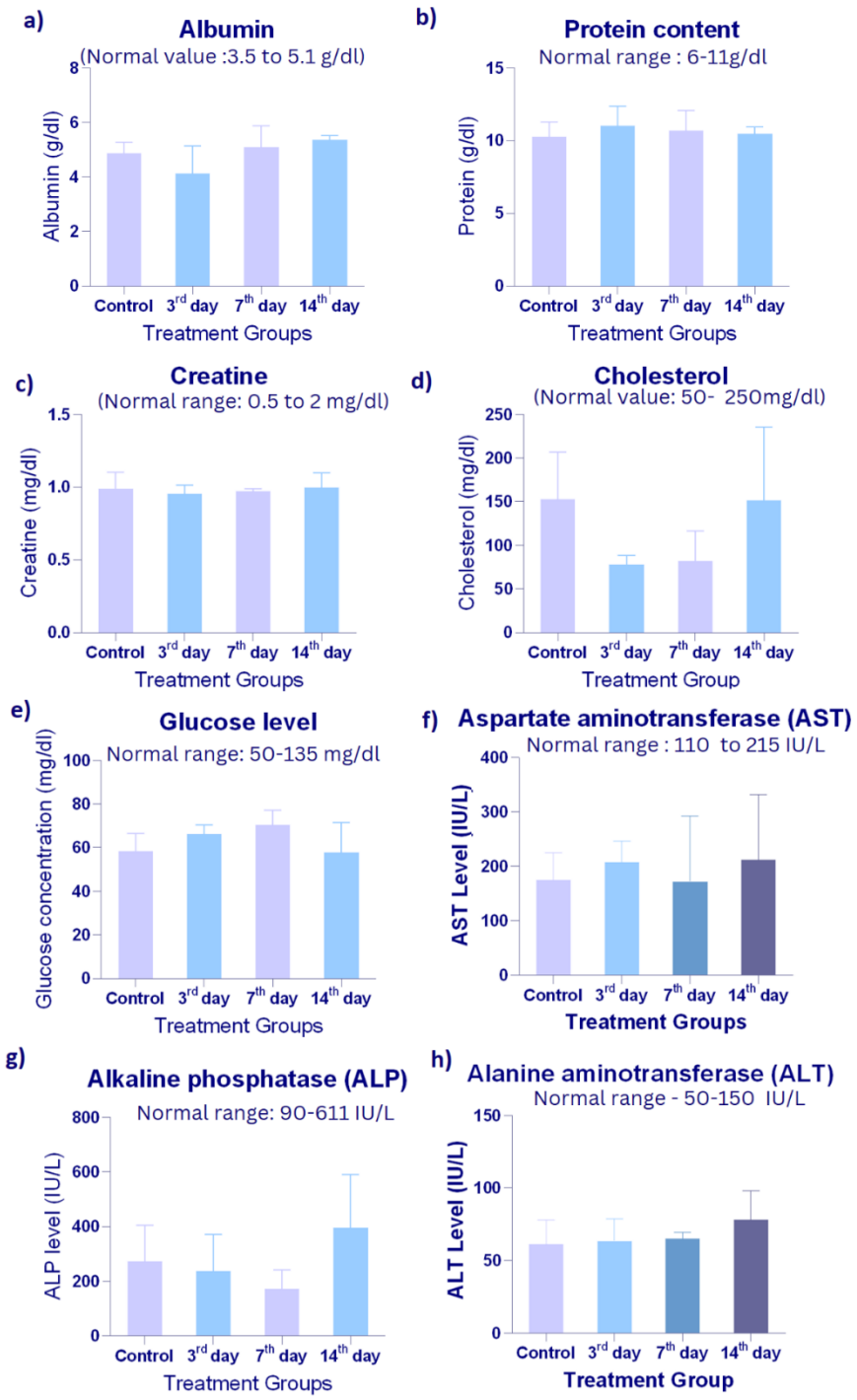

Figure 4.30: The biochemistry analysis of samples collected from Zn-Al LDHs exposed Wistar rats. Values were expressed in mean ± SD and n=3.

4.3.5 Urine analysis

Urine collected from the test animals on the 3rd, 7th and 14th day were analysed for different parameters. The urine analysis results were tabulated in Table 4.3. All the indices checked which includes pH, specific gravity, protein level, urobilinogen, ketones, glucose, leukocyte, nitrite, blood and bilirubin were comparable to the control animals.

PARAMETERS	CONTROL	3rd DAY	7th DAY	14th DAY
pH	7.88 ± 0.29	8.00 ± 0.0	7.00 ± 0.27	6.05 ± 0.35
Protein(mg/dl)	14.66± 1.53	14.00± 1.41	14.33± 1.15	14.11± 1.3
Urobilinogen(mg/dl)	0.1 ± 0.11	0.11 ± 0.33	0.11 ± 0.01	0.1 ± 0.1
Specific gravity	1.02 ± 0.002	1.12 ± 0.01	1.12 ± 0.01	1.015 ±0.002
Blood	Negative	Negative	Negative	Negative
Bilirubin	Small	Small	Small	Small
Glucose (mg/dl)	Negative	Negative	Negative	Negative
Ketones(mg/dl)	Negative	Negative	Negative	Negative
Leucocytes	Negative	Negative	Negative	Negative
Nitrite	Positive	Positive	Positive	Positive

Table 4.3: Urine analysis of samples collected from Zn-Al LDHs exposed Wistar rats. The data was expressed in mean ± S.D, n=3.

4.3.6 Gross pathology

The rats sacrificed were examined for any observable changes, gross abnormalities or lesions. Gross abnormality was not detected. No observable lesions were found in any of the rats examined. Pictorial representation included as figure 4.31.

Figure 4.31: Gross pathology of Wistar rat intraperitoneally administrated with Zn-Al LDHs.

4.3.7 Organ weight

Upon sacrifice, four organs liver, kidney, spleen and brain were collected from all 12 rats. The total weight of each organ was measured and tabulated in **Table 4.4.**

ORGAN	CONTROL	3RD DAY	7TH DAY	14TH DAY
BRAIN (g)	1.67 ± 0.04	1.78 ± 0.15	1.54 ± 0.07	1.64 ± 0.13
LIVER (g)	9.29 ± 4.47	10.29 ± 3.01	7.61 ± 4.44	8.78 ± 1.85
SPLEEN (g)	0.54 ± 0.11	0.48 ± 0.05	0.51 ± 0.19	0.52 ± 0.03

Sree Chitra Tirunal Institute for Medical Sciences and Technology, Trivandrum

KIDNEY (g)	1.68 ± 0.72	1.82 ± 0.66	1.54 ± 0.41	1.65 ± 0.13

Table 4.4: The organ (brain, liver, spleen and kidney) weights of Wistar rats (in grams) exposed to Zn-Al LDHs via i.p route. The data was expressed in mean ± S.D and n=3.

4.3.8 Anti-oxidant assays

4.3.8.1 Protein level

The protein levels showed small fluctuations in brain and liver but were not significantly different in test groups rats compared to normal unexposed rats. The protein level in both brain and liver showed a decrease on 3rd and 7th day and then showed comparable level to control on the 14th day. The results were included in Figure 4.32.

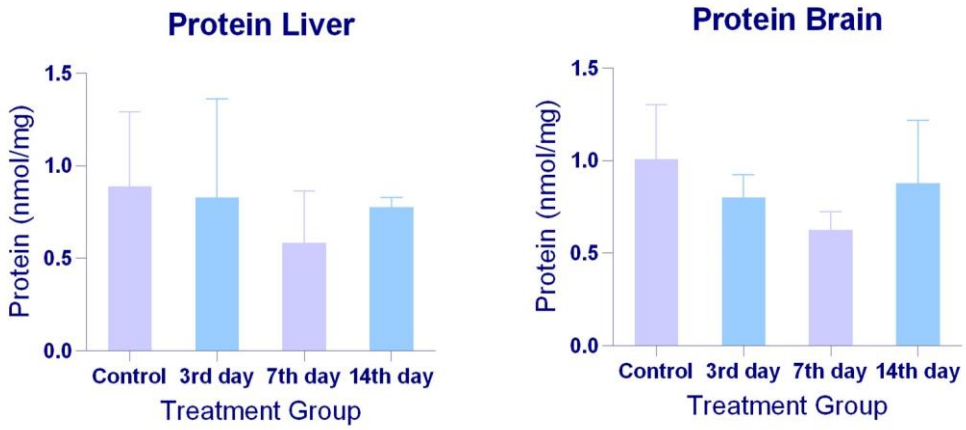

Figure 4.32: The protein level in (a) liver and (b) brain of Wistar rats injected with Zn-Al LDHs. The data represent mean ± SD and n=3.

4.3.8.2 GSH

The total GSH level in liver showed a slight increase on the 7th day result (0.34 ± 0.07 nmol/mg protein) compared to control (0.27 ± 0.08 nmol/mg protein), 3rd day (0.24 ± 0.05 nmol/mg protein) and 14th day (0.26 ± 0.03 nmol/mg protein). The GSH level in brain was 0.29 ± 0.005 nmol/mg protein in control, 0.22 ± 0.07 nmol/mg protein in 3rd

day samples, 0.22 ± 0.1 nmol/mg protein in 7th day and 0.33± 0.05 nmol/mg protein in 14th day samples. The results were graphically represented in Figure 4.33.

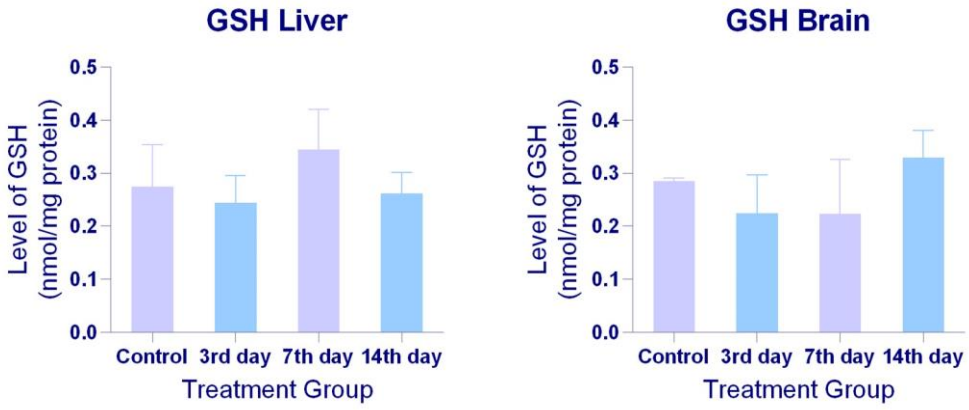

Figure 4.33: The GSH level in (a) liver and (b) brain of Wistar rats injected with Zn-Al LDHs. The data represent mean ± SD and n=3.

4.3.8.3 LPO

The LPO in brain and liver remained similar to that of control in the analyzed samples. The LPO was marked as a function of malondialdehyde (MDA) concentration. The MDA levels in brain were 1.11 ± 0.04 (control), 1.10 ± 0.06 (3rd day), 1.13 ± 0.21 (7th day) and 1.19 ± 0.09 (14th day) nmoles/ mg protein. Results from the LPO level in the liver showed similar range in control, 3rd and 7th day, a slight increase in LPO level (1.36 ± 0.12 nmoles/mg protein) was observed in the 14th-day samples. The results are included in Figure 4.34**.**

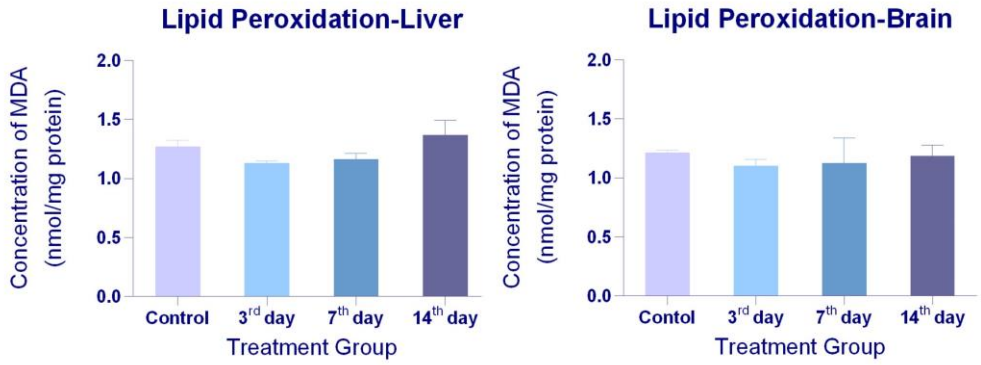

Figure 4.34: The figure includes the LPO estimation in a) liver and b) brain after exposure to Zn-Al LDHs. The graph was plotted with mean ± SD, n=3.

4.3.9 Splenocyte proliferation

The proliferation capacity of spleen after exposure to Zn-Al LDHs was compared with control spleens with the help of tritiated thymidine (Figure 4.35). .The proliferation capacity of spleen was observed to slightly increase on 3rd day (152.33 ± 5.03 CPM), decrease on 7th day (109 ± 17.9 CPM) and almost normalize to control value 138.53 ± 37.53 CPM) on 14th day (141 ± 20.79 CPM).

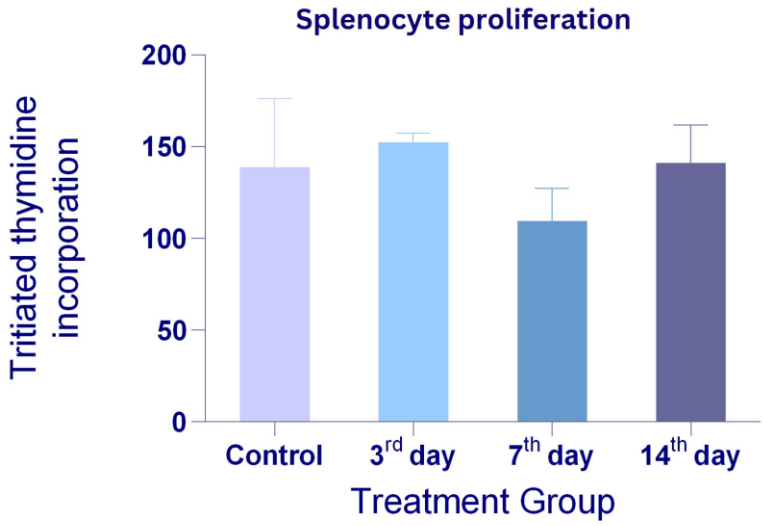

Figure 4.35: The splenocyte proliferation capacity of Wistar rats (control and Zn-Al LDHs exposed). The graph was plotted with mean ± SD, n=3

4.3.10 Biodistribution

The Zn and Al content in liver, kidney, brain and blood post i.p exposure to Zn-Al LDHs was examined using ICP-MS analysis. The Zn and Al level in kidney and blood remained comparable to that of control blood samples in all the three test groups. In case of liver, the Al level remained similar to control while Zn content was observed to slightly increase on 7th day (51.85 ± 15.1 ppm) compared to the control (43.85 ± 3.3 ppm). Small fluctuations in Zn levels were noted in brain samples but no significant difference from control brain samples was observed. The Zn content was found to be lower on 3rd day but was seen to be normalized by 7th and 14th day. No significant increase or decrease in both Zn and Al levels were observable in rats exposed to Zn-Al LDHs. The Zn and Al distribution in blood, liver, kidney and brain were graphically represented in Figure 4.36.

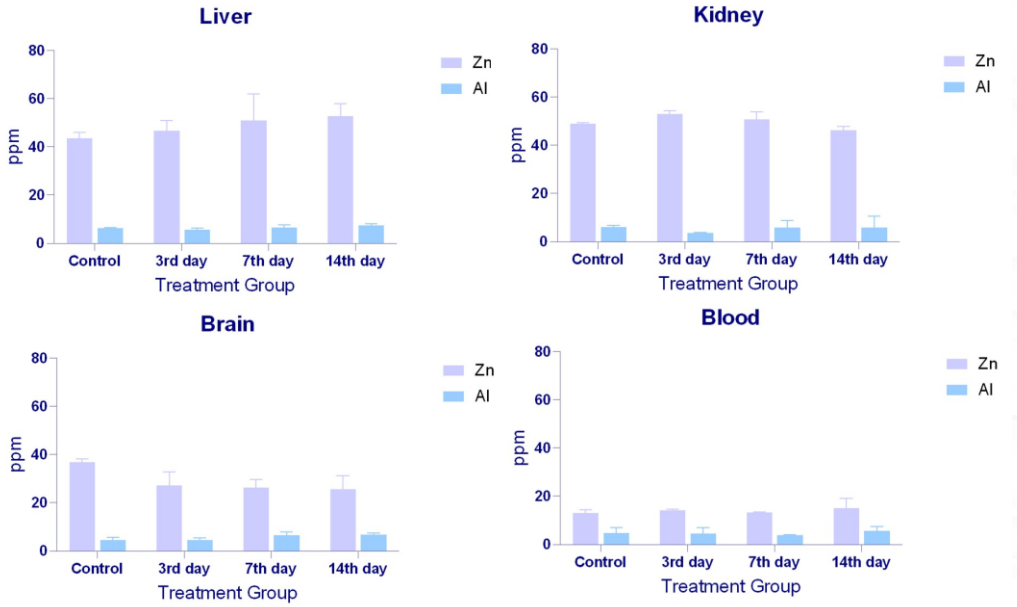

Figure 4.36: Estimation of Zn and Al content in a) liver, b) kidney, c) brain and d) blood after Zn-Al exposure using ICP-MS analysis.

4.3.11 Histopathology

Histopathological examination of liver, kidney, spleen and brain was done to check if Zn-Al LDHs exposure causes any potential tissue damage. The spleen sections from control, day 3, day 7 and day 14 samples showed normal splenic architecture. The white and red pulps were clearly seen in control as well as in spleen sections collected from Zn-Al LDHs exposed samples without any evident pathological changes. The brain sections showed normal morphology for neurons and no inflammations were observed in the sections collected from all four groups. Histograms of kidney specimens from control, 3rd day, 7th day and 14th day rats featured Bowman's capsules and tubules denoting normal pathology of kidney. Spleen, kidney and brain sections showed normal histopathological features (Figure 4.37). No toxic effect was evident in brain, kidney and spleen specimens collected post-exposure to Zn-Al LDHs.

In case of liver, periportal infilteration was found on 3rd and 14th day. Reactive hepatocytes were found in 3rd day liver (Figure 4.37). There was an incidence of periportal infilteration in one case at the end of 14th day. The micrographs obtained from the histopathological analysis were included in figure 4.37**.**

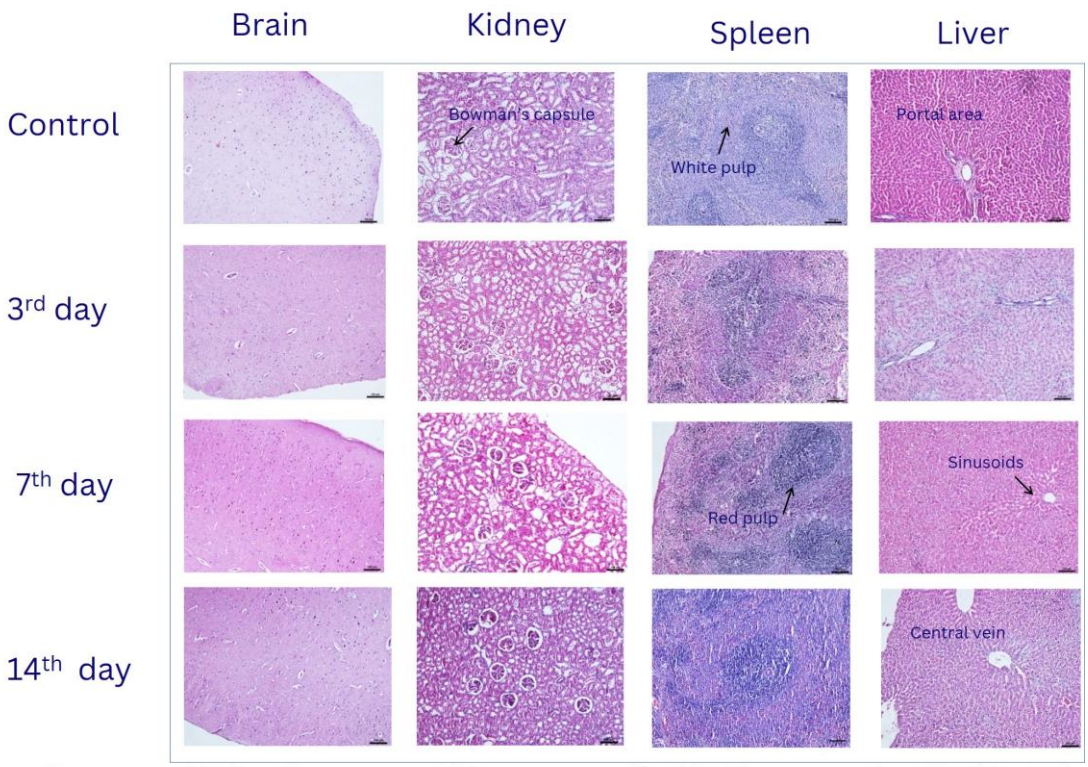

Figure 4.37: Histology of brain, kidney, spleen and liver of Wistar rats exposed to Zn-Al LDHs obtained after H & E staining. Magnification: 20x and scale bar: 100 µm.

DISCUSSION

5. DISCUSSION

5.1 *Synthesis and Physico-chemical characterization of 2D Zn-Al LDHs*

5.1.1 Synthesis of Zn-Al LDHs

Layered double hydroxides (LDHs) arose as one of the recent pacesetters in material science and biomedical field because of their two-dimensionality, high surface area, ion-exchange capacity, chemical composition, and tuneable properties (Murali, A., *et al* 2021). The characteristics of LDHs are greatly susceptible to the synthesis condition and therefore the selection of synthesis route remains highly decisive in controlling the exhibiting properties. LDHs can be fabricated in diverse chemical compositions; among them, Zn-Al LDHs are a highly sought-after combination fabricated and researched for diverse applications [Seftel EM *et al*., 2008, Cao F *et al.*, 2012].

The synthesis of the material of interest- Zn-Al LDHs was done by adopting the co-precipitation method for the nucleation step followed by hydrothermal treatment. Reports suggest co-precipitation at constant pH as the most consistent route for the synthesis of LDHs with even distribution of particle size and chemical composition [Abderrazek K *et al.*, 2017]. The metal composition, ratio, and intercalated anions, precursor salt selection turns out to be important factors that rule the properties and applicability of LDHs. Zinc nitrate ($Zn(NO_3)_2 \cdot 6H_2O$) and aluminium nitrate nonahydrate ($Al(NO_3)_3 \cdot 9H_2O$) in 2:1 ratio was co-precipitated at pH 8 and carbonate was selected as the intercalating anion. The nitrate salts of Zn-Al LDHs were reported to yield hydrotalcite phase LDHs alone rather than hydrotalcite- metal oxide mixed phase seen in reactions with sulphate salt as precursors [Bukhtiyarova *et al* 2019]. One of the demerits of co-precipitation method is the low crystallinity of the precipitated LDHs. Thermal aging of the precipitated LDHs is one solution proven for improving the crystalline nature [Zhao *et al.,* 2002]. Also, taking up separate nucleation and aging step helps in narrowing down the particle size distribution

[Tonelli *et al.,* 2021]. Therefore in the current study, nucleation was done by co-precipitating at 0^0 C and the precipitated solution was aged hydrothermally for 4 h at 80^0 C. Repeated washing of the aged solution with D.I water helped in removing the unwanted residues and yield pure white LDHs powder on drying at 80^0 C for 24 h.

5.1.2 Characterization of Zn-Al LDHs

5.1.2.1 *Size and morphological characterization using TEM*

TEM images showed hexagonal LDHs structures with an average size of 102 nm. The hexagonal shape is the typical morphology of LDHs formed as the natural crystallographic tendency of rhombohedral structures [Liu J *et al.,* 2006]. LDHs morphology is greatly dependent on the reaction conditions and acquires different shapes depending on various parameters. Spherical morphology is acquired when precipitated at high- supersaturation while hexagonal morphology with sharp edges is attained at low supersaturation [Tichit D *et al.,* 2019]. The hexagonal morphology thus indicates the successful fine-tuning of reaction parameters to attain co-precipitation at low supersaturation.

5.1.2.2 Crystal structure and phase identification using XRD

The XRD imaging showed typical basal peaks [(003), (006), (009)] of Zn-Al LDHs at low 2Ɵ values and non-basal peaks [(015), (018), (110) and (113)] at high 2Ɵ values. The reflections at (006) and (009) correspond to the parallel orientation of brucite layers and confirm the layered parallel structure for the synthesized Zn-Al LDHs [Khanal, S *et al.,* 2022]. The d spacing (003) for the synthesized LDHs was calculated as 0.75 nm similar to previous reports [Khanal, S *et al*., 2022]. The lattice parameters a and c values were estimated as 0.307 nm and 2.25 nm which were in accordance with published literature works [Richetta M *et al*., 2018]. According to the XRD results, the reflections suggest that the synthesized Zn-Al LDHs showed rhombohedral symmetry. For rhombohedral symmetry, reflections are found at h+k+ l= 3n, where n is any

integer value [Evans and Slade 2006, Prestopino *et al.,* 2019]. The XRD pattern of the synthesized material concludes to have hexagonal units with rhombohedral symmetry.

5.1.2.3 Chemical group identification using FT-IR spectroscopy

The FT-IR spectra showed peaks corresponding to all the characteristic functional groups present in Zn-Al LDHs structure. The peak pattern was matching with the previous reports on the same material [Khanal S *et al.,* 2022]. The broad peak at 3361.92 cm^{-1} matches to typical hydroxyl (OH) stretching mode which features the presence of hydroxyl groups connected to central metal ions in the octahedrons and the intercalated water molecules. This observation is in agreement with the basic structure of LDHs in which each metal atom at the centre of an edge-sharing octahedron is connected to six OH groups forming brucite layers. The partially charged layers are intercalated with water molecules and anions [Evans and Slade 2006]. A sharp peak at 1340.52 cm^{-1} matches the asymmetric stretching vibration of the carbonyl group conforming carbonate intercalation in between brucite layers. A small peak at 1631.77 cm^{-1} proves the presence of intercalated water. The peaks at 734.87 cm^{-1} and 541.9 cm^{-1} were from the Al-O vibrations while the other peak at 677.01 cm^{-1} was from the Zn-O vibrations. The obtained peaks were matching to the LDHs fabrication results of Abderrazek *et al .,* 2017.

5.1.2.4 Chemical group identification using Raman spectroscopy

The functional groups present in the prepared Zn-Al LDHs were further confirmed using Raman spectroscopy. Raman spectra helped to get a better picture of the chemical bonding present in the fabricated Zn-Al LDHs. The peak seen at 3471 cm^{-1} links to water vibrations that include water bonded to M_3OH units or intercalated carbonate ions [Johnson TE *et al*., 2002]. The peak at 1052 cm^{-1} showed the vibrational mode peculiar to CO_3^{2-} conforming carbonate intercalation. The peaks observed at 2885-2921 cm^{-1} correspond to the vibration from absorbed carbonate ions in the LDHs structure. These observations were also mentioned by Balcomb *et al* in 2015 during

the characterization of different types of LDHs (Mg-Fe, Zn-Al, and Zn-Fe) using Raman spectroscopy. The peaks at 495 and 555 cm^{-1} trade to the metal-oxygen bonds: Zn-O and Al-O bonds respectively. The peak at 152 cm^{-1} attributed to the O-M-O bonds. The obtained results were co-relatable to the previous reports [Frost RL *et al.,* 2009].

5.1.2.5 Thermal degradation profiling

The TGA analysis showed major weight loss of 36.48 % w/w in five major steps. (1) loss of absorbed water, (2) loss of intercalated water (3) dehydroxylation of brucite layers, (4) decomposition of intercalated carbonate and (5) decomposition to mixed metal oxide. The initial weight loss of 2.76 % w/w (temperature upto 102^0C) corresponds to loss from removal of surface absorbed water. The second weight loss (11.81 %) observed from 102^0 to 170^0 C stands for the elimination of intercalated water molecules. The dehydroxylation and carbonate decomposition were responsible for the further weight loss of 22.28 %, seen with the gradual increase in temperature up to 500^0 C. This finding matches the TGA analysis of LDHs reported by Zhang *et al* in 2004. The weight loss observed after 500^0 C was from the transition of LDHs to MMO [Kloprogge JT *et al.,* 2004].

5.1.2.6 Thermal stability check using DTA

The DTA analysis was in agreement with the outputs from TGA analysis and complemented the findings. DTA spectra showed the first endothermic reaction taking place to be loss of surface adsorbed water and intercalated water at 165^0 C. Water loss was followed by endothermic reactions: dehydroxylation and carbonate decomposition, evident at around 250^0 C. Similar DTA curves were also reported by Cui *et al* in 2010 for LDHs. The graph pattern above 312^0 C shows the possible collapse in LDHs structure at higher temperatures to MMO (Cocheci, L 2019).

5.1.2.7 Hydrodynamic size analysis using DLS

DLS technique was opted to estimate the hydrodynamic size, and collect information about the dispersity of the synthesized LDHs, aggregation tendency and particle size distribution. The hydrodynamic size of Zn-Al LDHs varied from 101.2 nm in culture media to 136.2 nm in ethanol. Zn-Al LDHs showed better polydispersity in ethanol (P.D.I = 0.352) compared to culture media (P.D.I = 0.421). P.D.I < 0.7 indicates narrow particle size distribution [Nasiriboroumand *et al.,* 2018]. Therefore, DLS data indicate appreciable dispersity and narrow particle size distribution for the synthesized Zn-Al LDHs.

5.1.2.8 Charge confirmation using Zeta potential analysis

LDHs possess a net positive charge because of the partial M(III) substitution in the brucite layers [Goh *et al.,* 2008]. The Zeta potential measurement showed a charge of +24.3 ± 3.47 mV validating the successful fabrication of positive brucite LDHs layers. Another study by Huo *et al* also reported similar findings while estimating the charge of Zn-Al LDHs at pH 7 [Huo *et al.,* 2022]. The positive charge of LDHs facilitates interaction with the negatively charged cell membrane and eases cellular uptake in contrast to uncharged or negatively charged nanoparticles. Furthermore, the positive charge of LDHs also enables the loading of negatively charged drugs/ genes/ biomolecules making them a good pick as a delivery vector in therapeutics [Yan *et al.,* 2019].

5.2 Evaluation of cellular interactions of 2D Zn-Al LDHs

Although nanomaterials with their mesmerizing properties remain glorified for its potential biomedical applications on one side, there exists another side to the coin where the toxicity concerns weaken their usage. The lack of understanding of the possible interactions of the nanoparticle with the exposed biological systems and aftermath reactions creates a gap between the successful material fabrication and its actual applicability. Therefore, nanotoxicology has emerged as a vital research field focused on getting a better understanding of bio-nano interactions and helping in the smoothening lab to bedside translation [Krug *et al.,* 2011]. In the present study, the interaction of the synthesized Zn-Al LDHs *in-vitro* systems was examined and potential toxicity was evaluated. For the study, toxicity screening was done with different endpoints namely mitochondrial metabolism, lysosomal activity, oxidative stress, membrane permeability, cytoskeletal integrity, genotoxicity, mechanism of cell death *etc.*

5.2.1 Evaluation of cellular interactions of 2D Zn-Al LDHs with L929 cells

Understanding the interaction of nanomaterials with the different organelles could help deeply to estimate the potential toxicity of nanoparticles [Unfried K *et al.,* 2007]. Therefore, the effect of Zn-Al LDHs upon exposure to L929 cells was monitored by comprehending the cellular responses post uptake on major target cellular compartments like mitochondria, lysosomes, cytoskeleton and nuclei. The major mechanisms of cytotoxicity induced by nanoparticles are reported to be via (1) membrane rupture (2) affecting cellular metabolism causing energy imbalance, (3) disturbing lysosomal activity (4) oxidative stress, (5) cytoskeleton rupture leading to intracellular transportation disorder (6) DNA damage, (7) apoptosis *etc.,* [Sukhanova *et al.,* 2018]. In this context, various *in-vitro* assays were carried out to inspect the possible incidence of toxicity via any of the cytotoxic mechanisms.

5.2.1.1 Cellular uptake of 2D Zn-Al LDHs by L929 cells

The cellular uptake of 2D Zn-Al LDHs by L929 cells was evaluated by using flow cytometry analysis. Cellular uptake of nanoparticles will cause granularity increase in exposed cells compared to normal unexposed cells. An increment in granularity is detectable in inflow cytometry as an upsurge in side scattering and therefore side scattering is used as a marker for nanoparticle internalization [Cui X *et al.,* 2016]. Imaging flow cytometry analysis of L929 cells exposed to Zn-Al LDHs showed an increase in side scattering with increasing concentration of LDHs exposure. The increase in the intensity of side-scattering was evident in channel 6 of imaging flow cytometry micro graphs. The graph showing side scateering showed an increased shift in Zn-Al LDHs treated cells compared to control L929 cells that denotes uptake. Cell death could also result in a granularity increase [Foldbjerg R *et al.,* 2011]. Inorder to check this possibility and confirm that the SSC increase was from the LDHs internalization, % cell death was further confirmed by sorting Annexin-PI-stained cells. No significant increase in cell death was observed for L929 cells exposed to LDHs and hence, the possibility of cell death leading to granularity increase can be ruled out. Therefore, the increase in side scattering can be attributed to increasing cellular internalization. The detailed result of Annexin-PI cell sorting is included in section 5.2.1.9.

5.2.1.2 Cellular metabolic activity check using MTT assay

Cell viability is a key indicative factor in deciding the toxic potential of nanomaterial or toxicants in general. The proportion of live and dead cells is fundamental in concluding whether the interaction is compatible or toxic to the exposed system [Asha Rani *et al.,* 2009]. So, MTT assay was carried out on L929 cells incubated with different concentrations of Zn-Al LDHs for varying time periods to estimate the live-dead cell % post-incubation. Mitochondria are one of the major target cellular compartments for nanomaterial toxicity. There are many reports on the induction of

mitochondrial damage on nanomaterial exposure. For instance, nanomaterials are proven to induce permeability concerns, morphological change, mitochondrial membrane potential loss and disturb the normal functioning of mitochondria [Wu D *et al.,* 2020]. For the present study, more than 80% of L929 cells were viable for 3 h, 6 h, 24 h and 48 h exposure. A material is considered cytotoxic if the % of viable cells falls below 70 % post-exposure to the material [ISO 10993-5]. The MTT results showed that the % of viable cells was well above the cytotoxic limits. The absorbance in exposed wells did not show any markable decrease in comparison to unexposed wells indicating that the mitochondrial activity of L929 cells was not affected with Zn-Al LDHs incubation. Hence, according to the MTT results, it was inferred that Zn-Al LDHs interaction with L929 cells showed a non-cytotoxic response.

5.2.1.3 Cell viability assessment using Live/dead assay

For qualitative cytotoxicity assessment of Zn- Al LDHs, live/dead assay was done by labeling viable and dead cells with calcein AM and PI fluorescent dyes respectively. The fluorescence micrographs showed attached green fluorescent cells in majority and only a small fraction of red fluorescence was observed. The confluent adherent cells without any apparent morphological changes indicated a non-toxic interaction between Zn-Al LDHs and L929 cells. Earlier, functionalized Mg–Mn–Al layered double hydroxides with MoS_2 doping were also scrutinized in another study for their biocompatibility and similar results were found. The material was fabricated with the aim of photothermal therapy by utilizing the PTT efficiency of doped MoS_2 and catalytic properties of LDHs. The aforementioned type of LDHs was incubated with L929 cells for a set of concentrations ranging from 50 µg/mL to 500 µg/mL. A live/dead assay using calcein-AM/ PI dual dyes showed that the cell viability was not compromised with LDHs exposure and the densely populated L929 cells post-exposure were evidently seen in optical imaging. The overall study report by Zhao *et al* indeed favoured the developed material for PTT applications [Zhao *et al.,* 2021].

5.2.1.4 Lysosomal activity evaluation using NRU

Lysosomes are another prime target of nanoparticles. The chances of nano-lysosome interactions are high since lysosomes possess the function of endocytosis and therefore take up foreign bodies as a defensive mechanism [Frohlich E *et al.,* 2013]. Bexiga *et al* stated that the NH_2-modified polystyrene nanoparticle having a positive charge induced morphological changes in lysosomes post-treatment. The study also found that the cationic nanoparticle-induced lysosomal membrane breakage and leakage of enzymes. Cationic particles are likely to get accumulated at lysosomes having low (acidic range) pH [Bexiga *et al*.,2011]. Hence, lysosomes turn out to be an important potential target of LDHs cytotoxicity because of their charge. The NRU assay outcomes from the present study suggested that the lysosomes health or activity was not damaged with the Zn-Al LDHs exposure. The cell viability quantification from NRU assay showed a similar trend to that of MTT assay, the cell viability at the highest endpoints of exposure concentration and time (160 µg/ml and 48 h respectively) showed high values, well within the non-cytotoxic reference range. The optical micrographs taken for the L929 cells treated with Zn-Al LDHs for 24 h showed active uptake of NR dye by the lysosomes in all treatment groups without any detectable difference.

5.2.1.5 Lysosomal integrity assessment using AO staining

There were few studies that showed concerns regarding the results of NRU assay for nanoparticle cytotoxicity. For example, carbon-based nanoparticles were reported to interfere with the NRU assay and give false-positive results [Casey A *et al.,* 2007]. Lysosome being a potential target organelle for LDHs, AO staining was also carried out to double-check the LDHs' impact on lysosomes and rule out any chance of dye interference in the results. No disappearance in red fluorescence was observed

suggesting that Zn-Al LDHs exposure did not trigger lysosome damage or dysfunction.

5.2.1.6 Oxidative stress assessment using DCFH-DA assay

Oxidative stress is a widely noticed toxicity response associated with nanoparticle exposure. Henceforth, the general ROS production in L929 cells exposed to the synthesized LDHs was marked using DCFH-DA as the fluorescent probe. The DCFH-DA results from the L929-Zn-Al LDHs 24 h exposure showcased that the test material does not cause any significant hike in the ROS generation in exposed cells. The comparable levels of ROS in treated wells and control wells indicate an absence of significant oxidative stress-inducing tendency of Zn-Al LDHs. A similar inference was made by Choi *et al* in 2015 while investigating the chances of ROS production when exposed to Mg-Al LDHs. According to the study, a significant elevation in ROS levels was only observed at high doses of 250 to 1000 µg/mL [Choi *et al.,* 2015].

5.2.1.7 Cytoskeletal and nuclear integrity screening using Rhodamine-phalloidin-DAPI staining

The cytoskeleton is responsive to the structural framework of cells and is composed of filamentous assemblies of microtubules, actin fibers and intermediate filaments [Chazotte B *et al*., 2010]. Actin is an important protein present in the cytoskeleton that plays a crucial role in cell division and adhesion. During foreign body invasion in cells, actin filaments are damaged so as to impede phagocytosis. Actin damage leads to the loss of structural integrity of cells. In many nanotoxicological evaluations, cytoskeleton disruption and nuclear damage are two widely seen cytotoxicity impacts created by nanomaterials. ZnO nanoparticles were held responsible for inducing actin depolymerization and nuclei condensation at concentrations 75 µg/mL and 100 µg/mL. A clear-cut indication of cytoskeleton damage and nuclei shrinkage was observed in fluorescence micrographs after rhodamine and DAPI staining [Pati R *et al.,* 2016]. In the current study, F-actin and nuclei were found to be uninterrupted with

particle exposure. The fluorescence micrographs of L929 cells with properly orientated actin fibers imply a non-destructive interaction. Also, an absence of nuclear condensation or multinucleation suggests a non-toxic response at the nuclear level.

5.2.1.8 Nuclear integrity and apoptosis estimation using DNA laddering

DNA laddering is regarded as a hallmark assay for apoptosis detection. The pattern obtained in DNA laddering draws the line of understanding whether the mode of cell death is via apoptosis or necrosis. Inter-nucleosomal DNA cleavage takes-place in apoptosis while in necrosis random cleavage occurs [Harshita *et al.,* 2019]. During apoptosis (programmed cell death), genomic DNAs are cleaved by specific endonuclease enzymes like caspase-activated DNAse. The DNA ladder in case of apoptotic cell death pathway displays a fragmented pattern with fragments of 180-200 base pair length. Necrotic cell death is marked by smear formation in the DNA ladder because of irregular fragmentation [Harshita *et al.,* 2019]. Cationic nanoparticles are overlooked for their potential to influence the DNA structure. The possibility of electrostatic interaction between cationic nanoparticles and negatively charged DNA rises concerns about the structural and conformational stability of DNA [Railsback *et al.,* 2012]. On the other hand, there is also literature showing cationic nanoparticles to be devoid of inducing any DNA damage/ fragmentation. For example, Doktorovova *et al* reported lipid nanoparticles with a positive charge to show DNA compatible response in two human cell lines: Caco-2 (colorectal adenocarcinoma) and HepG2 (hepatoma) at 0.1mg/mL concentration [Doktorovova *et al.,* 2014]. In the current study, DNA fragmentation or smear formation was absent for all the tested samples. The DNA isolated from LDHs exposed cells showed a similar laddering pattern to that of control samples which suggests an absence of genotoxic retort.

5.2.1.9 Apoptosis/ Necrosis detection by Annexin-PI flow cytometry analysis

The cytotoxicity of nanoparticles is dependent on many of the characteristic parameters like size, composition, surface chemistry, charge *etc*., The mechanistic cell

death pathway involved in the cytotoxic response is influenced by the above-mentioned factors. The charge of the nanoparticles at times exhibits an influential role in cytotoxicity. In a work reported by Wei *et al.,* 2015, cationic nanocarriers were seen to influence the cell membrane potential and trigger cell death via necrosis. The nanocarriers exhibited surface charge-dependent cytotoxicity and an increase in necrotic cell death with an increasing positive charge of nanoparticles, thereby confirming the impact of the charge on cellular interactions. Also in another literature, positively charged silver nanoparticles were found to induce cell death via apoptosis when exposed to breast cancer cell death. In that case, unmodified bare silver nanoparticle with a higher positive charge was found to exhibit higher apoptosis rate relative to core-shell/ non-surface functionalized nanoparticles [Liu *et al.,* 2015]. So, a conclusive prediction on the nature of interactions at the bio-nano level is impossible while considering nanoparticle charge or any other single parameter alone. The fate of the exposed cells is decided by the comprehensive effect of different parameters like shape, composition, size, charge, dose *etc.,* and therefore varies with each case [De Stefano *et al.,* 2012]. The quantification of apoptotic and necrotic L929 cells post-treatment with Zn-Al LDHs was analyzed with the help of Annexin-V/PI staining. There was significant increase in neither necrotic nor apoptotic cells s in Zn-Al LDHs exposed cells compared to untreated cells. The results suggest a non-cytotoxic response of L929 cells to Zn-Al LDHs. In a similar study using another type of LDHs (Mg-Al LDHs) having hexagonal morphology and an average particle size of 100 nm, relatable results were found. Annexin/PI staining of embryonic stem cells exposed to Mg-Al LDHs exhibited neither an increase in apoptotic nor necrotic cells in assessment with the unexposed cells, proposing a non-cytotoxic interaction [Wu *et al.,* 2015].

5.2.1.10 Leachout toxicity

Nanomaterials/ bioimplants of metallic composition possess potential leach-out toxicity because of possible metal ion release. So, it is important to check the impact of resultant leachout at the cellular level. For this, the extract from the test

nanomaterials/ bioimplants are procured as per the ISO standard guidelines and exposed to cells. The extract cytotoxicity may be influenced by the metal composition, amount of metal ion release and exposure time [Granchi, D *et al.*, 1996]. The extract helps to mimic the *in-vivo* condition and estimate the possible toxicity from the ion release. The leach-out toxic potential of Zn-Al LDHs on L929 cells was estimated with MTT and NRU assays.

5.2.1.10.1 Metabolic activity assessment using MTT assay

Metals and alloys have been widely explored for implants, especially for bone applications. They are also scrutinized for the potential toxic effect imparted as a consequence of metal ion release [Sun *et al.,* 1997]. The presence of Zn and Al in the synthesized LDHs also triggers doubts about the leaching of ions causing unwanted reactions. Zinc comes under the essential element category mentioned for the human body. But concerns regarding the effect of Zn ions released from biomedical implants are also overlooked because of their higher ion release rate, as well as exposure time, could contribute to toxicity. For example, in a study that checked the effect of alloy extract containing Zn ions, the conclusive remark reported was that extract with concentrations above 80 µM imparted negative impacts on cell viability while lower doses showed non-toxic response [Kubásek *et al.,* 2016]. In another study, extract from aluminum oxide nanoparticles was collected and exposed on freshwater algae to understand the effect of aluminum leachout. The MTT results in that case, was indicating a toxic response and a decrease in viability when exposed to 72 h extract [Pakrashi *et al.,* 2013]. Ardlin *et al* and group mentioned that MEM culture media extract of dental composite made of copper-aluminum-nickel alloy showed non-cytotoxic response on fibroblast cells [Ardlin *et al.,* 2009]. For the present work, the MTT assay of the Zn-Al LDHs extract showed no significant reduction in metabolic activity or cell viability for both 24 and 72 h extract-exposed L929 cells.

5.2.1.10.2 Lysosomal activity evaluation using NRU assay

The NRU assay viability check was also in concordance with the MTT outcomes and no potential harm to L929 cells was observed when treated with the Zn-Al LDHs extracts. No remarkable decrease in lysosomal activity was induced by the extract exposure in L929 cells suggesting an absence of noxious response for the checked exposure times.

5.2.2 Evaluation of cellular interactions of 2D Zn-Al LDHs with HOS cells

Bone tissue engineering being the prime scope of LDHs applications, it is an ineludible compulsion to check its compatibility with osteoblast cells. Henceforth, the compatibility of prepared Zn-Al LDHs against HOS cells was analyzed for different endpoints like cell viability, metabolic activity, mitochondrial membrane potential, lysosomal activity, oxidative stress, cell membrane permeability, cytoskeleton structure, nuclear integrity, induction of apoptosis *etc*.,

5.2.2.1 Cellular viability and metabolic activity check by MTT assay

The MTT results for exposure time periods of 3 h, 24 h and 48 h exhibited that Zn-Al LDHs interference with HOS cells did not induce any significant reduction in cell viability post-exposure. The mitochondrial activity of exposed cells was not compromised on interaction with the synthesized Zn-Al LDHs. Similar results were reported previously in the case of Mg-Al LDHs in composite form with bone cement. Mg-Al LDHs-bone cement composite was found to express high viable cell proportion and biocompatibility post-treatment compared to bare bone cement in MG-63 human osteoblast-like cells. The abovementioned study supported that Mg-Al LDHs presence afforded positive contributions to the composite's biocompatibility [Kapusetti G *et al.,* 2012].

5.2.2.2 Cellular cytotoxicity examination using live/dead assay

The micrographs after AO/EtBr staining showed that the majority of the cells were seen as uniform green fluorescent cells denoting live cells. Few red cells showcased PI permeabilization due to cellular damage, but the number of red cells was insignificant to the number of green cells. Therefore, it can be deduced that Zn-Al LDHs exposure does not provoke a cytotoxic response in HOS cells. The study by Choi *et al* with Mg-Al LDHs with A549 cells also draws a similar conclusion. It was stated that Mg-Al LDHs did not indicate any cytotoxicity in A549 cells upto 500µg/mL concentration for 48 h exposure time [Choi *et al.,* 2009].

5.2.2.3 Mitochondrial membrane potential (MMP) by JC1 staining

Red spots of JC1 dye evident from the fluorescence micrographs of exposed cells suggest normal accumulation of the dye in mitochondrial. The MMP of HOS cells exposed to all the selected concentrations of Zn-Al LDHs were comparable to untreated cells. Accordingly, JC1 staining results lead to the inference that the synthesized Zn-Al LDHs did not noticeably alter the MMP of HOS cells post-exposure upto 24h. The study by Zhang *et al* with Cobalt (Co)-based LDHs was also in support to the present findings. Co-Al LDHs nanosheets at concentrations of 50, 100 and 150 µg/mL were found to maintain MMP in endothelial cells without significant decrement from MMP of untreated cells [Zhang *et al.,* 2022].

5.2.2.4 Morphological analysis by Giemsa staining

Cell morphology alterations are considered a marker for cytotoxic response to toxicant exposure. For instance, oleic acid-modified iron oxide nanoparticles influenced the cell morphology and caused reduction in lateral extension [Mbeh DA *et al.,* 2012]. The micrographs in that particular study showed that oleic acid-modified iron oxide nanoparticles caused disturbances in cell adhesion and structure, suggesting a

cytotoxic response. The morphological analysis using Giemsa staining displayed normal physiological shape for particle-treated HOS cells. The comparable morphological features of exposed cells with normal untreated cells also propound a non-cytotoxic response of Zn-Al LDHs on HOS cells.

5.2.2.5 Morphological analysis by Coomassie brilliant blue staining

In order to countercheck the effect of LDHs on HOS morphology, coomassie brilliant blue staining was also done. The micrographs showed that Zn-Al LDHs exposed HOS cells were stained without any evident abnormalities in morphology compared to normal cells. The results obtained were in parallel notion to the results of Giemsa staining confirming that Zn-Al LDHs did not trigger any evident non-cytocompatible interactions that could hinder the regular cellular structure. A similar result was also reported in a previous study, in which phase contrast imaging of PC12 cells exposed to LDHs composite for 72 h showed that the cells successfully sustained their structural integrity [Kura *et al.,* 2014].

5.2.2.6 Oxidative stress assessment using DCFH-DA assay

As mentioned in section 5.2.1.6 oxidative stress is one of the major mechanisms of nanomaterial toxicity. Quantification of ROS production helps track the potential oxidative stress. The ROS generation in HOS cells after 3 h exposure showed no remarkable increase compared to untreated cells. The HOS cells showed a dose-dependent slight increase in ROS production during 24 h and 48 h exposure but a significant overproduction of ROS was absent. The DCFH-DA assay results propose that Zn-Al LDHs upto 160 µg/ml concentration does not induce an extensive level ROS generation capable of causing oxidative stress. Choi *et al* in 2009 reported that Mg-Al LDHs of 200 ± 15 nm average size induced a dose-dependent ROS production leading to oxidative stress. Significant production of ROS production was observed after 72 h exposure to concentrations 250-500 µg/ml. Mg-containing LDHs exhibited

negligible cytotoxicity below 250 µg/ml dose concentration and shorter exposure time [Choi SJ *et al.,* 2009].

5.2.2.7 Cell membrane damage check using lactate dehydrogenase enzyme assay

Lactate dehydrogenase, the cytoplasmic enzyme is involved in the catalysis of pyruvate to lactate conversion reaction and parallel NAD to NADH. The quantification of pyruvate in the supernatant solution is used for the detection of cell membrane leakage, an indication of cytotoxic response [Kumar P *et al.,* 2018]. HOS cells treated with different concentrations of Zn-Al LDHs for 3 h showed no elevation in lactate dehydrogenase enzyme release. In the case of 24 h, an exposure concentration-dependent increase in lactate dehydrogenase release was observed but the percentage of enzyme release was not in the range of cytotoxic response. A previous report of A549 cells exposed to Mg-Al LDHs disclosed low and dose-dependent lactate dehydrogenase enzyme release and cytotoxic response after 24 and 48 h treatment. The study also marked that the enzyme release and cytotoxicity were relative to the size of LDHs. Noticeably, smaller particle size showed higher enzyme release and cytotoxicity. Mg-Al LDHs with 100 nm size (similar sized as the Zn-Al LDHs in the present study) displayed low enzyme release and stated absence of remarkable membrane damage [Choi S J *et al.,* 2008].

5.2.2.8 Lysosomal integrity assessment using Acridine orange staining

According to the AO fluorescencec imaging, the lysosomal integrity of HOS cells was seen to be regular. No change in lysosome pattern compared to untreated cells was manifested in fluorescence micrographs of exposed cells. So, the results suggest that Zn-Al LDHs exposure for 24 h did not impose any lysosomal impairment. An interesting work was reported by Hu *et al* recently, in which NiCoTi LDHs were explored for photothermal efficiency. In the study, the acridine orange staining revealed that exposure of HeLa cells to NiCoTi LDHs (30 µg/ml) did not compromise the integrity of lysosomes (membrane permeabilization) at acidic pH. The outcomes

of cell viability test done on HeLa cells post-LDHs exposure also established compatible interactions up to the highest tested concentration which was 100 µg/ml [Hu *et al.,* 2022].

5.2.2.9 Cytoskeletal and nuclear integrity screening using Rhodamine-phalloidin-DAPI staining

The cytoskeleton framework was not disrupted when exposed to varying concentrations of Zn-Al LDHs. The DAPI staining did not show any occurrence of nuclear condensation in Zn-Al LDHs exposed HOS cells. The rhodamine-phalloidin/DAPI counterstained images of exposed HOS cells point to a similar inference to that of L929 cells. Previously, Li *et al* reported enhanced adherence of stem cells on Titanium surface coated with yet another type of LDHs (Mg-Fe LDHs). In this study, Mg-Fe LDHs coating helped in improving of bone marrow mesenchymal stem cells adhesion than non-coated Ti surfaces. The rhodamine-phalloidin/ DAPI fluorescence staining images of the adherent stem cells confirmed characteristic cytoskeleton and cell morphology on LDHs-coated surfaces suggesting a compatible interaction between stem cells and Mg-Fe LDHs interface [Li Q *et al.,* 2018]. The rhodamine-phalloidin/ DAPI images from the present study also suggest a cytocompatible response towards the cytoskeleton and cell nuclei for the current doses of Zn-Al LDHs.

The rhodamine-phalloidin/ DAPI counter fluorescence staining images of the stem cells confirmed characteristic cytoskeleton and cell morphology on LDHs-coated surfaces validating a compatible interaction at the cell-Mg-Fe LDHs interface [Li Q *et al.,* 2018]. The rhodamine-phalloidin/ DAPI imaging of the present study also deduces that synthesized Zn-Al LDHs showcase a cytocompatible interaction towards the cytoskeleton and cell nuclei.

5.2.2.10 Nuclear integrity and apoptosis estimation using DNA laddering

As discussed in the previous section 5.2.1.8, DNA fragmentation is a marker for apoptosis-mediated cell death. The DNA laddering assay revealed that the test material (Zn-Al LDHs) upto the highest tested concentration of 160 µg/ml did not bring about any DNA fragmentation in HOS cells. From the laddering results, the absence of fragmented DNA pattern suggests that different concentrations of Zn-Al LDHs (10 µg/ml- 160 µg/ml) exposure does not evoke significant apoptosis or DNA damage.

5.3 Toxicity evaluation of 2D Zn-Al LDHs in rat model

5.3.1 Clinical signs

The Wistar rats were exposed to 10mg/Kg dose of Zn-Al LDHs intra-peritoneally and were closely observed for clinical signs. It was found that the Zn-Al LDHs exposure of the selected dose did not trigger any deviation in normal behavioural patterns of treated rats. Specifically, eating, drinking, movement, grooming, and the overall appearance of exposed rats were comparable to that of normal group rats. The particle exposure induced 0% mortality rate in all the test groups. In a similar study, Mg-Al LDHs was tested on female BALB/c mice model. It was observed that different-sized LDHs (50, 100, 200, and 350 nm) did not cause death of i.p injected mice for various dose concentrations (100, 300, 500, and 600 mg/kg) [Choi *et al.,* 2008].

5.3.2 Body weight

Body weight change is an immediate visible response observed as a sign of toxic retort to foreign material exposure. Choi *et al* investigated the potential size-dependent toxicity of Mg-Al LDHs in a mice model. The group found that irrespective of the size of selected LDHs, no significant weight loss was observed for test doses till 600 mg/Kg [Choi *et al.,* 2008]. In another study, 100-200 nm size ranged Mg-Al LDHs were injected into male Sprague Dawley rats and evaluated for toxicity. The findings for lower doses were comparable to the present study. For instance, Mg-Al LDHs of doses 60mg/Kg and 200 mg/Kg showed no remarkable weight loss and significant weight loss was only observed for high dose of 600mg/kg Mg-Al LDHs [Kwak *et al.,* 2004]. For the present study, experimentally the synthesized Zn-Al LDHs did not induce any significant weight loss in exposed rats.

5.3.3 Hematology

During the current study, the hematological indices like platelets, RBC, WBC and HGB of the test group rats showed slight alteration in hematological values, however all the values remained within the reference range for Wistar rats [Kondashevskaya *et al.,* 2006, CPCSEA 2006]. The hematology results of Zn-Al LDHs injected Wistar rats suggest that the test particles do not provoke remarkable changes in hematological markers and 10mg/Kg Zn-Al LDHs turn out to be within the tolerable limit for Wistar rats. Similar findings were reported for another type of LDHs (Mn-LDHs) by Xie *et al*. Manganese doped LDHs on exposure to Sprague Dawley rats was found to maintain the hematological parameters similar to unexposed rats suggesting an absence of any significant toxicity [Xie *et al.,* 2020]. Another group investigated the toxicity of Mg-Al LDHs to be male Sprague rats and found that the hematology markers remained comparable to normal rats without significant change [Kwark *et al.,* 2004]. Zhu *et al* and group explored the efficiency of Mg-Al LDHs as a vector for cancer drug etoposide. The results were interesting and the blood parameter evaluation of mice model post-exposure to drug-loaded LDHs at 5 mg/Kg and 15 mg/Kg dose showed an ameliorated hematotoxicity compared to bare drug-exposed mice. The hematology parameters in mice groups exposed to both the above-mentioned doses of bare Mg-Al LDHs showed a comparable range to that of reference points, evincing Mg-Al LDHs to be a hemocompatible vector [Zhu *et al.,* 2015].

5.3.4 Biochemistry

The biochemistry markers like creatine and protein in Zn-Al LDHs exposed to Wistar rats remained comparable to untreated rats. The other markers like albumin, glucose, cholesterol, ALT, AST, ALP level showed fluctuations but were not significantly different from the levels in control serum samples. Though fluctuations were present in the biochemical parameters, the values obtained were in similar to previous reports

on control rats [Mohamed *et al*., 2011, Nia *et al*., 2019, Mohanan *et al.,* 2021]. On similar grounds, the introduction of Mn-LDHs into rats at a dose of 0.5 mg/Kg was found to leave the albumin, ALT, creatine levels without significant alterations from normal values. The AST and ALP levels showed initial hike but got normalized within 3 days suggesting a non-toxic response [Xie *et al.,* 2020]. Also, the ALT, AST and ALP levels of Taconic-wide type mice were within normal range after intraperitoneal administration of Mg-Al LDHs (upto 15mg/Kg dose) pointing towards a non-destructive interaction [Zhu *et al.,* 2015]. A similar pattern in AST and ALT levels was also reported by Wang *et al* when Mg-Al LDHs was injected to BALB/c via i.p route [Wang *et al.,* 2019].

5.3.5 Urine analysis

The urine analysis showed that different parameters like the pH and protein of urine samples post-exposure were normal compared to the samples collected from unexposed rats. The regular pattern in other markers like glucose, ketones, blood *etc.,* draws to the inference that a single dose of 10mg/Kg of Zn-Al LDHs did not alter the normal functioning of kidneys in exposed Wistar rats. In a previous work, oral administration of Mg-Al LDHs into Balb/c mice showed an unaltered kidney function post-exposure, as estimated from the uric acid and blood urea nitrogen in blood. The above-mentioned study also deduced that oral dosage upto 2000mg/Kg of Mg-Al LDHs did not cause any significant change in different kidney function markers. The result also suggested the test material to be without any acute-oral toxicity/ harm to kidney [Yu *et al.,* 2013].

5.3.6 Gross pathology

Gross pathology examination of the Zn-Al LDHs exposed rats showed no abnormalities compared to the saline-injected rats. There were no lesions or colour changes observed in major organs like the liver, brain, kidney and spleen. Zn-Al LDHs in bare and composite form when orally introduced to Sprague-Dawley rats at different

doses (500 mg/Kg and 5mg/Kg) showed comparable results. Any detectable changes in gross pathology were not observed for the treated rat groups, suggesting an absence of acute toxic response [Kura *et al.,* 2014].

5.3.7 Organ weight

Changes in organ weight indices are regarded as indicative of toxic responses. Therefore, changes in organ weight post-exposure are monitored and considered an important checkpoint in the nanoparticle *in-vivo* toxicity assessments [Hong *et al.,* 2013]. With the suspect of organ-specific targeted toxicity, major organs including liver, brain, kidney and spleen were collected post-sacrifice. The organ weight of the collected organs from rats after 3-, 7- and 14-days Zn-Al LDHs exposure did not show any significant variation in organ weight compared to rats exposed to saline alone. The comparable organ weight figures in exposed and unexposed rats indicate an absence of detectable toxic responses. Another type of LDHs, when orally exposed to mice model also showed a similar response pattern [Yu *et al.,* 2013]. All major organs including brain, liver, heart, kidney, intestine, spleen, lung and stomach when collected and weighed after 14 days of Mg-Al LDHs exposure via oral route showed insignificant differences. The organ weight/ body weight indices for different doses (5 mg/Kg, 50 mg/Kg, 300 mg/Kg and 2000 mg/Kg) in exposed mice groups were comparable for all the tested organs. The results were conclusive of non-toxic response in mice towards Mg-Al LDHs even at a high dose of 2000mg/Kg [Yu *et al.,* 2013].

5.3.8 Anti-oxidant assays

5.5.8.1 Protein level

The total protein level in the liver and brain showed a slight decrease on 3rd and 7th day, and got normalized on the 14th-day of examination. The variation observed was insignificant compared to the control group values. Therefore, the variation could be considered an adaptive mechanism opted and imply an absence of remarkable toxic

retort to Zn-Al LDHs exposure. Very few literature sources screening the effect of LDHs on anti-oxidants at the *in-vivo* level are available. A previous study using another type of LDHs, Co-Cd-Fe LDHs to be specific, showed contrasting results. A significant drop in total protein content was observed in soft tissue from the snail model exposed to Co-Cd-Fe LDHs [Tawab *et al.,* 2022]. The contrast observed could be as part of different parameters influencing the anti-oxidant behavior post-exposure. In fact, Mg-Al LDHs showed varied oxidative stress responses in mouse neuroblastoma cells when exposed to LDHs of varying morphology [Lu *et al.,* 2015].

5.3.8.2 GSH level

GSH is a responsive factor acting against oxidative stress and potential damage thereafter. GSH acts as a non-enzymatic anti-oxidant defensive against oxidative stress [Tewab *et al.,* 2022]. For the present study, the deviations in GSH levels throughout the experimental period were insignificant in comparison to the control. The fluctuation observed in the GSH level could be regarded as a defensive response of the body against a foreign factor. Previously, GSH level was accounted for Wistar rat model exposed to organo-modified montmorillonite (type of 2D clay) exposed repeatedly for 90 days at daily high dose of 40mg/Kg and found to be insignificantly varied compared to normal unexposed rats. The findings also proposed a non-toxic interaction at the organ level of Wistar rats with clay particles [Maisanaba *et al.,* 2014].

5.3.8.3 LPO

LPO is one of the major mechanisms of action taking place onset of oxidative stress. Henceforth, LPO turns out to be a major marker for toxicity estimation. Induction of oxidative stress is widely observed after-effect of nanoparticle exposure and therefore, the extent of LPO on nanoparticle treatment is evaluated for getting insight into the toxicity potential at both *in-vitro* and *in-vivo* levels [Dinischiotu *et al.,* 2013]. Estimating the level of MDA, a byproduct of LPO is an opted way of assessing the extent of LPO [Potter *et al.,* 2011]. MDA levels in liver and brain sections procured

from Zn-Al LDHs exposed Wistar rats did not show any significant deviation compared to saline exposed control group in the present study, implying an absence of remarkable LPO induction. Previously, oxidative stress in liver mitochondria procured from Sprague Dawley rats subjected to Zn-Al-NO_3 LDHs exposure was estimated by Jumenez *et al,*. The group reported that Zn-Al-NO_3 LDHs exposure did not elevate LPO in tested system and was comparable to that of the control group [Juménez *et al.,* 2020].

5.3.9 Splenocyte proliferation

Spleen is one of the major target organs for foreign compounds entering the body. The changes in weight, pathology and proliferation capacity of spleen are indicators of immunotoxicity [Jong *et al.,* 2007]. Literature screening shows that liver and spleen remain common prime targets during nanoparticle-induced toxicity specifically in cases triggered via oxidative stress [Zhou X *et al.,* 2019]. For example, the most explored 2D material- graphene showed an accumulating tendency in liver and spleen. Small-sized graphene sheets, when administered intravenously into mice model were found to accumulate in the spleen and liver [Jasim *et al.,* 2021]. An important concern arising from accumulation in the spleen is the increase in splenocyte proliferation on nanoparticle exposures, accounting for the activation of immunotoxicity. Reduced graphene- PEG functionalized was found to increase the proliferation tendency of the spleen on repeated exposure in mice as an immunotoxic response [Syama *et al.,* 2017]. With the background of 2D materials causing immune response stimulation, the immunotoxicity concerns on Zn-Al LDHs were determined by splenocyte proliferation assay. The single dose of 10mg/Kg of Zn-Al LDHs did not elevate the splenocyte proliferation capacity in Wistar rats, eliminating chances of inflammatory/ immunotoxic reaction post-exposure.

5.3.10 Biodistribution

A bigger concern associated with the nanoparticles is their fate once they enter the body, *i.e* the chances or extent of accumulation in different organs. Nanoparticles tend to be localized in different organs depending on various parameters like nanoparticle properties, exposure-route, physiological factors *etc*., [Almeida *et al*., 2015]. Many past works point out that nanoparticles accumulate over different tissues/ organs, primarily in liver, kidney, spleen, lungs, intestine, stomach, brain, skin and bone *etc*., [Khlebtsov *et al.,* 2011, Almeida JPM *et al.,* 2011]. The accumulation of nanoparticles may create unwanted responses, disturb normal functioning, and cause organ harm and toxicity [Wei Y *et al.,* 2018]. Ideally, compatible nanoparticles for biomedical applications should show low accumulation and be cleared out from the body once the purpose is met. So much effort is taken to track the nanoparticle distribution on exposure before clinical applications. Some of the earlier works have tried to identify the possible target organs of accumulation after exposure [Choi *et al.,* 2009, Chung *et al.,* 2013]. Previously, fluorescent-labeled Mg-Al LDHs were intraperitoneally injected into mice at a dose of 500mg/Kg continuously for 5 days to study the distribution pattern and identify the possible target organs. The Mg-Al LDHs were found mostly in liver, kidney and spleen (Choi *et al* 2009]. For the present study, zinc or aluminum content in kidney and brain was not increased post-exposure to Zn-Al LDHs. The ion concentrations in the liver on 3rd, 7th and 14th day of exposure were also not significantly different from the control samples. The blood samples also didn't show any significant increase in ion content. The ICP results eliminate chances of significant accumulation of Zn-Al LDHs in Wistar rats when injected with a dose of 10mg/Kg intraperitoneally. A similar response was previously reported for another type of LDHs- Mg-Al LDHs, when orally given to mice model. The biodistribution of the test sample was reported to have an insignificant difference compared to unexposed mice [Chung *et al.,* 2013].

5.3.11 Histopathology

Histopathology is a widely sort after *in-vivo* toxicity assay for making a judgement on the effect of test material exposure on tissue/ organs [Marquis BJ *et al.,* 2009]. The brain sections of Wistar rats showed similar morphological features of neurons in both Zn-Al LDHs exposed and saline-injected samples. The histology findings of the brain were in agreement with the anti-oxidant assays, which also notified insignificant differences to control. Hence, the current results point out that a single dose of Zn-Al LDHs (10mg/Kg) does not change the normal histology of the brain in Wistar rats upon i.p exposure. The histographs of the spleen contained its characteristic histological features (red and white pulp), without any detectable disintegration compared to spleen sections from saline-injected rats. The splenocyte proliferation assay as previously discussed also revealed that the current dose of Zn-Al LDHs did not affect the normal functioning of the spleen. The histopathology findings also indicate that the Zn-Al LDHs did not distort the normal hematology of the spleen. Furthermore, the collected kidney sections were also showing normal features without any evident contrast between particle exposed and unexposed samples. Henceforth, as per the histogram images, Zn-Al LDHs when intraperitoneally injected into Wistar rats did not make any distinguishable alteration to the regular structural features of the kidney. Histopathology evaluation indicated that there is no lesions in brain, spleen and kidney. The results are also in agreement with the findings on other types of LDHs like Mg-Al LDHs, Mn-Al LDHs *etc.,* [Yan *et al.,* 2017, Xie *et al.,* 2020]. Histopathological examination of different organs of rat models intravenously injected with Mn-Al LDHs showed normal histological structure. The liver, kidney, spleen, heart and lungs procured from the treated rat group displayed no detectable inflammation or toxicity and were very similar to PBS-injected rats [Xie *et al.,* 2020]. Likewise, it was reported that Mg-Al LDHs also did not cause any histological changes in all major key organs specifically liver, heart, kidney, spleen and lungs of exposed mice models [Yan *et al.,* 2017]. While in another study, Mg-Al-Cl LDH intraperitoneal

administration in rats showed accumulation in lungs causing infilteration [Yan *et al.,* 2015]. In the present study, liver showed few reactive hepatocytes on the 3rd and 14th day but maintained normal architectures having central nerve, portal vein, triad *etc*., The reactive hepatocytes could be the result of an adaptive response to a foreign body. Notably, liver micrographs did not show any evidence of adverse reactions like apoptosis/ necrosis or intrusions *etc.,* The incidence of periportal infiltration were observed in one case at the end of 14th day. Further repeated administration of the material is required to clear the status.

SUMMARY AND CONCLUSION

6.1 Summary

LDHs are highly picked two-dimensional clay materials and immensely discussed when looking forward to 2D options other than graphene. The dimensionality, layered structure, interlayer space, versatility, positive surface charge, synthesis ease, possibility for wide chemical combinations, loading capacity *etc*., are attributed to assorting LDHs for different applications. Over the years, LDHs have been an attraction as catalysts, absorbents, polymer additives, drug/gene delivery vector, adjuvant, bone regeneration materials *etc*., Many successful claims have been reported on the potential applicability of various type of LDHs for clinical applications. Any translation from lab-bench to medical desk is obliged to toxicity assessment of the material to eliminate latent risk. The present study focused on the compatibility evaluation of Zn-Al LDHs, a widely explored LDHs for biomedical applications and yet meagre profile accessible on its possible toxicity. The Zn-Al LDHs was synthesized by low-temperature nucleation followed by hydrothermal treatment so as to avoid overgrowth of LDHs, a demerit associated with LDHs synthesis. The opted strategy helped control the particle size to <200 nm and size distribution. Zn-Al LDHs was fabricated by co-precipitating nitrate salts of zinc and aluminium and the reaction parameters were optimized to yield average ~ 102 nm sized LDHs. The prepared LDHs was characterized by TEM, XRD, FT-IR, Raman spectra, DLS, TGA, DTA and zeta-potential.

The synthesized LDHs was initially evaluated for its compatibility when in interaction with L929 cells. The cellular uptake of the exposed LDHs by L929 cells was estimated by flow cytometry analysis. The cell viability and mitochondrial activity of L929 cells after exposure to Zn-Al LDHs were analyzed using MTT assay. The oxidative stress-inducing potential of the prepared Zn-Al LDHs particles was approximated using DCFH-DA assay. The fate of different organelles including lysosomes, cytoskeleton, nuclei after exposure to Zn-Al LDHs was examined by using different organelle-

specific fluorescent dye staining. The mechanism of cell death was also examined by Annexin-PI assay. Inorder to check on the potential leach-out toxicity, cell viability and ROS production in L929 cells after treatment with Zn-Al LDHs extracts were estimated. In the context of LDHs being widely explored for bone regeneration scaffold applications, the interactions of prepared Zn-Al LDHs with HOS cells were monitored. The cell viability, morphology changes, oxidative stress, lactate dehydrogenase release, mitochondrial activity, lysosomal stability, cytoskeleton structure, nuclei integrity in HOS cells post-exposure to Zn-Al LDHs was marked to address the toxicity concerns.

To understand the interaction of Zn-Al LDHs in *in-vivo*, the synthesized material at a dose of 10mg/Kg was intraperitoneally injected to the Wistar rat model. The test animals were monitored for any clinical/ behavioural abnormalities due to Zn-Al LDHs exposure. The animals were sacrificed on 3^{rd}, 7^{th} and 14^{th} day. The body weights on the day of sacrifice were noted to check for any possible toxic response. Liver, kidney, brain and spleen were collected from the experimental rats and corresponding organ weights were taken down. Blood and urine from the study rats were analyzed to detect any parameter changes. The anti-oxidant assays were carried out for brain and liver. The probability of immunotoxicity was checked with splenocyte proliferation assay. The biodistribution in liver, kidney, brain and blood was estimated to understand the chances of accumulation of Zn-Al LDHs at *in-vivo* level. The effect of Zn-Al LDHs on important organs was examined by histopathological evaluation of liver, kidney, brain and spleen.

6.2 Methodology adopted

- Synthesis of Zn-Al LDHs
- Zn-Al LDHs was synthesized via co-precipitation method with nucleation at ice-cold condition and hydrothermal growth at 80^0 C.
- Physico-chemical characterization
- Nano-size and morphology characterization by TEM.
- Crystal structure identification by XRD.
- Hydrodynamic size was calculated with DLS analysis.
- Functional groups were identified by FT-IR spectra.
- Chemical groups were characterized using Raman spectroscopy.
- Thermal degradation profile was found with TGA analysis.
- Thermal changes were recognized using DTA analysis.
- Surface charge was estimated using Zeta potential analysis.
- Interactions with L929 cells.
- Cellular uptake of Zn-Al LDHs confirmed using flow cytometry.
- Cell viability and metabolic activity evaluation by MTT assay.
- Lysosomal activity and cell viability check using NRU and acridine orange staining assay.
- Oxidative stress was estimated with DCFH-DA assay.
- The cytoskeletal and nuclei integrity was labeled using rhodamine-phalloidin and DAPI fluorescent dyes respectively.
- The Live/dead assessment was done using Calcein AM/PI staining.
- Chances of apoptosis and DNA damage were marked using DNA laddering assay.
- Apoptosis/ Necrosis cells were stained using Annexin/PI fluorescent dyes and quantified using flow cytometry analysis.
- The leach-out toxicity was estimated using MTT and NRU assays.

- Interactions with HOS cells

- Cell viability and metabolic activity assessed using MTT assay.
- Mitochondrial activity marked using JC1 staining.
- Morphological changes evaluated by Coomassie brilliant blue and Giemsa staining.
- ROS production was estimated using DCFH-DA assay.
- The release of lactate dehydrogenase enzyme was estimated using a lactate dehydrogenase enzyme assay kit.
- The lysosomal integrity post-treatment was analyzed using AO staining.
- Integrity of the cytoskeleton and nuclei was found using counter staining with rhodamine-phalloidin and DAPI.
- Live/dead cells trend after particle exposure was estimated using AO/EtBr staining.
- Effect of Zn-Al LDHs on nuclei and its probability to trigger apoptosis was checked using a DNA laddering assay.

- Toxicity evaluation of 2D Zn-Al layered double hydroxides in rat model

- For the *in-vivo* toxicity assessment, 12 Wistar rats were divided into 4 groups with 3 in each. The first group was intraperitoneally injected with saline whereas the other three groups were administrated with 10mg/Kg of Zn-Al LDHs via i.p. The 2^{nd}, 3^{rd} and 4^{th} group rats were sacrificed on 3^{rd}, 7^{th} and 14^{th} day.
- The experimental animals were monitored visually for the entire study period inorder to identify any clinical/ behavioural changes post-exposure.
- The body weights were also documented for identifying stress-induced toxic response.
- Blood was collected from all animals and was subjected to hematology and biochemistry analysis.
- The urine collected on respective days was evaluated for various markers.

- Liver, spleen, kidney and brain were collected from test animals after euthanization on 3^{rd},7^{th} and 14^{th} day. The gross pathological evaluation was done on sacrifice.
- The weights of collected organs were also listed to screen any organ-specific or stress-induced toxicity.
- The oxidative stress and adaptive response post-exposure were evaluated by estimating the level of LPO, GSH and total proteins in liver and brain.
- Immunotoxicity was monitored via splenocyte proliferation assay.
- The biodistribution of Zn-Al LDHs in blood, liver, brain and kidney was estimated using ICP-MS analysis.
- Organs collected were H & E stained for histopathology examination.

6.3 Major Outcomes

- Zn-Al LDHs was successfully synthesized with hexagonal morphology and an average size of ~102 nm.
- The synthesized Zn-Al LDHs was well characterized using TEM, XRD, TGA, DTA, zeta potential, FT-IR, Raman spectra and DLS.
- The prepared Zn-Al LDHs was internalized in a dose-dependent manner by L929 cells.
- MTT results showed that Zn-Al LDHs exhibited non-toxic interactions with mitochondria and overall good compatibility with L929 cells.
- The L929 cells succeeded in maintaining good cell viability post-exposure to upto 160 µg/ml of Zn-Al LDHs.
- The lysosomal integrity of L929 remained undisturbed on treatment with Zn-Al LDHs.
- All the tested concentrations of Zn-Al LDHs were found not to cause any rupture in the cytoskeleton of L929 cells.
- Zn-Al LDHs did not source any nuclear disintegration in L929 cells exposed to 160 µg/ml dose.
- Zn-Al LDHs showed a small increase in cell proportions at the early apoptotic stage at higher dose concentrations but the difference was insignificant compared to control.
- The leach-out toxicity from 24 h and 72 h extracts of Zn-Al LDHs was found to be negligible.
- The Zn-Al LDHs exhibited cytocompatible interaction with HOS cells.
- The metabolic function of HOS cells remained active when exposed to 10-160 µg/ml concentrations of Zn-Al LDHs.
- Zn-Al LDHs do not significantly interfere with the mitochondrial activity of HOS cells upto 160 µg/ml.

- No significant oxidative stress was induced by Zn-Al LDHs in HOS cells for the selected concentrations and upto 24 h exposure.
- Zn-Al LDHs does not cause harm to cytoskeleton of HOS cells.
- No evident genotoxicity or apoptosis was seen in Zn-Al LDHs exposed HOS cells.
- The Wistar rats injected with Zn-Al LDHs did not show any clinical signs of toxicity.
- Slight alteration was found in hematological values, however all the values are coming under normal range.
- Albumin, Protein and Creatinine levels in serum were found to be comparable to control.
- Cholesterol, glucose, AST, ALT and ALP levels showed fluctuations as an adaptive response to Zn-Al LDHs exposure, without any significant variation.
- Histopathology evaluation indicated that there is no lesions in brain, spleen and kidney. However periportal infiltration were observed in one case at the end of 14^{th} day.
- Parameters of urine analysis were comparable to control.
- No significant immunotoxicity was induced by Zn-Al LDHs at the tested dose in Wistar rats.
- No significant variation in oxidative stress.
- Biodistribution indicated the presence of Zn and Al in brain, kidney, liver and blood which is comparable to control group.

6.4 Conclusion

Zn-Al LDHs was synthesized in an economical and eco-friendly way by adopting the co-precipitation method. The synthesized Zn-Al LDHs showed an average particle size of ~102 nm in TEM analysis. The XRD analysis confirmed the LDHs structure to be a hexagonal lattice with rhombohedral 3R symmetry. All the characteristic peaks for LDHs, specifically hydroxyl, H_2O bending vibration of interlayer water, and intercalated carboxylate anion were confirmed by FT-IR spectroscopy. Raman spectroscopy further confirmed the functional groups of LDHs. The TGA analysis confirmed the temperature-dependent degradation profiling of LDHs and conversion of lattice structure to mixed metal oxide (MMO) at higher temperatures. LDHs, possessed positive charge as part of the partial substitution of Al^{3+} ions in between Zn^{2+} ions.

As per the cellular uptake analysis Zn-Al LDHs were internalized by L929 cells in a dose-dependent manner. L929 and HOS cells exhibited cytocompatible interaction upto 160 µg/ml concentration post-internalization. The cell viability assays were testaments to the non-toxic interaction of Zn-Al LDHs with HOS and L929 cells. No change in characteristic morphology was observed on exposure to LDHs. The structural integrity was not compromised on LDHs exposure and the actin filaments were seen intact post-exposure. Henceforth, it was concluded that Zn-Al LDHs for the selected concentrations did not cause any morphological or structural toxicity. The ROS production was similar to that of control values in L929 and HOS. The absence of a remarkable hike in ROS on treatment with the synthesized Zn-Al LDHs rules out chances of oxidative stress-induced toxicity, one of the major mechanisms of nanoparticle-induced toxicity. There was no remarkable decline in mitochondrial or lysosomal activity in exposed L929 and HOS cells, so no evident toxic mechanism involving mitochondria or lysosomes was involved with Zn-Al LDHs exposure. Also, Zn-Al LDHs did not bring about an alarming

toxic interaction at the nuclear level. The cells in the early apoptotic population were found to increase on Zn-Al LDHs treatment at higher concentrations but no significant difference was noticed. The annexin-PI mediated analysis and DNA laddering revealed that Zn-Al LDHs till the selected concentration and exposure time of 24 h do not induce significant cell death. The overall *in-vitro* studies suggest that 160µg/ml to be a safe concentration for HOS and L929 cells and exhibits non-toxic interactions.

Single dose of 10mg/Kg of Zn-Al LDHs injected into Wistar rats via i.p route did not cause any behavioural changes. The experimental rats showed no gross abnormality/ observable lesions. Furthermore, the Zn-Al LDHs administration did not alter the blood and urine parameters. At the current dose, no evident alteration in anti-oxidant levels were induced in Wistar rats' post-exposure to Zn-Al LDHs. Significant accumulation of Zn and Al in brain, kidney, liver and blood were not observed in exposed test groups as per the biodistribution study. Zn- Al LDHs showed no adverse effect in kidney, spleen, and brain. At the end of 14^{th} day, there was an incidence of infilteration in one case of liver tissue. Additional repeated exposure of Zn-Al LDHs will be required to confirm this observation. Further long-term toxicity studies will be required to declare the Zn-Al LDHs to be a safe nanomaterial for biomedical applications.

6.5 Future perspectives

- Repeated exposure toxicity studies.
- Fabrication of Zn-Al LDHs-based scaffold for bone regeneration.
- Controlled release kinetics of Zn-Al LDHs for drug delivery applications.

REFERENCES

Abdel-Tawab H, Ibrahim AM, Hussein T, Mohamed F (2022) Mechanism of action and toxicological evaluation of engineered layered double hydroxide nanomaterials in Biomphalariaalexandrina snails. *Environ Sci Pollut Res 29*(8), 11765-11779.

Abderrazek K, FriniSrasra N, Srasra E (2017) Synthesis and Characterization of [Zn-Al] Layered Double Hydroxides: Effect of the Operating Parameters. *J Chin Chem Soc*. *64*(3), 346-353.

Albers CE, Hofstetter W, Siebenrock KA, Landmann R, Klenke FM. (2013) *In-vitro* cytotoxicity of silver nanoparticles on osteoblasts and osteoclasts at antibacterial concentrations. *Nanotoxicology 7*(1), 30-36.

Almeida JPM, Chen AL, Foster A, Drezek R (2011). *In-vivo* biodistribution of nanoparticles. *Nanomedicine 6*(5), 815-835.

Amini AR, Laurencin CT, Nukavarapu SP (2012). Bone tissue engineering: recent advances and challenges. *Crit. Rev. Biomed. Eng* 40(5).

Andrade KN, Pérez AMP, Arízaga GGC (2019) Passive and active targeting strategies in hybrid layered double hydroxides nanoparticles for tumor bioimaging and therapy. *Appl Clay Sci*, 181, 105214.

Aranda A, Sequedo L, Tolosa L, Quintas G, Burello E, Castell J V, Gombau L (2013) Dichloro-dihydro-fluorescein diacetate (DCFH-DA) assay: a quantitative method for oxidative stress assessment of nanoparticle-treated cells. *Toxicol in vitro 27*(2), 954-963.

Ardlin BI, Lindholm-Sethson B, Dahl JE (2009) Corrosion of dental nickel–aluminum bronze with a minor gold content-mechanism and biological impact. *J Biomed Mater Res B Appl Biomater 88*(2), 465-473.

Asha Rani PV, Low Kah Mun G, Hande MP, Valiyaveettil S (2009) Cytotoxicity and genotoxicity of silver nanoparticles in human cells. *ACS nano*, *3*(2), 279-290.

Awasthi A, Jadhao P, Kumari K (2019) Clay nano-adsorbent: structures, applications and mechanism for water treatment. *SN Appl Sci* 1(9), 1076.

Baek M, Lee JA, Choi SJ (2012) Toxicological effects of a cationic clay, montmorillonite in vitro and *in-vivo*. *Mol Cell Toxicol* 8(1), 95-101.

Balcomb B, Singh M, Singh S (2015) Synthesis and characterization of layered double hydroxides and their potential as nonviral gene delivery vehicles. *Chemistry Open 4*(2), 137-145.

Bexiga MG, Varela JA, Wang F, Fenaroli F, Salvati A, Lynch I, Dawson K A (2011) Cationic nanoparticles induce caspase 3-, 7-and 9-mediated cytotoxicity in a human astrocytoma cell line. *Nanotoxicology*, *5*(4), 557-567.

Britvin SN, 2008. Structural diversity of layered double hydroxides. In *Minerals as advanced materials I,* Springer, Berlin, Heidelberg, pp. 123-128.

Bukhtiyarova MV (2019) A review on effect of synthesis conditions on the formation of layered double hydroxides. *J of Solid State Chem*, 269, 494-506.

Campana V, Milano GIUSEPPE, Pagano E, Barba M, Cicione C, Salonna G, Logroscino G (2014) Bone substitutes in orthopaedic surgery: from basic science to clinical practice. J Mater Sci Mater Med *25*(10), 2445-2461.

Cao Y, Li G, Li X (2016) Graphene/layered double hydroxide nanocomposite: Properties, synthesis, and applications. *Chem Eng J 292*, 207-223.

Cao F, Wang Y, Ping Q, Liao Z (2011) Zn–Al–NO3-layered double hydroxides with intercalated diclofenac for ocular delivery. *Int J pharm*, 404(1-2), 250-256.

Casey A, Herzog E, Davoren M, Lyng FM, Byrne HJ, Chambers G (2007) Spectroscopic analysis confirms the interactions between single walled carbon nanotubes and various dyes commonly used to assess cytotoxicity. *Carbon*, *45*(7), 1425-1432.

Chaicherd S, Killingsworth MC, Pissuwan D (2019) Toxicity of gold nanoparticles in a commercial dietary supplement drink on connective tissue fibroblast cells. *SN Appl Sci*, *1*(4), 1-8.

Chazotte B (2010). Labeling cytoskeletal F-actin with rhodamine phalloidin or fluorescein phalloidin for imaging. *Cold Spring Harbor Protocols*, *2010*(5), pdb-prot4947.

Chazotte B (2011). Labeling nuclear DNA using DAPI. *Cold Spring Harbor Protocols*, *2011*(1), pdb-prot5556.

Chen C, Gunawan P, Lou XW, Xu R (2012) Silver nanoparticles deposited layered double hydroxide nanoporous coatings with excellent antimicrobial activities. *Adv Funct Mater 22*(4), 780-787.

Chimene D, Alge DL, Gaharwar AK (2015) Two-dimensional nanomaterials for biomedical applications: emerging trends and future prospects. *Adv Mater 27*(45), 7261-7284.

Chin I-J, Thurn-Albrecht T, Kim H-C, Russell TP, Wang J (2001) On exfoliation of montmorillonite in epoxy. *Polymer* 42:5947–52.

Choi SJ, Oh JM, Choy JH (2008) Safety aspect of inorganic layered nanoparticles: Size-dependency in vitro and *in-vivo*. *J Nanosci Nanotech 8*(10), 5297-5301.

Choi S J, Oh JM, Choy JH (2009) Toxicological effects of inorganic nanoparticles on human lung cancer A549 cells. *J Inorg Biochem* 103(3), 463-471

Choi SJ, Paek HJ, Yu J (2015) Oxidative stress by layered double hydroxide nanoparticles via an SFK-JNK and p38-NF-κB signaling pathway mediates induction of interleukin-6 and interleukin-8 in human lung epithelial cells. *Int J nanomedicine 10*, 3217.

Ciniglia C, Pinto G, Sansone C, Pollio A (2010) Acridine orange/Ethidium bromide double staining test: A simple In-vitro assay to detect apoptosis induced by phenolic compounds in plant cells. *Allelopathy J* 26(2), 301-308.

Cocheci L, Lupa L, Lazău R, Vodă R, Pode R (2019) Zinc recovery from waste zinc ash-a new "green" route for the preparation of Zn-Al layered double hydroxide used for molybdate retention. *J Alloys Compd,* 787, 332-343.

Cui GJ, Xu XY, Lin YJ, Evans DG, Li DQ (2010) Synthesis and UV Absorption Properties of 5, 5′-Methylenedisalicylic Acid-Intercalated Zn− Al Layered Double Hydroxides. *Ind Eng Chem Res* 49(2), 448-453.

Cui X, Liang T, Liu C, Yuan Y, Qian J (2016) Correlation of particle properties with cytotoxicity and cellular uptake of hydroxyapatite nanoparticles in human gastric cancer cells. *Mater Sci Eng C* 67, 453-460.

Cui ZK, Kim S, Baljon JJ, Wu BM, Aghaloo T, Lee M (2019) Microporous methacrylated glycol chitosan-montmorillonite nanocomposite hydrogel for bone tissue engineering. *Nat Commun* 10(1), 1-10.

Cunha VRR, de Souza R B, da Fonseca Martins AMCRP, Koh IHJ, Constantino VRL (2016) Accessing the biocompatibility of layered double hydroxide by intramuscular implantation: Histological and microcirculation evaluation. *Sci Rep 6*(1), 1-10.

De Jong WH, & Van Loveren, H (2007) Screening of xenobiotics for direct immunotoxicity in an animal study. *Methods*, *41*(1), 3-8.

De Stefano D, Carnuccio R, Maiuri, MC (2012) Nanomaterials toxicity and cell death modalities. *J Drug Deliv*, 1-14.

Dinischiotu A, Stanca L, Gradinaru D, Petrache SN, Radu M, Serban AI (2013) Lipid peroxidation due to in vitro and *in-vivo* exposure of biological samples to nanoparticles. In *Oxidative Stress and Nanotechnology* Humana Press, Totowa, NJ, pp. 155-164.

Doktorovova S, Silva AM, Gaivão I, Souto EB, Teixeira JP, Martins-Lopes P (2014) Comet assay reveals no genotoxicity risk of cationic solid lipid nanoparticles. *J Appl Toxicol* 34(4), 395-403.

Donnadio A, Bini M, Centracchio C, Mattarelli M, Caponi S, Ambrogi V, Nocchetti M (2021) Bioinspired reactive interfaces based on layered double hydroxides-Zn rich hydroxyapatite with antibacterial activity. *ACS Biomater Sci Eng 7*(4), 1361-1373.

Duan X and Evans D.G eds., (2006) *Layered double hydroxides* (Vol. 119). Springer Science & Business Media.

Elefantova K, Lakatos B, Kubickova J, Sulova Z, Breier A (2018) Detection of the mitochondrial membrane potential by the cationic dye JC-1 in L1210 cells with massive overexpression of the plasma membrane ABCB1 drug transporter. *Inter J Mol Sci*, *19*(7), 1985.

Enderami SE, Shafiei SS, Rostamian A (2022) Evaluation of osteogenic differentiation of bone marrow-derived mesenchymal stem cell on highly porous polycaprolactone scaffold reinforced with layered double hydroxides nanoclay. *Front Bioeng Biotech* 232,1-17.

Evans DG, & Slade RC (2006) Structural aspects of layered double hydroxides. In *Layered double hydroxides.* Springer-Verlag Berlin Heidelberg, 1-87.

Experiments on Animals (203) Committee for the Purpose of Control and Supervision on Experiments on Animals (CPCSEA) guidelines for laboratory animal facility. Indian J Pharmacol 35:257–74

Foldbjerg R, Dang DA, Autrup H (2011) Cytotoxicity and genotoxicity of silver nanoparticles in the human lung cancer cell line, A549. *Arch Toxicol* 85(7), 743-750.

Frohlich E (2013) Cellular targets and mechanisms in the cytotoxic action of non-biodegradable engineered nanoparticles. *Curr Drug Metab* 14(9), 976-988.

Frost R L, Soisnard A, Voyer N, Palmer S J, Martens W N (2009) Thermo-Raman spectroscopy of selected layered double hydroxides of formula $Cu_6Al_2(OH)_{16}CO_3$ and $Zn_6Al_2(OH)_{16}CO_3$. *Journal of Raman Spectroscopy: An International Journal for Original Work in all Aspects of Raman Spectroscopy, Including Higher Order Processes, and also Brillouin and Rayleigh Scattering*, 40(6), 645-649.

Fu L, Yan Z, Zhao Q, Yang H (2018) Novel 2D nanosheets with potential applications in heavy metal purification: A review. *Adv Mater Interfaces* 5(23), 1801094.

Gaharwar AK, Cross LM, Peak CW, Gold K, Carrow JK, Brokesh A, Singh KA (2019) 2D nanoclay for biomedical applications: regenerative medicine, therapeutic delivery, and additive manufacturing. *Adv Mater*, *31*(23), 1900332.

Gaines RV, Dana JD, Dana ES (1997) *Dana's new mineralogy: The system of mineralogy of James Dwight Dana and Edward Salisbury Dana*. Wiley.

Gazaryan IG, Krasinskaya IP, Kristal BS, Brown AM (2007) Zinc irreversibly damages major enzymes of energy production and antioxidant defense prior to mitochondrial permeability transition. *J Biol Chem*, *282*(33), 24373-24380.

Goh KH, Lim TT, Dong Z (2008) Application of layered double hydroxides for removal of oxyanions: a review. *Water Res*, *42*(6-7), 1343-1368.

Gong T, Xie J, Liao J, Zhang T, Lin S, Lin Y (2015) Nanomaterials and bone regeneration. *Bone Res 3*(1), 1-7.

Granchi D, Ciapetti G, Savarino L, Cavedagna D, Donati M E, Pizzoferrato A (1996) Assessment of metal extract toxicity on human lymphocytes cultured in vitro. *J Biomed Mater Res 31*(2), 183-191.

Gunjakar JL, Kim TW, Kim HN, Kim IY, Hwang SJ (2011) Mesoporous layer-by-layer ordered nanohybrids of layered double hydroxide and layered metal oxide: highly active visible light photocatalysts with improved chemical stability. *J American Chem Soc 133*(38), 14998-15007.

Gürgit İ, Gökmen O, Kocatürkmen A, Namli İ, Günnur ONAK, Karaman O (2020) Proliferation and Viability of L929 Cells in Synthetic Flexible Bone Grafts. In *2020 Medical Technologies Congress (TIPTEKNO)* IEEE, 1-4.

Gutiérrez-Cruz A, Ruiz-Hernández AR., Vega-Clemente JF, Luna-Gazcón, DG, Campos-Delgado J (2022) A review of top-down and bottom-up synthesis methods for the production of graphene, graphene oxide and reduced graphene oxide. *Journal of Materials Science*, *57*(31), 14543-14578.

Harshitha B, Subhada B, Mustafa M, Solanki H, Safiya NAM, Tiwari RVC (2019) DNA laddering to evaluate cytogenetic damage in patients with periodontitis. *J Inter Soc Prev & Commun Dent 9*(5), 486.

Hong TK, Tripathy N, Son HJ, Ha KT, Jeong HS, Hahn YB (2013) A comprehensive in vitro and *in-vivo* study of ZnO nanoparticles toxicity. *J Mater Chem B 1*(23), 2985-2992.

Ho-Shui-Ling A, Bolander J, Rustom LE, Johnson AW, Luyten FP, Picart C (2018) Bone regeneration strategies: engineered scaffolds, bioactive molecules, and stem cells current stage and future perspectives. *Biomater* 180, 143-162.

Hu T, Gu Z, Williams G R, Strimaite M, Zha J, Zhou Z, Liang R (2022) Layered double hydroxide-based nanomaterials for biomedical applications. *Chem Soc Rev,* 51**,** 6126-6176.

Huo J, Min X, Dong Q, Xu S, Wang Y (2022) Comparison of Zn–Al and Mg–Al layered double hydroxides for adsorption of perfluorooctanoic acid. *Chemosphere*, *287*, 132297.

International Organization for Standardization (2009) Biological evaluation of medical devices - Part Tests for *in-vitro* cytotoxicity. ISO 10993-5. Geneva, Switzerland, 1–34.

Izbudak B, Cecen B, Anaya I, Miri A K, Bal-Ozturk A, Karaoz E (2021) Layered double hydroxide-based nanocomposite scaffolds in tissue engineering applications. *RSC Adv*, *11*(48), 30237-30252.

Jasim DA, Newman L, Rodrigues AF, Vacchi IA, Lucherelli MA, Lozano N, Kostarelos K (2021) The impact of graphene oxide sheet lateral dimensions on their pharmacokinetic and tissue distribution profiles in mice. *J Cont Release*, 338, 330-340.

Jiang Q, Li X, Cheng S, Gu Y, Chen G, Shen Y, Cao YI (2016) Combined effects of low levels of palmitate on toxicity of ZnO nanoparticles to THP-1 macrophages. *Environ Toxicol Pharmacol 48*, 103-109.

Jin W, Park DH (2019) Functional layered double hydroxide nanohybrids for biomedical imaging. *Nanomaterials 9*(10), 1404.

Johnson TE, Martens W, Frost RL, Ding Z, Theo Kloprogge J (2002) Structured water in hydrotalcites of formula $Mg_xZn_{6-x}Al_2$ (OH)16(CO_3)·4H_2O: a Raman microscopic study. *J Raman Spectroscopy*, *33*(8), 604-609.

Juménez CS, Moisés FPP, Cano ME, Andrade KN, Torres ALB, Arízaga GGC (2020) Folate-and glucuronate–functionalization of layered double hydroxides containing dysprosium and gadolinium and the effect on oxidative stress in rat liver mitochondria. *Heliyon*, *6*(1), e03111.

Kondashevskaya, M.V. and Mkhitarov, V.A (2006) Hematological parameters in wistar rats in conditions of stress and treatment with heparin. *Neuroscience and Behavioral Physiology*, *36*, 29-34.

Kang HR, da Costa Fernandes CJ , da Silva RA, Constantino VRL, Koh IHJ, Zambuzzi WF (2018) Mg–Al and Zn–Al Layered Double Hydroxides Promote Dynamic Expression of Marker Genes in Osteogenic Differentiation by 374Modulating Mitogen-Activated Protein Kinases. *Adv healthcare mater*, *7*(4), 1700693.

Kapusetti G, Misra N, Singh V, Kushwaha RK, Maiti P (2012) Bone cement/layered double hydroxide nanocomposites as potential biomaterials for joint implant. *J Biomed Mater Res Part A 100*(12), 3363-3373.

Kaur H, Singh S, Pal, B (2021). Impact of g-C3N4 loading on NiCo LDH for adsorptive removal of anionic and cationic organic pollutants from aqueous solution. *Korean J Chem Eng*, *38*(6), 1248-1259.

Khanal S, Lu Y, Jin D, Xu S (2022) Effects of layered double hydroxides on the thermal and flame retardant properties of intumescent flame retardant high density polyethylene composites. *Fire Mater*, *46*(1), 107-116.

Khlebtsov N, Dykman L (2011) Biodistribution and toxicity of engineered gold nanoparticles: a review of *in-vitro* and *in-vivo* studies. *Chem Soc Rev*, *40*(3), 1647-1671.

Kiani M, Bagherzadeh M, Ghadiri A M, Makvandi P, Rabiee N (2022) Multifunctional green synthesized Cu–Al layered double hydroxide (LDH) nanoparticles: anti-cancer and antibacterial activities. *Sci Reports*, *12*(1), 1-14.

Kim J, Kim D, Lee KJ, Kim D, Chung KH, Choi W, An JH (2020) Effect of Nano-Montmorillonite on Osteoblast Differentiation, Mineral Density, and Osteoclast Differentiation in Bone Formation. *Nanomaterials*, *10*(2), p.230.

Kim YH, Yang X, Shi L, Lanham SA, Hilborn J, Oreffo RO, Dawson JI (2020) Bisphosphonate nanoclay edge-site interactions facilitate hydrogel self-assembly and sustained growth factor localization. *Nat commun*, *11*(1), 1-9.

Kloprogge JT, Hickey L, Frost RL (2004) The effects of synthesis pH and hydrothermal treatment on the formation of zinc aluminum hydrotalcites. *J Solid State Chem*, *177*(11), 4047-4057.

Krug HF, Wick P (2011). Nanotoxicology: an interdisciplinary challenge. *Angew Chemie International Edition*, *50*(6), 1260-1278.

Kubásek J, Vojtěch D, Jablonská E, Pospíšilová I, Lipov J, Ruml T (2016) Structure, mechanical characteristics and in vitro degradation, cytotoxicity, genotoxicity and mutagenicity of novel biodegradable Zn–Mg alloys. *Mater Sci Eng: C*, *58*, 24-35.

Kumar P, Nagarajan A, Uchil PD (2018) Analysis of cell viability by the lactate dehydrogenase assay. *Cold Spring Harbor Protocols*, *2018*(6), pdb-prot095497.

Kura AU, Ain NM, Hussein MZ, Fakurazi S, Hussein-Al-Ali SH (2014). Toxicity and metabolism of layered double hydroxide intercalated with levodopa in a Parkinson's disease model. *Inter J Mol Sci 15*(4), 5916-5927.

Kura AU, Cheah PS, Hussein MZ, Hassan Z, Tengku Azmi TI, Hussein NF, Fakurazi S (2014) Toxicity evaluation of zinc aluminium levodopa nanocomposite via oral route in repeated dose study. *Nanoscale Res lett*, *9*(1), 1-11.

Kurapati R, Kostarelos K, Prato M, Bianco A (2016) Biomedical uses for 2D materials beyond graphene: current advances and challenges ahead. *Adv Mater*, *28*(29), 6052-6074.

Kwak SY, Kriven WM, Wallig MA, Choy JH (2004). Inorganic delivery vector for intravenous injection. *Biomater*, 25(28), 5995-6001.

Ladewig K, Xu ZP, Lu GQ (2009) Layered double hydroxide nanoparticles in gene and drug delivery. *Exp Opinion Drug Deliv*, *6*(9), 907-922.

Lee JH, Chang J, Cha JH, Jung DY, Kim SS, Kim JM (2010) Anthraquinone Sulfonate Modified, Layered Double Hydroxide Nanosheets for Dye-Sensitized Solar Cells. *Chem Eur J*, *16*(28), pp.8296-8299.

Li L, Ma R, Ebina Y, Iyi N, Sasaki T (2005) Positively charged nanosheets derived via total delamination of layered double hydroxides. *Chem Mater*, *17*(17), pp.4386-4391.

Li M, Li L, Lin S (2020) Efficient antimicrobial properties of layered double hydroxide assembled with transition metals via a facile preparation method. *Chinese Chem Lett*, *31*(6), 1511-1515.

Li Q, Wang D, Qiu J, Peng F, Liu X (2018) Regulating the local pH level of titanium via Mg–Fe layered double hydroxides films for enhanced osteogenesis. *Biomat Sci*, *6*(5), 1227-1237.

Liu G, Li Q, Ni W, Zhang N, Zheng X, Wang Y, Tai G (2015) Cytotoxicity of various types of gold-mesoporous silica nanoparticles in human breast cancer cells. *Int J Nanomed* 10, 6075.

Liu J, Huang X, Li Y, Sulieman K M, He X, Sun F (2006) Facile and large-scale production of ZnO/Zn−Al layered double hydroxide hierarchical heterostructures. *J Phy Chem B 110*(43), 21865-21872.

Lu X, Qian J, Zhou H, Gan Q, Tang W, Lu J, Liu C (2011) *In vitro* cytotoxicity and induction of apoptosis by silica nanoparticles in human HepG2 hepatoma cells. *Int J Nanomed*, *6*, 1889.

Lu Y, Yan B, Liu X, Zhang Y, Zeng S, Hu H, Yang X (2015) Comparative study of oxidative stress induced by sand flower and schistose nanosized layered double hydroxides in N2a cells. *Front Bio 10*(3), 279-286.

Maisanaba S, Gutierrez-Praena D, Puerto M, Moyano R, Blanco A, Jorda M., Jos A (2014) Effects of the subchronic exposure to an organomodified clay mineral for food packaging applications on wistar rats. *Appl Clay Sci 95*, 37-40.

Manisekaran R, García-Contreras R, RasuChettiar AD, Serrano-Díaz P, Lopez-Ayuso, CA, Arenas-Arrocena MC, Acosta-Torres, L. S. (2021). 2D Nanosheets—A New Class of Therapeutic Formulations against Cancer. *Pharmaceutics*, *13*(11), 1803.

Marian M, Berman D, Nečas D, Emami N, Ruggiero, Rosenkranz, A (2022) Roadmap for 2D materials in biotribological/biomedical applications–A review. *Advances in Colloid and Interface Science*, *307*, 102747.

Marquis BJ, Love SA, Braun KL, Haynes CL (2009) Analytical methods to assess nanoparticle toxicity. *Analyst*, *134*(3), 425-439.

Marquis Bryce J, Sara A, Love Katherine L, Braun, Christy L Haynes (2009) Analytical methods to assess nanoparticle toxicity. *Analyst* 134, no.3, 425-439.

Mascolo G. and Mascolo MC (2015) On the synthesis of layered double hydroxides (LDHs) by reconstruction method based on the "memory effect". *Micropor and Mesopor Mater 214*, 246-248.

Mbeh DA, França R, Merhi Y, Zhang XF, Veres T, Sacher E, Yahia L (2012) In vitro biocompatibility assessment of functionalized magnetite nanoparticles: Biological and cytotoxicological effects. *J Biomed Mater Res A*, *100*(6), 1637-1646.

Miranda-Trevino JC, Coles CA. (2003) Kaolinite properties, structure and influence of metal retention on pH. *Appl Clay Sci* 23:133–9.

Mishra G, Dash B, Pandey S (2018) Layered double hydroxides: A brief review from fundamentals to application as evolving biomaterials. *Appl Clay Sci*, *153*, 172-186.

Mohanan, P.V., Sangeetha, V., Sabareeswaran, A., Muraleedharan, V., Jithin, K., Vandana, U. and Varsha, S.B., 2021. Safety of 0.5% hydrogen peroxide mist used in the disinfection gateway for COVID-19. *Environmental Science and Pollution Research*, *28*(47), 66602-66612.

Mohapatra L and Parida K (2016) A review on the recent progress, challenges and perspective of layered double hydroxides as promising photocatalysts. *J Mater Chem A*, *4*(28), 10744-10766.

Monteiro-Riviere NA, Inman AO, Zhang LW (2009) Limitations and relative utility of screening assays to assess engineered nanoparticle toxicity in a human cell line. *Toxicol Appl Pharm 234*(2), 222-235.

Mourdikoudis S, Pallares RM, Thanh NT (2018) Characterization techniques for nanoparticles: comparison and complementarity upon studying nanoparticle properties. *Nanoscale 10*(27), 12871-12934.

Murali A, Lokhande G, Deo KA, Brokesh A, Gaharwar AK (2021) Emerging 2D nanomaterials for biomedical applications. *Mater Today*, *50*, 276-302.

Nasiriboroumand M, Montazer M, Barani H (2018 Preparation and characterization of biocompatible silver nanoparticles using pomegranate peel extract. *J Photochem Photobio B: Bio 179*, 98-104.

Nia, R., Njang, A.S., Achidi, U.A., Tiencheu, B. and Taiwe, G.S (2019)Therapeutic Impacts of Garlic Varieties on Hyperlipidemia Induced In Male Wistar Rats.

Ohkawa H, Ohishi N and Yagi K (1979) Assay for lipid peroxides in animal tissues by thiobarbituric acid reaction. *Anal Biochem* 95: 351-358.

Padil, V. V., Kumar, K. A., Murugesan, S., Torres-Mendieta, R., Wacławek, S., Cheong, J. Y., ... & Varma, R. S. (2022). Sustainable and safer nanoclay composites for multifaceted applications. *Green Chemistry*, *24*(8), 3081-3114.

Pakrashi S, Dalai S, Prathna TC, Trivedi S, Myneni R, Raichur AM, Mukherjee A (2013) Cytotoxicity of aluminium oxide nanoparticles towards fresh water algal isolate at low exposure concentrations. *Aquatic Toxicol*, *132*, 34-45.

Pan Y, Gao Y, Hu J, Ye G, Zhou F, Yan C (2021) Montmorillonite nanosheets with enhanced photodynamic performance for synergistic bacterial ablation. *J Mater Chem B*, *9*(2), 404-409.

Pati R, Das I, Mehta RK, Sahu R, Sonawane A (2016). Zinc-oxide nanoparticles exhibit genotoxic, clastogenic, cytotoxic and actin depolymerization effects by inducing oxidative stress responses in macrophages and adult mice. *Toxicol Sci*, *150*(2), 454-472.

Paul A, Manoharan V, Krafft D, Assmann A, Uquillas JA, Shin SR, Khademhosseini A (2016) Nanoengineered biomimetic hydrogels for guiding human stem cell osteogenesis in three dimensional microenvironments. *J Mater Chem B*, *4*(20), 3544-3554.

Pavlidou S and Papaspyrides CD (2008) A review on polymer–layered silicate nanocomposites. *Progress Poly Sci 33*(12), 1119-1198.

Peng F, Wang D, Zhang D, Cao H, Liu X (2018) The prospect of layered double hydroxide as bone implants: A study of mechanical properties, cytocompatibility and antibacterial activity. *Appl Clay Sci 165*, 179-187.

Potter TM, Neun BW, Stern ST (2011) Assay to detect lipid peroxidation upon exposure to nanoparticles. In *Characterization of Nanoparticles Intended for Drug Delivery*, Humana Press, pp. 181-189.

Prestopino GG, Arrabito A, Generosi A, Mattoccia B, Paci G, Perez G, Verona-Rinati and PG Medaglia (2009) Emerging switchable ultraviolet photoluminescence in dehydrated Zn/Al layered double hydroxide nanoplatelets." *Sci Rep,* 9, no. 1, 1-12.

Railsback JG, Singh A, Pearce RC, McKnight TE, Collazo R, Sitar Z, Melechko A V (2012) Weakly charged cationic nanoparticles induce DNA bending and strand separation. *Adv Mater 24*(31), 4261-4265.

Rather HA, Jhala D, Vasita R (2019) Dual functional approaches for osteogenesis coupled angiogenesis in bone tissue engineering. *Mater Sci Eng C 103*, 109761.

Parent M, Baradari H, Champion E, Damia C, Viana-Trecant M (2017) Design of calcium phosphate ceramics for drug delivery applications in bone diseases: A review of the parameters affecting the loading and release of the therapeutic substance. *J Control Release 252*, 1-17.

Rawat K, Agarwal S, Tyagi A, Verma A, Bohidar HB (2014) Aspect ratio dependent cytotoxicity and antimicrobial properties of nanoclay. *Appl Biochem Biotech 174*(3), 936-944.

Repetto G, Del Peso A, Zurita JL (2008) Neutral red uptake assay for the estimation of cell viability/cytotoxicity. *Nat Prot 3*(7), 1125-1131.

Richetta M, Varone A, Mattoccia A, Medaglia PG, Kaciulis S, Mezzi A, Pizzoferrato R (2018) Preparation, intercalation, and characterization of nanostructured (Zn, Al) layered double hydroxides (LDHs). *Surf Interface Anal 50*(11), 1094-1098.

Riss TL, Moravec RA, Niles AL, Duellman S, Benink HA, Worzella TJ, Minor L (2016) Cell viability assays. *Assay Guidance Manual [Online]*

Rives V, del Arco M and Martín C (2014) Intercalation of drugs in layered double hydroxides and their controlled release: A review. *Appl Clay Sci*, *88*, 239-269.

Rojas R, Mosconi G, Zanin JP, Gil GA (2022) Layered double hydroxide applications in biomedical implants. *Appl Clay Sci 224*, 106514.

Ruzicka B and Zaccarelli E (2011) A fresh look at the Laponite phase diagram. *Soft Matter*, *7*(4), 1268-1286.

Saikia P (2020) Clay nanostructures for biomedical applications. In *Two-Dimensional Nanostructures for Biomedical Technology* (pp. 137-172). Elsevier.

Seftel EM, Popovici E, Mertens M, De Witte K, Van Tendeloo G, Cool P, Vansant, EF (2008) Zn–Al layered double hydroxides: Synthesis, characterization and photocatalytic application. *Micropor Mesopor Mater 113*(1-3), 296-304.

Shan D, Cosnier S, Mousty C (2003) Layered double hydroxides: an attractive material for electrochemical biosensor design. *Anal Chem 75*(15), 3872-3879.

Shirin VA, Sankar R, Johnson AP, Gangadharappa HV, Pramod K (2021) Advanced drug delivery applications of layered double hydroxide. *J Control Release*, *330*, 398-426.

Srivastava P, Singh B, Angove M (2005) Competitive adsorption behavior of heavy metals on kaolinite. *J Colloid Interface Sci*, *290*(1), 28-38.

Sukhanova A, Bozrova S, Sokolov P, Berestovoy M, Karaulov A, & Nabiev I. (2018) Dependence of nanoparticle toxicity on their physical and chemical properties. *Nanoscale Res Lett 13*(1), 1-21.

Sun ZL, Wataha JC, Hanks CT (1997). Effects of metal ions on osteoblast-like cell metabolism and differentiation. *J Biomed Mater Res 34*(1), 29-37.

Syama S, Paul W, Sabareeswaran A, Mohanan PV (2017). Raman spectroscopy for the detection of organ distribution and clearance of PEGylated reduced graphene oxide and biological consequences. *Biomaterials*, *131*, 121-130.

Tang G, Liu Z, Liu Y, Yu J, Wang X, Tan Z, Ye X (2021). Recent trends in the development of bone regenerative biomaterials. *Front Cell Development Bio 9*.

Tathod, Anup P, Oz M Gazit (2016) Fundamental insights into the nucleation and growth of Mg–Al layered double hydroxides nanoparticles at low temperature." *Crystal Growth Design* 16, no. 12, 6709-6713.

Tichit D, Layrac G, Gérardin, C (2019) Synthesis of layered double hydroxides through continuous flow processes: A review. *Chem Eng J 369*, 302-332.

Tonelli D, Gualandi I, Musella E, Scavetta E (2021) Synthesis and characterization of Layered Double Hydroxides as materials for electrocatalytic applications. *Nanomaterials 11*(3), 725.

Unfried K, Albrecht C, Klotz LO, Von Mikecz A, Grether-Beck S, Schins RP (2007).Cellular responses to nanoparticles: target structures and mechanisms. *Nanotoxicol 1*(1), 52-71.

Van Olphen H and J. J. Fripiat (1979) Data handbook for clay materials and other nonmetallic minerals, Pergamon Press.

Varga G (2007) The structure of kaolinite and metakaolinite. *Epitoanyag*, *59*(1): 6-9.

Wan Y, Fan Y, Dan J, Hong C, Yang S, Yu F (2019) A review of recent advances in two-dimensional natural clay vermiculite-based nanomaterials. *Mater Reser Express*, *6*(10), 102002.

Wang Q and O'Hare D (2012) Recent advances in the synthesis and application of layered double hydroxide (LDH) nanosheets. *Chem Rev 112*(7), 4124-4155.

Wang Y, Wang M (2022). Low-dimensional physics of clay particle size distribution and layer ordering. *Sci Rep 12*(1), 1-11.

Wang Y, Mei X, Bian Y, Hu T, Weng X, Liang R, Wei M (2020) Magnesium-based layered double hydroxide nanosheets: a new bone repair material with unprecedented osteogenic differentiation performance. *Nanoscale*, *12*(37), 19075-19082.

Wei X, Shao B, He Z, Ye T, Luo M, Sang Y, Zhang Z (2015) Cationic nanocarriers induce cell necrosis through impairment of Na+/K+-ATPase and cause subsequent inflammatory response. *Cell Res*, *25*(2), 237-253.

Wei Y, Quan L, Zhou C, Zhan Q (2018) Factors relating to the biodistribution & clearance of nanoparticles & their effects on *in-vivo* application. *Nanomedicine*, *13*(12), 1495-1512.

Wong F, Buchheit RG (2004) Utilizing the structural memory effect of layered double hydroxides for sensing water uptake in organic coatings. *Prog Org Coatings 51*(2), 91-102.

Wu D, Ma Y, Cao Y, Zhang, T (2020) Mitochondrial toxicity of nanomaterials. *Sci Total Environ 702*, 134994.

Wu M, Chen F, Wu P, Yang Z, Zhang S, Xiao L, Cai L (2021) Nanoclay mineral-reinforced macroporous nanocomposite scaffolds for in situ bone regeneration: In vitro and *in-vivo* studies. *Mater Design*, *205*, 109734.

Wu Y, Zhu R, Zhou Y, Zhang J, Wang W, Sun X, Wang S (2015) Layered double hydroxide nanoparticles promote self-renewal of mouse embryonic stem cells through the PI3K signaling pathway. *Nanoscale*, *7*(25), 11102-11114.

Xie W, Guo Z, Gao Q, Wang D, Liang K, Gu Z, Zhao LY (2020) Manganese-doped layered double hydroxide: a biodegradable theranostic nanoplatform with tumor microenvironment response for magnetic resonance imaging-guided photothermal therapy. *ACS Appl Bio Mater*, *3*(9), 5845-5855.

Yan L, Gonca S, Zhu G, Zhang W, Chen X (2019) Layered double hydroxide nanostructures and nanocomposites for biomedical applications. *J Mater Chem B*, *7*(37), 5583-5601.

Yan M, Yang C, Huang B, Huang Z, Huang L, Zhang X, Zhao C (2017). Systemic toxicity induced by aggregated layered double hydroxide nanoparticles. *Int J Nanomedicine*, *12*, 7183.

Yu J, Chung HE, Choi SJ (2013) Acute oral toxicity and kinetic behaviors of inorganic layered nanoparticles. *J Nanomaterials*, *2013*.

Yuan P, Tan D, Annabi-Bergaya F(2015) Properties and applications of halloysite nanotubes: recent research advances and future prospects. *Appl. Clay Sci.* 112–113, 75–93.

Zhang, H., Fan, T., Chen, W., Li, Y. and Wang, B., 2020. Recent advances of two-dimensional materials in smart drug delivery nano-systems. *Bioactive Materials*, *5*(4), 1071-1086.

Zhang J, Zhang F, Ren L, Evans DG, Duan X (2004) Synthesis of layered double hydroxide anionic clays intercalated by carboxylate anions. *Mater Chem Phys 85*(1), 207-214.

Zhang L, Yang G, Johnson BN, Jia X (2019) Three-dimensional (3D) printed scaffold and material selection for bone repair. *Acta biomaterialia*, *84*, 16-33.

Zhang S, Chen J, Yang WS, Chen X (2022) Vacancies-rich CoAl monolayer layered double hydroxide as efficient superoxide dismutase-like nanozyme. *Nano Res* 1-11.

Zhang Y, Long M, Huang P, Yang H, Chang S, Hu Y, Tang A, Mao L (2017) Intercalated 2D nanoclay for emerging drug delivery in cancer therapy. *Nano Res 10*(8), pp.2633-2643.

Zhao J, Wu H, Zhao J, Yin Y, Zhang Z, Wang S, Lin K (2021) 2D LDH-MoS2 clay nanosheets: synthesis, catalase-mimic capacity, and imaging-guided tumor photo-therapy. *J Nanobiotech*, *19*(1), 1-16

Zhao R, Yang R, Cooper PR, Khurshid Z, Shavandi A, Ratnayake J (2021) Bone grafts and substitutes in dentistry: A review of current trends and developments. *Molecules 26*(10), 3007.

Zhao Y, Li F, Zhang R, Evans DG, Duan X (2002) Preparation of layered double-hydroxide nanomaterials with a uniform crystallite size using a new method involving separate nucleation and aging steps. *Chem Mater 14*(10), 4286-4291.

Zheng L, Zhou B, Qiu X, Xu X, Li G, Lee WY, Li, Y (2019) Direct assembly of anticancer drugs to form Laponite-based nanocomplexes for therapeutic co-delivery. *Mater Sci Eng C 99*, 1407-1414.

Zheng Y, Hong X, Wang J, Feng L, Fan T, Guo R, Zhang H (2021) 2D nanomaterials for tissue engineering and regenerative nanomedicines: recent advances and future challenges. *Advanced healthcare materials*, *10*(7), 2001743.

Zhou X, Zhao L, Luo J, Tang H, Xu M, Wang Y, Jing B (2019) The toxic effects and mechanisms of Nano-Cu on the spleen of rats. *Int J Mol Sci 20*(6), 1469.

Zhu R, Wang Q, Zhu Y, Wang Z, Zhang H, Wu B, Wang S (2016). pH sensitive nano layered double hydroxides reduce the hematotoxicity and enhance the anticancer efficacy of etoposide on non-small cell lung cancer. *Acta biomater*, *29*, 320-332.

Zubair M, Daud M, McKay G, Shehzad F, Al-Harthi MA. (2017) Recent progress in layered double hydroxides (LDH)-containing hybrids as adsorbents for water remediation. *Appl Clay Sci 143*, 279-292.

Zümreoglu-Karan B, Ay A (2012) Layered double hydroxides—multifunctional nanomaterials. *Chem Papers 66*(1), 1-10.

ANNEXURES

LIST OF PUBLICATIONS

Journals

1. **Ashtami J**, Mohanan PV (2023) Co-precipitation-hydrothermal mediated synthesis, characterization and toxicity evaluation of 2D Zn–Al LDHs in human osteoblast cells, *J Mater Sci,* 1-13. (I.F-4.68)

2. Biby TE, Prajitha N, **Ashtami J**, Sakthikumar D, Maekawa T, Mohanan, P.V (2020) Toxicity of dextran stabilized fullerene C60 against C6 Glial cells. Brain Research Bulletin. *155*, 191-201 (I.F 3.715).

3. Cherian RS, **Ashtami J,** Mohanan PV (2020) Effect of surface modified reduced graphene oxide nanoparticles on cerebellar granule neurons. Journal of Drug Delivery Science and Technology, p.101706, (I.F 3.981).

4. **Ashtami J**, Anju S, Mohanan PV (2019) Conformity of dextran-coated fullerene C70 with L929 fibroblast cells. Colloids and Surfaces B: Biointerfaces, *184*, p.110530, (I.F 5.8).

5. Cherian R.S, Sandeman S, Ray S, Savina I.N, **Ashtami J,** Mohanan P.V (2019) Green synthesis, characterization and cytoskeletal integrity of Pluronic stabilized reduced graphene oxide nanoparticles. Colloids Surf B Biointerfaces, 179, 94-106, (I.F 5.8).

6. Anju S, **Ashtami J,** Mohanan PV (2019) Effect of Surface Modified Fullerene C70 on the ROS Production and Cellular Integrity Using Chinese Hamster Ovarian Cells. General Chemistry, 5, 190022.

Review

7. **Ashtami J**, Anju S, Mohanan PV (2018) 2D materials for next generation healthcare applications. International journal of pharmaceutics, *551*(1-2), 309-321, (I.F-6.81)

8. Anju S, **Ashtami J**, Mohanan PV(2019) Black phosphorus, A prospective graphene substitute for biomedical applications, Material Science & Engineering C, Elsevier, 9, 978-993, (IF 8.451).

9. Athira SS, **Ashtami J**, Mohanan PV (2020) Glial cell colony injured on exposure to fullerene soot nanoparticles. Letters in applied nanobioscience,9 (4), 1637-1643, (I.F 1.9).

10. Ashtami J, Mohanan PV (2020) Do graphene worship cerebellar granular neuron cells, Pharm Anal Act, Vol 12,Issue 2. (I.F 1.43)

11. **Ashtami J**, Athira SS, Mohanan PV (2020) Fullerene C70- a promising cage for biomedical applications. Trends in Biomaterials and artificial organs, (I.F : .011).

12. Athira SS, **Ashtami J**, Mohanan PV (2020) Nanofullerene mixture impose threat to alveolar epithelial cells. EC Pharmacology and toxicology,8.9:38-43 (I.F 1.02).

13. Sruthi S, **Ashtami J**, Mohanan PV (2018) Biomedical application and hidden toxicity of Zinc oxide nanoparticles. Materials today chemistry, *10*, 175-186, (I.F 7.3).

Book chapters

14. **Ashtami J**, Joseph X, Akhil V.G, Athira S.S, Mohanan P.V (2020) 2D layered double hydroxides, *Layered Advanced Materials and their Allied Applications,* Wiley-Scrivener Publisher

15. Athira SS, Joseph X, Akhil VG, **Ashtami J,** Mohanan PV (2020) 2D hollow nanomaterials, *Layered Advanced Materials and their Allied Applications,* Wiley-Scrivener Publisher, pp.211-248.

16. **Ashtami J,** Athira, SS, Reshma VG, Mohanan, PV (2019) Black Phosphorous Based Nanodevices, In *Black Phosphorus* (pp. 31-58). Springer, Cham.

Online publications

17. **Ashtami J,** Mohanan PV (2019) Chemical and biological characterization spot the faith of nanoparticles. Science Trends (in Energy and Matter Column), June 19, 2019.

18. Anju S, **Ashtami J**, Mohanan PV. (2019) Black phosphorous : a miracle material for future biomedical technology. Science Trends, April 11, 2019.

19. **Ashtami J,** Syama S, Mohanan, P.V, (2018) Magical chemistry of graphene in stem cells differentiation for osteogenesis, December 6, 2018.

20. **Ashtami J**, Anju, S, Mohanan P.V, (2018) Significance of 2D materials in the biomedical sphere. Science Trends, November 28, 2018

AWARDS & FELLOWSHIPS

- Fulbright-Nehru Doctoral Visiting Students Fellowship (2020-2021) organized by United States-India Educational Foundation, Fulbright Commission in India at University of Houston, Texas, US.
- SCTIMST Institute fellowship

CONFERENCES ATTENDED

- **Ashtami J** and Mohanan PV*. Assessment of cytotoxicity of Zn-Al Layered double hydroxide using L929 cell. Poster presentation, 40th Annual Conference of Society of Toxicology (STOX), India, STOX-2021, 29-30 Jan 2021.

- **Ashtami J,** Mohanan PV. Layered double hydroxide: a new generation 2D material for bone tissue engineering. Presented at International Conference on Emerging Advancement in Science and Technology (ICEAST 2019)**,** 5-6 September 2019.

- **Ashtami J**, Anju, S, Mohanan P.V (2018) Fullerene C70: a promising nanoparticle for biomedical applications. Presented at the 'International Conference on the Role of Toxicology in Public Health & 38th Annual Conference of Society of Toxicology, India, Sri Balaji Vidyapeeth, Puducherry, India, 12-14 December 2018.

- Anju, S, **Ashtami J**, Mohanan P.V (2018) Cytocompatibility of C70 fullerene nanocomposite using CHO cells. Presented at the 'International Conference on the Role of Toxicology in Public Health & 38th Annual Conference of Society of Toxicology, India, Sri Balaji Vidyapeeth, Puducherry, India, 12-14 December 2018.

- **Ashtami J**, Anju S, Mohanan PV (2018) Interaction of surface functionalized fullerene C70 with L929 cells. Presented at 28th Swadeshi Science Congress, National Institute for Interdisciplinary Sciences and Technology, Thiruvananthapuram, Kerala, India, 7-9 November 2018.

- Anju S, **Ashtami J**, Mohanan PV (2018) Characterization and cyto-compatibility of surface modified C70 fullerene nanoparticles using CHO cells lines. Presented at 28th Swadeshi Science Congress, National Institute for Interdisciplinary Sciences and Technology, Thiruvananthapuram, Kerala, India, 7-9 November 2018.

WEBINARS & WORKSHOPS ATTENDED

- International webinar on food, chemical and nanomaterial toxicity by SCTIMST-Central University of Kerala in association with Kerala Academy of Sciences on 26-28 Nov 2020 at biomedical technology wing SCTIMST.

- Tissue engineering for biomedical applications organized by Industry Institute Partnership Cell (IIPC) on 28- 29 June 2019 at BMT wing, SCTIMST, Trivandrum.

- Hands-on workshop on flow cytometry organized by Sree Chitra Tirunal Institute for Medical Sciences and Technology on 5-7 December 2019 at BMT wing, SCTIMST, Trivandrum.